OPTICAL APPROACHES TO STUDY NANOSCALE ELECTROCHEMICAL PROCESSES

A Dissertation

Submitted to

The Temple University Graduate Board

In Partial Fulfillment

of the Requirements for the Degree

DOCTOR OF PHILOSOPHY

---

by

Joseph W. Monaghan

May 2023

Examining Committee Members:

Katherine A. Willets, Ph.D., Advisor, Chemistry, Temple University
Daniel Strongin, Ph.D., Chemistry, Temple University
Yugang Sun, Ph.D., Chemistry, Temple University
Chetan Patil, Ph.D., External Member, Engineering, Temple University

ABSTRACT

In this work, we use optical approaches to study and provide mechanistic insight into electrochemical reactions occurring at the surface of single nanoparticles. Correlated optical-electrochemical studies offer several advantages over single nanoparticle electrochemical studies including, higher spatial resolution, the ability to interrogate many nanoparticles at the same time and identify populations of inactive nanoparticles. Throughout this dissertation, two optical techniques are discussed in detail, dark-field scattering and super-localization imaging. In the first set of experiments, we describe calcite-assisted localization and kinetics (CLocK) microscopy, a multiparameter super-localization imaging technique. By placing a rotating birefringent calcite crystal in the infinity space of an optical microscope, CLocK provides immediate polarization and orientation information while still maintaining the ability to localize a single nanoparticle with < 10 nm resolution. Additionally, we demonstrate that the CLocK point spread function encodes kinetic information that we quantified to be an order of magnitude shorter than the integration time of the camera. In this work, CLocK provides new mechanistic insight into dynamic processes such as the dissolution of single gold nanorods as well as single-molecule surface-enhanced Raman scattering. In the second work, dark-field scattering was employed to monitor a proposed post-synthesis silver nanoparticle surface cleaning strategy to improve homogeneity across a population. Here, a sacrificial silver-sulfide sulfide shell is chemically grown on single silver nanoparticles to outcompete surface impurities. We demonstrate that upon electrochemical removal of the shell, a more reactive and reproducible silver surface can be achieved as revealed by enhanced

electrodissoluion of the freshly cleaned silver nanoparticles. In these experiments, we additionally found a sulfide-dependent formation of multiple sulfide-species as well as mixed character sulfide shells on single nanoparticles themselves, thus demonstrating the sensitivity provided by optical microscopy at identifying multiple surface chemistries. Overall, the work in this dissertation highlights the ability of optical tools at revealing heterogeneity in single particle studies providing insight into structure-function relationships.

DEDICATION

I would not have made it to the finish line of this Ph.D. without the unwavering support and love of my family. I dedicate this dissertation to each of you.

Mom and Dad: You taught me that if I believe in myself, work hard, and have faith, things will always work out in the end. This Ph.D. is a testament to that belief. Thank you both for your support of not only my academic goals but my goals in life. I wouldn't be the person I am today without you.

Alyssa and Matt: Being your older brother was the best part of growing up for me. I cherish each memory we made and look forward to each left to make. Thank you for the endless laughs and being my first two friends in life.

Frances and Mike: You both accepted me into your home and family with open arms and never expected anything in return. You helped me through difficult life choices, teaching me things are better solved together than alone. Thank you both for seeing me as your second son.

Yeidi, Pepe, Boey and Mookie: Collectively you all keep me young and make me feel old at the same time, I don't know how that's possible, but it is. Thank you for teaching me patience and always showing me love (in your own ways) after a long day.

Nati: My best friend. My love. My biggest supporter. You encouraged me to follow my heart and not be afraid of trying something new. Graduate school would not have been possible without you by my side each step of the way. While stressful, I wouldn't have traded our late-night dissertation-writing sessions for anything because we were in it together. Thank you for allowing me to be me and loving that person. Thank you for being you and allowing me to love that person. Forever and always.

ACKOWLEDGEMENTS

I would first like to acknowledge my research advisor, Professor Katherine A. Willets. Your mentorship, support, and frequent advice had immeasurable impact in both my development as a scientist but also my growth as a person.

I would like to thank my dissertation committee members Professor Daniel Strongin, Professor Yugang Sun, and Professor Chetan Patil for their scientific discussions and feedback over my research career.

A special acknowledgement goes out to my current and former colleagues for the constant support of my research progress and making our office an inviting and overall fun place to work. Professor Vignesh Sundaresan, Zachary O'Dell, Sanjay Sridhar, and Phillip Reinhardt were invaluable during my Ph.D. career providing collaboration and input on multiple projects.

I had the fortunate opportunity to collaborate with other research groups on several occasions: Professor Henry White's group – University of Utah, Professor Xingchen Ye's group – Indiana University, and Professor Alexander Gray's group – Physics Department at Temple University.

Finally, I would like to acknowledge the National Science Foundation, Air Force Office of Scientific Research, and Temple University for the financial support that made my research possible.

TABLE OF CONTENTS

LIST OF FIGURES

Figure 3.10. Comparison of spectral features found in CLocK images of a Au NS, large-width Au NR (NR-1, 126 x 61 nm), and small-width Au NR (NR-2, 113 x 51 nm). (A) From top to bottom: dark-field color CLocK images, SEM images, wavelength-averaged dark field (DF) CLocK images and spectrally-dependent dark field CLocK using bandpass filters centered at the wavelengths indicated. Images are shown at an optimal contrast to highlight the $e_{\perp}$ pattern. Scale bars: Color = 2 □m; SEM = 50 nm; DF = 1 μm. Optical images were acquired with an integration time of 300 ms. Bandpass filters: 562 ± 20 nm, 655 ± 20 nm, and 692 ± 20 nm. (B-D) Polar plots showing how the angle-dependent $e_{\perp}$ intensity changes as a function of bandpass filter wavelength. The data are normalized to the maximum scattering intensity and fit to Equation 3.2. Each trace in the polar plot is color coordinated to the bandpass filter labels in A. Each circle-tick of the polar plots is 0.25 normalized intensity units. (E-G) Normalized scattering intensity spectra of the intensity of $o_{\parallel}$ (black), $e_{\perp\,long}$ (red), and $e_{\perp\,trans}$ (blue) as a function of bandpass filter center wavelength. Data points are shown at the center wavelength of each filter and lines are drawn to guide the eye. Results from (B-D) and (E-G) agree well with polarization-resolved single-NP dark-field spectroscopy data (Figure 3.13).

Figure 3.11. (A) Dark-field CLocK images from Figure 3.10 with complete range of bandpass filters. Scale bars: SEM = 50 nm; Color = 2 □m; DF = 1 □m. (B) Normalized intensity polar plots showing how the intensity and modulation depth of the $e_{\perp}$ changes as a function of bandpass filter wavelength. Polar plots are color coordinated to bandpass filter labels and CLocK images in A.

Figure 3.12. Modulation depth and orientation obtained from CLocK images plotted as a function of bandpass filter wavelength for the Au NS, Au NR-1, and Au NR-2 discussed in Figures 3.10 & 3.11.

Figure 3.13. Comparison of spectral data obtained using CLocK images (data points) and single-particle polarization-resolved dark-field scattering spectroscopy for the Au NS, Au NR-1, and Au NR-2 discussed in Figures 3.10, 3.11, 3.12. (A) CLocK $o_{\parallel}$ intensity as a function of bandpass filter wavelength compared with the single-particle unpolarized dark-field scattering spectra of each Au NP. (B) CLocK $e_{\perp\,trans}$ intensity as a function of bandpass filter wavelength compared to single-particle polarized-resolved dark-field scattering spectra corresponding to $\theta = \varphi + 90°$ for each Au NP. (C) Comparison of CLocK $e_{\perp\,long}$ intensity as a function of bandpass filter wavelength to the single-particle polarized dark-field scattering spectra corresponding to $\theta = \varphi$ of each Au NP. (D) Intensity polar plots obtained from single-particle polarization-resolved dark-field scattering spectroscopy. Plots are color coordinated to the bandpass filter labels, CLocK images, and polar plot in Figure 3.11.

LIST OF TABLES

CHAPTER 1: INTRODUCTION

1.1 Single Nanoparticle Electrochemistry

Metal nanoparticles (NPs) have become a widely adopted electrode material for energy storage and conversion,[1,2] biosensing,[2,3] (photo)catalysis,[4–6] and corrosion[7–9] applications due to the attractive properties achieved after reducing the size of the metal to the nanoscale. Traditionally, performance of these nano-electrodes is benchmarked using bulk electrochemical techniques, such as potentiometry and amperometry, where the current response measured represents an ensemble average of large numbers of NPs assembled on a supporting electrode.[10–13] However, at the nanoscale, size, shape, and surface properties lead to heterogeneous performance from particle-to-particle, a phenomenon hidden in ensemble electrochemical techniques.[10,14–16] To address this issue, single NP electrochemical studies are necessary to better understand and assign structure-function relationships for the development of more efficient systems.

Over the past decade, the field of nano-electrochemistry has seen a surge of interest with a common goal of improving sensitivity in electrochemical measurements at a single entity level.[17–20] Specifically for single NP experiments, improvement to fabrication methods has allowed researchers to make electrodes on the order of a few tens-of-nanometers in diameter which are capable of probing electrochemical signals from redox reactions involving single NPs with sufficiently high signal-to-noise.[21,22] These electrodes are often referred to as ultramicroelectrodes (UMEs) and are the backbone of techniques such as scanning electrochemical microscopy (SECM),[11,21,23] and single NP collision-based studies.[24–26] Collision-based studies are of particular interest for single NP

electrochemistry measurements due to their low cost, experimental simplicity, and high-level sensitivity.[24,27] In these types of studies, an inert UME is immersed in a solution containing electrocatalytic NPs and biased at a potential such that a redox mediator in solution or the NPs themselves undergo redox reaction. For example, Zhang and co-workers reported the observation of electrocatalytic water oxidation as silver NPs (Ag NPs) collide with a gold UME that was held at oxidizing potentials (Figure 1.1A).[28] The authors observed that at sufficiently high oxidizing potentials, most Ag NP collision events consisted of a sharp subcollsion peak followed by a long decay time (τ) (Figure 1.1B). They discovered that the total charge transferred in these events was higher than that estimated from complete oxidation of the Ag NPs. This suggested additional redox chemistry was occurring at the surface beyond the oxidation of the Ag NPs. Control studies in which they varied the pH of the NP solution, the oxidizing potential at which the UME was held, and the size of the Ag NPs revealed that particle-dependent silver oxide (Ag_2O) growth on the surface of the Ag NPs occurred during collision and served as the catalyst for water oxidation. The single particle nature of their collision experiments provided mechanistic insight into the oxidation of Ag NPs that would otherwise be unobservable in similar bulk electrochemical measurements.

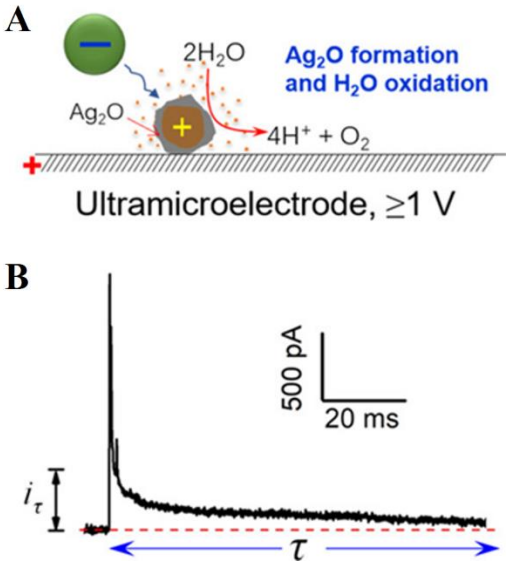

Figure 1.1. (A) As Ag NPs stochastically collide with the Au UME held at an oxidizing potential, the NP oxidizes to Ag^+ ions (red circles) and forms an outer silver oxide (Ag_2O) layer (shown in gray) which catalyzes water oxidation. (B) A single current spike is observed as a single Ag NP collides, oxidizes, and catalyzes water oxidation on the Au UME. Adapted from Reference 28. Copyright 2018, American Chemical Society.

While single NP electrochemical techniques like collision-based studies are effective for demonstrating NP heterogeneity by monitoring changes in electroactivity, they are still limited to studying one NP at a time, thus creating time consuming experiments with an inability of providing spatial or compositional feedback of the NPs. Complimenting single NP electrochemistry with other *in situ* techniques such as optical microscopy can lead to a more complete understanding of structure-function relationships for single NP studies.[29–31]

1.2 Optical Techniques for Single Nanoparticle Studies

Despite single NP electrochemical techniques providing insight into NP heterogeneity through reaction kinetics at the single NP level, correlated electrochemical and optical methods can offer spatial and structural information that is essential for mechanistic insight into single NP behavior.[32,33] Throughout this dissertation, two optical

techniques are discussed in detail, dark-field optical microscopy and super-localization imaging.

Dark-field optical microscopy

Metal NPs like silver and gold support localized surface plasmon resonances (i.e. the collective oscillation of surface conduction electrons) when exposed to light, resulting in efficient light scattering at wavelengths in the visible region of the spectrum.[34–36] This makes nanomaterials such as silver and gold well suited for optical studies where the light scattered from individual NPs can be made observable with the assistance of an optical microscope. In a dark-field configuration (Figure 1.2A),[37] white light is passed through a high numerical aperture (N.A.) dark-field condenser which blocks low angle light from the source allowing a hollow cone of high angle light to illuminate the sample of interest. Light that is scattered by the NPs is collected by a low N.A. objective and imaged onto a detector, such as a charged coupled device (CCD), while light that passes through the sample without interacting with any NPs is rejected by internal optics of the objective. The resulting dark-field optical image shows diffraction limited bright spots which represent NPs against a dark background. Figure 1.2B shows an example of a dark-field scattering image of gold nanospheres (Au NSs) collected on a colored CCD camera.[37] Here, different diffraction-limited spots with varying colors are observed due to heterogeneity in size/shape of the Au NSs. By placing a spectrometer in the imaging path, the wavelength of light scattered from each NS can be quantified as a spectral image thus providing relative feedback on size and shape (Figure 1.2C).[37] Previous work from our lab has demonstrated that dark-field optical imaging can be used in unison with electrochemical techniques to monitor reactions on individual particles in real time.[14–16] In this dissertation, dark-field optical imaging is used

to demonstrate a methodology of restoring the surface of silver nanoparticles to a more homogeneous and reactive state by electrochemically removing a chemically-grown silver-sulfide shell (Chapter 4).

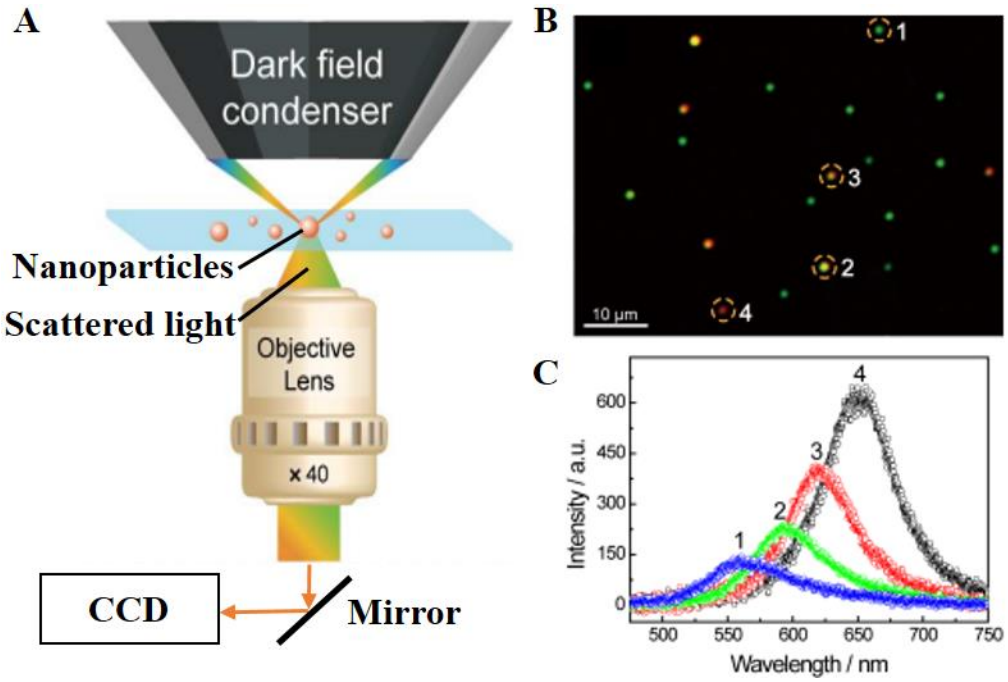

Figure 1.2. (A) Generalized scheme of a dark-field optical microscope in an inverted configuration. (B) Dark-field scattering image of ~ 50 nm gold nanospheres captured by a colored CCD camera where different sized/shaped nanospheres appear as diffraction limited spots of different colors ranging from green to red against a dark background. (C) Dark-field single particle spectra of the 4 gold nanospheres circled in (B). Adapted from Reference 37. Copyright 2011, John Wiley and Sons.

Super-localization imaging

The ability of an optical imaging system to resolve light scattered by an object is restricted by the diffraction limit of light, which limits the spatial resolution to roughly half of the wavelength of light used.[36,38] For example, the Au NSs shown in Figure 1.2B have a physical size of ~ 50 nm in diameter; however, their diffraction limited spot size in the dark-field image is ~ 300 nm in diameter.[37] The advent of super-localization based super-resolution imaging made it possible to overcome the diffraction limit of an optical imaging

system by fitting the point of highest scattering intensity from the point spread function of the diffraction limited spot to a model equation, such as a two-dimensional (2-D) Gaussian, such that the spatial location of an individual scatterer can be determined with precision better than 10 nm.[39–42] Figure 1.3 shows a visual representation of how super-localization imaging is used to approximate the center position of an individual NP from a diffraction-limited dark-field scattering image by using a 2-D Gaussian equation (Equation 1.1) to determine the position of highest scattering intensity.[14]

$$I(x,y) = z_0 + I_0 e^{-\frac{1}{2}\left[\left(\frac{x-x_0}{\sigma_x}\right)^2 + \left(\frac{y-y_0}{\sigma_y}\right)^2\right]} \qquad \text{(Eq. 1.1)}$$

Here *I(x,y)* is the intensity of the diffraction-limited spot projected onto the x and y pixels in the optical image , z_0 is the background intensity, σ_x and σ_y are the standard deviation (or width) of the diffraction-limited spot, and x_0 and y_0 are the approximated center position of the scattering object. The ability to monitor the center position of an individual NP becomes useful for single particle electrochemical studies when a redox reaction involving the NP is accompanied by a physical change in its center-of-mass, such as the asymmetric electrodissolution of Ag or Au NPs.[14–16]

While super-localization imaging is powerful in terms of providing spatial and intensity information for an individual NP, determining the NP's orientation and inferring structural information often requires additional characterization techniques such as scanning electron microscopy (SEM) or atomic force microscopy (AFM). In this dissertation, we discuss a new localization-based super-resolution imaging technique, calcite-assisted localization and kinetics (CLocK) microscopy, in which spatial, intensity, structural, and orientation information for an individual NP can be extracted from a single optical image (Chapter 3).

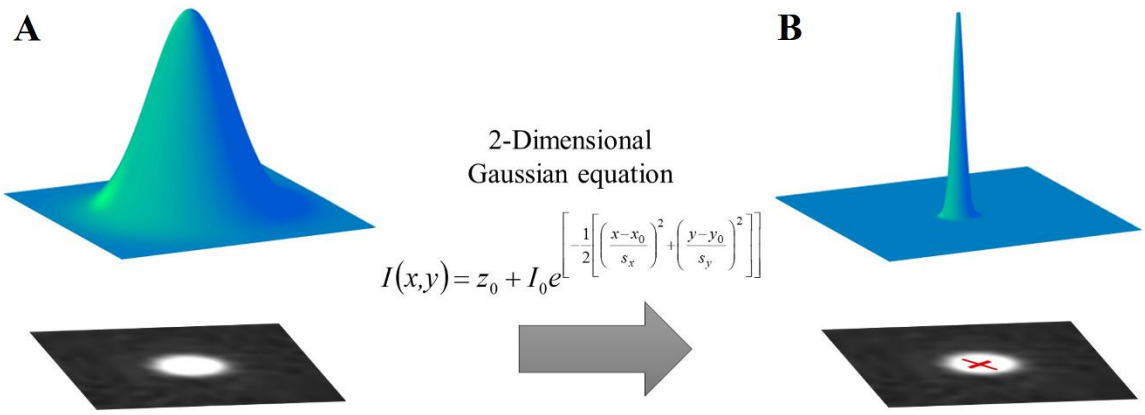

Figure 1.3. Visual representation of super-localization imaging. (A) A diffraction-limited dark-field scattering image of an individual Ag NP (bottom) with a corresponding 3-D representation (top). In the 3-D image, x- and y-dimensions represent the pixel coordinates of the diffraction limited dark-field scattering image while the z-dimension represents the intensity profile of the image. (B) Analyzing the dark-field image from (A) with a 2-D Gaussian equation allows us to determine the center position (marked with red-X) of the Ag NP by determining the point in the dark-field image of highest scattering intensity. Adapted from Reference 14. Copyright 2018, American Chemical Society.

1.3 Exploring the Role of Surface Chemistry on Silver Nanoparticle Heterogeneity

As metal particles are shrunk to the nanoscale, the chemical nature of the particle surface becomes a source of heterogeneity in their reactivity, creating a challenge in deriving structure-function relationships.[43–47] Surface oxides, capping agents, and surface ligands are all well documented sources of heterogeneity when examining surface effects on NP performance. For example, Long and co-workers compared the electrodissolution behavior of Ag NPs adsorbed to the surface of a Au UME in a pH neutral electrolyte solution versus in an alkaline (pH 11) electrolyte solution where surface oxide formation is favored.[48] The authors found that the time to reach complete oxidation (which they refer to as NP dwell time on the UME surface) for Ag NPs in the alkaline solution was up to 20 times longer than Ag NPs in the neutral solution. They attributed the slow electrodissolution kinetics to the insoluble oxide layer that formed on the surface of the Ag

NPs and additionally found that larger NPs drastically increased the time for oxidation in alkaline solution.

Previous work from our lab explored the role of surface oxides on the electrodissoluion of Ag NPs using a correlated optical-electrochemical approach (Figure 1.4A).[14] Ag NPs scatter light at their plasmon resonance which lies in the visible region of the spectrum making them easy to optically observe in a dark-field microscope setup. By monitoring the dark-field scattering intensity of single Ag NPs while an oxidation potential was applied, we observed the heterogeneous loss of scattering intensity as Ag electrodissolves to Ag^+ (Figure 1.4B). We found that the timescales of this dissolution process showed significant particle-to-particle variation that could be manipulated by the applied oxidation potential (Figure 1.4C).

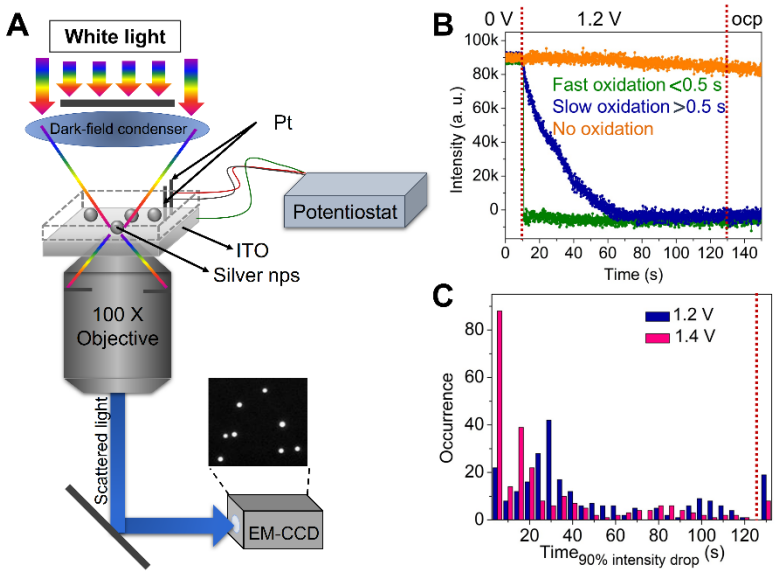

Figure 1.4. (A) Dark-field microscope setup. (B) Scattering intensity vs time for three Ag NPs with different electrodissoluion behaviors: fast (<0.5 s, green), slow (>0.5 s, blue), and no oxidation (orange). The applied potentials are indicated at the top of the graph. (C) Histogram of the time required for the particle intensity to drop to 90% of its original value at 1.2 V (blue) and 1.4 V (pink). The red dashed lines indicate particles that do not oxidize. Adapted from Reference 14. Copyright 2018, American Chemical Society.

To probe the heterogenous electrodissolution behavior, we applied super-localization imaging to examine if the Ag NPs had any changes in their spatial position. Fitting diffraction-limited dark-field images to a 2-D Gaussian equation (Equation 1.1) allowed us to localize the center of mass of the Ag NPs as they electrodissolve, thus providing feedback on how the shape of the nanoparticle progresses. This super-localization study revealed that Ag NPs electrodissolve in either a spatially symmetric (Figure 1.5A) or asymmetric manner (Figure 1.5B) which we attributed to heterogeneity in the surface oxide coverage on single Ag NPs. We proposed that a thin or uniform oxide layer led Ag oxidizing to Ag^+ evenly across the nanoparticle resulting in symmetric dissolution. If the oxide layer was non-uniform across the nanoparticle surface, then Ag oxidized to Ag^+ preferentially which led to asymmetric dissolution.

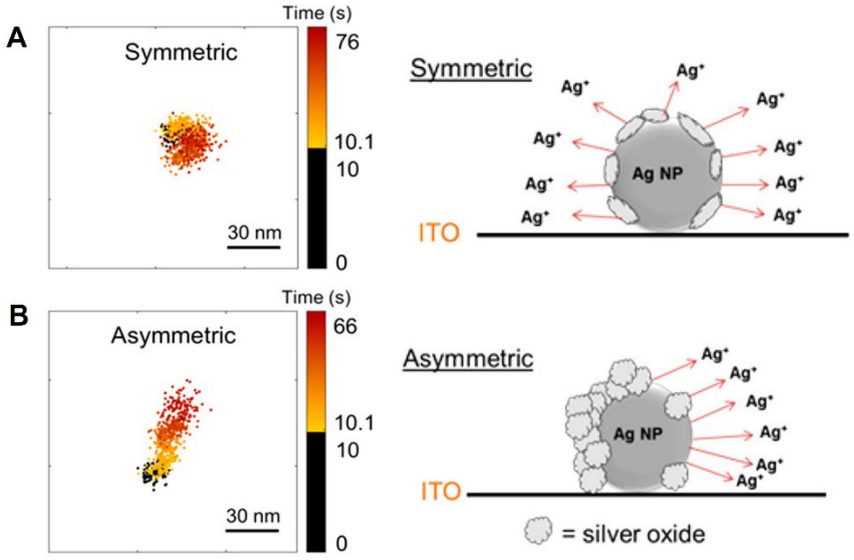

Figure 1.5. (A) Left- scatter plot showing the (x,y) center positions of a single Ag NP undergoing symmetric dissolution where the color bar indicates time evolution. Right- Schematic showing how the oxide layer on the surface of the Ag NP influences electrodissolution of a single Ag NP to undergo symmetric dissolution. (B) Left- scatter plot showing the (x,y) center positions of a single Ag NP undergoing asymmetric dissolution. Right- Schematic showing how the oxide layer on the surface of the Ag NP influences electrodissolution of a single Ag NP to undergo asymmetric dissolution. Adapted from Reference 14. Copyright 2018, American Chemical Society.

To confirm that changes in spatial origin were due to anisotropic dissolution of the nanoparticles, polarization-resolved studies were carried out in which a birefringent calcite crystal was placed in the infinity space of the microscope. As scattered light from the Ag NPs is passed through the calcite, it's split into two orthogonal polarizations producing two diffraction-limited spots in our dark-field image (Figure 1.6A). For an isotropic Ag NP, the two diffraction-limited spots will have the same intensities (Figure 1.6B), whereas anisotropic Ag NPs show different intensities (Figure 1.6C) depending on the orientation of the particle. We quantified the anisotropy by defining a ratio of the two diffraction-limited spots of the optical image as the *M* value:

$$M = \frac{I_{left} - I_{right}}{I_{left} + I_{right}} \qquad \text{(Eq. 1.2)}$$

where I_{left} and I_{right} correspond to the scattering intensities of the two diffraction-limited spots. *M* will have a value of zero if the nanoparticle is symmetric (Figure 1.6B) and a value between zero and one if asymmetric (Figure 1.6C). By tracking the change in *M* over time, we were able to demonstrate the anisotropic shape change Ag NPs undergo during electrodissoluion associated with heterogeneous surface oxide coverage.

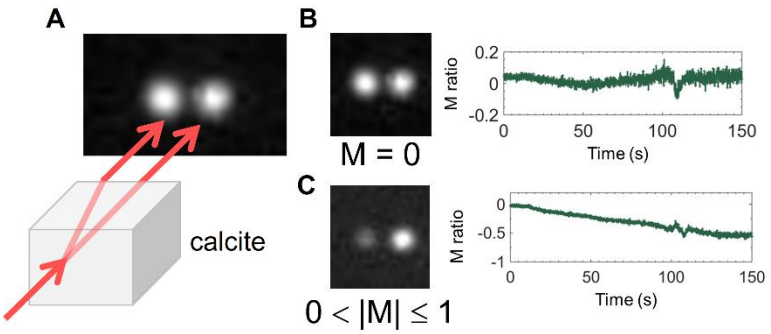

Figure 1.6. (A) Schematic of the two polarization-resolved diffraction-limited spots produced as scattered light from the Ag NPs passes through a birefringent calcite crystal. (B) Left- Example of isotropic Ag NP where intensity of two spots are the same. Right- Monitoring change in *M* during electrodissoluion where a value of zero implies the symmetric dissolution. (C) Left- Example of anisotropic Ag NP where the intensity of the two spots are different. Right- The decrease in *M* during electrodissoluion suggests that the Ag NP is undergoing asymmetric dissolution where the intensity of the spots change relative to each other over time. Adapted from Reference 14. Copyright 2018, American Chemical Society.

1.4 Scope of this Dissertation

The motivation of the research discussed in this dissertation was to address the unsolved problems of our investigation into the influence of surface oxides on the electrodissoluion of single Ag NPs. There were two challenges that we encountered in these studies, first, our ability to obtain both super-localization and single nanoparticle anisotropy information in a single optical image, and second, the heterogeneous oxide layers on Ag NPs leading to significant variation in electrodissoluion kinetics from particle-to-particle. To address the first challenge, Chapter 3 of this dissertation discusses a multiparameter super-localization imaging technique, calcite-assisted localization and kinetics (CLocK) microscopy, that builds upon the polarization-resolved imaging previously discussed. By rotating the birefringent calcite crystal, CLocK microscopy generates a polarization-averaged diffraction-limited image surrounded by a polarization-resolved ring, allowing intensity and localization information to be maintained but adding

in the ability to extract anisotropy/orientation information from a single optical image. To address the second challenge, Chapter 4 of this dissertation explores a methodology of improving the homogeneity of Ag NP electrodissolution. Here, a sacrificial silver-sulfide shell is chemically grown on the surface of single Ag NPs to compete with unwanted surface contaminants, such as surface oxides. We propose that upon electrochemical removal of this shell, a more pristine and reproducible silver surface can be achieved as revealed by fast electrodissoluion kinetics across a population of Ag NPs. This study not only demonstrates an approach for creating a more homogeneous NP surface, but also highlights the ability of optical microscopy at identifying multiple chemistries present on the surface of single NPs. Finally, in Chapter 5, we look to provide a perspective on the future of CLocK microscopy and how it could be applied to improve our understanding of Ag NP electrodissolution as well as dynamic changes to surface chemistries such as growth of silver-sulfide on single Ag NPs.

1.5 References

(1) Zhang, Q.; Uchaker, E.; Candelaria, S. L.; Cao, G. Nanomaterials for Energy Conversion and Storage. *Chem. Soc. Rev.* **2013**, *42* (7), 3127–3171.

(2) Kleijn, S. E. F.; Lai, S. C. S.; Koper, M. T. M.; Unwin, P. R. Electrochemistry of Nanoparticles. *Angew. Chem. Int. Ed.* **2014**, *53* (14), 3558–3586

(3) Lucky, S. S.; Soo, K. C.; Zhang, Y. Nanoparticles in Photodynamic Therapy. *Chem. Rev.* **2015**, *115* (4), 1990–2042.

(4) Christopher, P.; Xin, H.; Linic, S. Visible-Light-Enhanced Catalytic Oxidation Reactions on Plasmonic Silver Nanostructures. *Nat. Chem.* **2011**, *3* (6), 467–472.

(5) Hartland, G. V.; Besteiro, L. V.; Johns, P.; Govorov, A. O. What's so Hot about Electrons in Metal Nanoparticles? *ACS Energy Lett.* **2017**, *2* (7), 1641–1653.

(6) Sambur, J. B.; Chen, P. Approaches to Single-Nanoparticle Catalysis. *Annu. Rev. Phys. Chem.* **2014**, *65* (1), 395–422.

(7) Saji, V. S.; Thomas, J. Nanomaterials for Corrosion Control. *Curr. Sci.* **2007**, *92* (1), 51–55.

(8) Al-Zubeidi, A.; Stein, F.; Flatebo, C.; Rehbock, C.; Hosseini Jebeli, S. A.; Landes, C. F.; Barcikowski, S.; Link, S. Single-Particle Hyperspectral Imaging Reveals Kinetics of Silver Ion Leaching from Alloy Nanoparticles. *ACS Nano* **2021**, *15* (5), 8363–8375.

(9) Glover, R. D.; Miller, J. M.; Hutchison, J. E. Generation of Metal Nanoparticles from Silver and Copper Objects: Nanoparticle Dynamics on Surfaces and Potential Sources of Nanoparticles in the Environment. *ACS Nano* **2011**, *5* (11), 8950–8957.

(10) Ivanova, O. S.; Zamborini, F. P. Size-Dependent Electrochemical Oxidation of Silver Nanoparticles. *J. Am. Chem. Soc.* **2010**, *132* (1), 70–72.

(11) Mirkin, M. V.; Sun, T.; Yu, Y.; Zhou, M. Electrochemistry at One Nanoparticle. *Acc. Chem. Res.* **2016**, *49* (10), 2328–2335.

(12) Fang, Y.; Wang, H.; Yu, H.; Liu, X.; Wang, W.; Chen, H.-Y.; Tao, N. J. Plasmonic Imaging of Electrochemical Reactions of Single Nanoparticles. *Acc. Chem. Res.* **2016**, *49* (11), 2614–2624.

(13) Yu, Y.; Sundaresan, V.; Bandyopadhyay, S.; Zhang, Y.; Edwards, M. A.; McKelvey, K.; White, H. S.; Willets, K. A. Three-Dimensional Super-Resolution Imaging of Single Nanoparticles Delivered by Pipettes. *ACS Nano* **2017**, *11* (10), 10529–10538.

(14) Sundaresan, V.; Monaghan, J. W.; Willets, K. A. Visualizing the Effect of Partial Oxide Formation on Single Silver Nanoparticle Electrodissolution. *J. Phys. Chem. C* **2018**, *122* (5), 3138–3145.

(15) Sundaresan, V.; Monaghan, J. W.; Willets, K. A. Monitoring Simultaneous Electrochemical Reactions with Single Particle Imaging. *ChemElectroChem* **2018**, *5* (20), 3052–3058.

(16) Molina, N. Y.; Pungsrisai, T.; O'Dell, Z. J.; Paranzino, B.; Willets, K. A. The Hidden Role of the Supporting Electrode for Creating Heterogeneity in Single Entity Electrochemistry. *ChemElectroChem* **2022**, *9* (9).

(17) Murray, R. W. Nanoelectrochemistry: Metal Nanoparticles, Nanoelectrodes, and Nanopores. *Chem. Rev.* **2008**, *108* (7), 2688–2720.

(18) Peng, Y.-Y.; Qian, R.-C.; Hafez, M. E.; Long, Y.-T. Stochastic Collision Nanoelectrochemistry: A Review of Recent Developments. *ChemElectroChem* **2017**, *4* (5), 977–985.

(19) Baker, L. A. Perspective and Prospectus on Single-Entity Electrochemistry. *J. Am. Chem. Soc.* **2018**, *140* (46), 15549–15559.

(20) Robbs, P. H.; Rees, N. V. Nanoparticle Electrochemistry. *Phys. Chem. Chem. Phys.* **2016**, *18* (36), 24812–24819.

(21) Sun, T.; Yu, Y.; Zacher, B. J.; Mirkin, M. V. Scanning Electrochemical Microscopy of Individual Catalytic Nanoparticles. *Angew. Chem. Int. Ed.* **2014**, *53* (51), 14120–14123.

(22) Kim, J.; Kim, B.-K.; Cho, S. K.; Bard, A. J. Tunneling Ultramicroelectrode: Nanoelectrodes and Nanoparticle Collisions. *J. Am. Chem. Soc.* **2014**, *136* (23), 8173–8176.

(23) Amemiya, S.; Bard, A. J.; Fan, F.-R. F.; Mirkin, M. V.; Unwin, P. R. Scanning Electrochemical Microscopy. *Annu. Rev. Anal. Chem.* **2008**, *1* (1), 95–131.

(24) Anderson, T. J.; Zhang, B. Single-Nanoparticle Electrochemistry through Immobilization and Collision. *Acc. Chem. Res.* **2016**, *49* (11), 2625–2631.

(25) Kwon, S. J.; Fan, F.-R. F.; Bard, A. J. Observing Iridium Oxide (IrOx) Single Nanoparticle Collisions at Ultramicroelectrodes. *J. Am. Chem. Soc.* **2010**, *132* (38), 13165–13167.

(26) Xiao, X.; Fan, F.-R. F.; Zhou, J.; Bard, A. J. Current Transients in Single Nanoparticle Collision Events. *J. Am. Chem. Soc.* **2008**, *130* (49), 16669–16677.

(27) Oja, S. M.; Robinson, D. A.; Vitti, N. J.; Edwards, M. A.; Liu, Y.; White, H. S.; Zhang, B. Observation of Multipeak Collision Behavior during the Electro-Oxidation of Single Ag Nanoparticles. *J. Am. Chem. Soc.* **2017**, *139* (2), 708–718.

(28) Zhang, F.; Defnet, P. A.; Fan, Y.; Hao, R.; Zhang, B. Transient Electrocatalytic Water Oxidation in Single-Nanoparticle Collision. *J. Phys. Chem. C* **2018**, *122* (11), 6447–6455.

(29) Brasiliense, V.; Patel, A. N.; Martinez-Marrades, A.; Shi, J.; Chen, Y.; Combellas, C.; Tessier, G.; Kanoufi, F. Correlated Electrochemical and Optical Detection Reveals the Chemical Reactivity of Individual Silver Nanoparticles. *J. Am. Chem. Soc.* **2016**, *138* (10), 3478–3483.

(30) Batchelor-McAuley, C.; Martinez-Marrades, A.; Tschulik, K.; Patel, A. N.; Combellas, C.; Kanoufi, F.; Tessier, G.; Compton, R. G. Simultaneous Electrochemical and 3D Optical Imaging of Silver Nanoparticle Oxidation. *Chem. Phys. Lett.* **2014**, *597*, 20–25.

(31) Sun, L.; Fang, Y.; Li, Z.; Wang, W.; Chen, H. Simultaneous Optical and Electrochemical Recording of Single Nanoparticle Electrochemistry. *Nano Res.* **2017**, *10* (5), 1740–1748.

(32) Noël, J.-M.; Lemineur, J.-F. Optical Microscopy to Study Single Nanoparticles Electrochemistry: From Reaction to Motion. *Curr. Opin. Electrochem.* **2021**, *25*, 100647.

(33) Wilson, A. J.; Devasia, D.; Jain, P. K. Nanoscale Optical Imaging in Chemistry. *Chem. Soc. Rev.* **2020**, *49* (16), 6087–6112.

(34) Willets, K. A.; Van Duyne, R. P. Localized Surface Plasmon Resonance Spectroscopy and Sensing. *Annu. Rev. Phys. Chem.* **2007**, *58* (1), 267–297.

(35) Byers, C. P.; Hoener, B. S.; Chang, W.-S.; Yorulmaz, M.; Link, S.; Landes, C. F. Single-Particle Spectroscopy Reveals Heterogeneity in Electrochemical Tuning of the Localized Surface Plasmon. *J. Phys. Chem. B* **2014**, *118* (49), 14047–14055.

(36) Willets, K. A.; Wilson, A. J.; Sundaresan, V.; Joshi, P. B. Super-Resolution Imaging and Plasmonics. *Chem. Rev.* **2017**, *117* (11), 7538–7582.

(37) Zhang, L.; Li, Y.; Li, D.-W.; Jing, C.; Chen, X.; Lv, M.; Huang, Q.; Long, Y.-T.; Willner, I. Single Gold Nanoparticles as Real-Time Optical Probes for the Detection of NADH-Dependent Intracellular Metabolic Enzymatic Pathways. *Angew. Chem. Int. Ed.* **2011**, *50* (30), 6789–6792.

(38) Biteen, J.; Willets, K. A. Introduction: Super-Resolution and Single-Molecule Imaging. *Chem. Rev.* **2017**, *117* (11), 7241–7243.

(39) Stranahan, S. M.; Willets, K. A. Super-Resolution Optical Imaging of Single-Molecule SERS Hot Spots. *Nano Lett.* **2010**, *10* (9), 3777–3784.

(40) Weber, M. L.; Litz, J. P.; Masiello, D. J.; Willets, K. A. Super-Resolution Imaging Reveals a Difference between SERS and Luminescence Centroids. *ACS Nano* **2012**, *6* (2), 1839–1848.

(41) Weber, M. L.; Willets, K. A. Nanoscale Studies of Plasmonic Hot Spots Using Super-Resolution Optical Imaging. *MRS Bull.* **2012**, *37* (8), 745–751.

(42) Willets, K. A. Super-Resolution Imaging of Interactions between Molecules and Plasmonic Nanostructures. *Phys. Chem. Chem. Phys.* **2013**, *15* (15), 5345–5354.

(43) Tschulik, K.; Batchelor-McAuley, C.; Toh, H.-S.; Stuart, E. J. E.; Compton, R. G. Electrochemical Studies of Silver Nanoparticles: A Guide for Experimentalists and a Perspective. *Phys. Chem. Chem. Phys.* **2013**, *16* (2), 616–623.

(44) Patrice, F. T.; Qiu, K.; Ying, Y.-L.; Long, Y.-T. Single Nanoparticle Electrochemistry. *Annu. Rev. Anal. Chem.* **2019**, *12* (1), 347–370.

(45) Wilson, A. J.; Jain, P. K. Light-Induced Voltages in Catalysis by Plasmonic Nanostructures. *Acc. Chem. Res.* **2020**, *53* (9), 1773–1781.

(46) Andreescu, D.; Kirk, K. A.; Narouei, F. H.; Andreescu, S. Electroanalytic Aspects of Single-Entity Collision Methods for Bioanalytical and Environmental Applications. *ChemElectroChem* **2018**, *5* (20), 2920–2936.

(47) Zamborini, F. P.; Bao, L.; Dasari, R. Nanoparticles in Measurement Science. *Anal. Chem.* **2012**, *84* (2), 541–576.

(48) Ma, H.; Chen, J.-F.; Wang, H.-F.; Hu, P.-J.; Ma, W.; Long, Y.-T. Exploring Dynamic Interactions of Single Nanoparticles at Interfaces for Surface-Confined Electrochemical Behavior and Size Measurement. *Nat. Commun.* **2020**, *11* (1), 2307.

(49) Heuer-Jungemann, A.; Feliu, N.; Bakaimi, I.; Hamaly, M.; Alkilany, A.; Chakraborty, I.; Masood, A.; Casula, M. F.; Kostopoulou, A.; Oh, E.; Susumu, K.; Stewart, M. H.; Medintz, I. L.; Stratakis, E.; Parak, W. J.; Kanaras, A. G. The Role of Ligands in the Chemical Synthesis and Applications of Inorganic Nanoparticles. *Chem. Rev.* **2019**, *119* (8), 4819–4880.

CHAPTER 2: METHODS

2.1 Experimental Section for Chapter 3

Nanoparticles and Fiducials

Citrate stabilized gold nanospheres (100 nm diameter, 0.05 mg/mL in 2 mM sodium citrate) were purchased from nanoComposix. CTAB-stabilized gold nanorods (70 nm diameter, 120 nm length, aspect ratio = 1.7, 50 µg/mL in DI water) were purchased from Nanopartz. Fluorescent nanodiamonds (100 nm, vitrogen vacancy > 900 NV/particle, 1 mg/mL in DI water) were purchased from Sigma Aldrich. Fluorescent sky-blue particles (260 nm, 0.25% w/v in DI water) were purchased from Spherotech.

Silver colloids were prepared following the Lee and Meisel method.[1] First, a 500 mL and 50 mL flask were acid cleaned with aqua regia (1:3 volume mixture of nitric acid: hydrochloric acid). After glassware was cleaned, approximately 45 mg of $AgNO_3$ (ACS Reagent ≥ 99.0%, Sigma Aldrich) was added to the 500 mL flask and dissolved in 250 mL of nanopure water (18 MΩ·cm, arium pro, Sartorius). This solution was then heated to a boil. In the 50 mL flask, 5 mL of a 10% w/w solution of sodium citrate (ACS Reagent ≥ 99.0%, Sigma Aldrich) was prepared and added to the solution in the 500 mL flask. This combined mixture was boiled for 1 hour being sure to continuously add in extra nanopure water that is lost during the boiling process. The Ag colloid solution appears cloudy gray in color when finished. This solution can be stored in the flask or a secondary container, however, covering and limiting light exposure will help maintain the quality of the particles.

Preparation of Substrates

Glass coverslips (premium coverglass No. 1, 25 x 25 mm) were purchased from Fischer Scientific. Indium-tin oxide coated glass coverslips (ITO, #1 thickness, 22 x 22 mm, 15-30 Ω/sq. resistivity) were purchased from SPI Supplies. Both glass and ITO coverslips were sequentially cleaned by sonicating 15 minutes each in acetone, iso-propanol, and then nanopure water. All coverslips were dried with N_2 and O_2 plasma cleaned (Harrick Plasma, Plasma Cleaner PDC-32G) for 10 minutes prior to use.

Rotating Calcite Crystal Setup

For all CLocK studies, a birefringent calcite crystal (Thor Labs, Mounted Calcite Beam Displacer, BD27 – 2.7 mm beam separation) housed in a motorized rotary mount (QIOPTIQ, Rotary Mount with Servo Motor) was placed in the infinity space of an inverted optical microscope (Olympus, IX-73, two-deck system) between the objective and tube lens. The rotation rate of the motorized rotary mount was controlled by a precision DC voltage source (Stanford Research Systems, Model DC205) and monitored using an intelligent digital tachometer (Buyee, DT-2234C$^+$). Importantly, the rotation rate of the motorized rotary mount was set to equal the acquisition rate of the EM-CCD camera (Andor, iXon Life 897) (i.e. the rotations-per-minute (RPM) reading from the tachometer was equal to the acquisition rate of the camera).

CLocK Microscope Setups

Dark-field CLocK images (Figure 2.1A) were collected by passing white light from a tungsten-halogen source through a dark-field condenser (Olympus) to illuminate a sample of metal NPs on either a glass or ITO coverslip. Low angle light scattered from the NPs

was collected by a 100X objective (Olympus, oil immersion, 0.6 NA), passed along the optical path through the rotating calcite crystal, tube lens, and a relay lens before imaging onto the EM-CCD camera.

In fluorescence (Figure 2.1B) and single molecule SERS (SM-SERS) CLocK studies, samples were illuminated with a circularly polarized 532 nm continuous wave laser in a through-the-objective epi-illumination configuration. The resulting emission was collected by the same objective (Olympus, oil immersion, 1.3 NA), passed along the optical path through a dichroic mirror, the rotating calcite crystal, a 532 long-pass filter, and a relay lens before being imaged onto the EM-CCD camera.

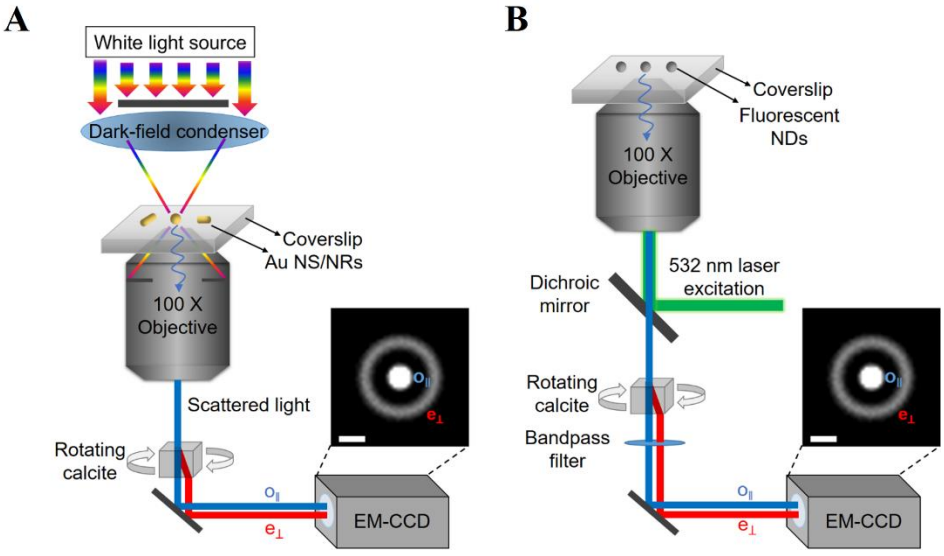

Figure 2.1. Scheme of CLocK microscopy in (A) dark-field and (B) fluorescence configurations. In both configurations, as the light scattered or emitted from the sample and passes through the rotating calcite crystal, the incident light is split into two orthogonal rays, an ordinary ($o_{||}$) and extraordinary ($e_{\perp}$). The $o_{||}$ appears as a diffraction limited spot while the $e_{\perp}$ sweeps out a ring creating the distinct CLocK point spread function. Scale bars = 1 μm.

Super-localization of $o_{\parallel}$

The center position of the $o_{\parallel}$ was determined by fitting the diffraction limited spot of the CLocK point spread function (PSF) to a two-dimensional (2-D) Gaussian equation (Equation 2.1):

$$I = z_0 + I_0 e^{-\frac{1}{2}\left[\left(\frac{x-x_0}{\sigma_x}\right)^2+\left(\frac{y-y_0}{\sigma_y}\right)^2\right]} \qquad \text{(Eq. 2.1)}$$

where I is the intensity of the diffraction-limited spot ($o_{\parallel}$), z_0 is the background intensity, σ_x and σ_y are the standard deviation (or width) of the diffraction-limited spot, and x_0 and y_0 are the approximated center position of the $o_{\parallel}$.

Simulated CLocK Images*

*For completeness of discussion in Chapter 3 of this dissertation, the procedure for simulating CLocK images is described below; however, the simulations were performed by Zachary J. O'Dell and Sanjay Sridhar.

In CLocK microscopy, the angle-dependent intensity of the ordinary ray, $I_{o_{\parallel}}(\theta)$, and extraordinary ray, $I_{e_{\perp}}(\theta)$, are defined using Equation 2.2 and Equation 2.3, respectively:

$$I_{o_{\parallel}}(\theta) = WI_0\cos^2(\theta-\varphi+90) + (1-W)I_0\cos^2(\theta-\varphi) \qquad \text{(Eq. 2.2)}$$

$$I_{e_{\perp}}(\theta) = WI_0\cos^2(\theta-\varphi) + (1-W)I_0\cos^2(\theta-\varphi+90) \qquad \text{(Eq. 2.3)}$$

where W is a constant between 0.5 – 1 used to describe the degree of anisotropy of the emitter/scatterer, I_0 is a constant value representing the intensity, θ is the (varying) orientation of the calcite crystal, and φ is the fixed orientation of the emitter/scatterer. For an isotropic emitter/scatterer (W = 0.5), $I_{o_{\parallel}}$ and $I_{e_{\perp}}$ are equal at all values of θ, leading to the uniform intensity observed in the $e_{\perp}$ pattern (Figure 2.2A). For an anisotropic emitter/scatter ($0.5 < W \leq 1$), $I_{o_{\parallel}}$ and $I_{e_{\perp}}$ will have different values depending on the value

of θ, leading to the intensity modulation or lobing observed in the $e_\perp$ pattern (Figure 2.2B). The entire CLocK PSF can be modelled using Equation 2.4:

$$PSF = \int_0^{2\pi} \left(I_{o_\parallel}(\theta) e^{-\frac{1}{2}\left[\left(\frac{x-x_{0\,o_\parallel}}{\sigma_x}\right)^2+\left(\frac{y-y_{0\,o_\parallel}}{\sigma_y}\right)^2\right]} + I_{e_\perp}(\theta) e^{-\frac{1}{2}\left[\left(\frac{x-x_{0\,e_\perp}}{\sigma_x}\right)^2+\left(\frac{y-y_{0\,e_\perp}}{\sigma_y}\right)^2\right]} \right) d\theta \quad \text{(Eq. 2.4)}$$

where *x* and *y* are Cartesian coordinates within the CLocK image, $x_{0\,o_\parallel}$ and $y_{0\,o_\parallel}$ are the (fixed) center coordinates of the $o_\parallel$, and σ_x and σ_y are the width of the Gaussian in the *x* and *y* direction, respectively. $x_{0\,e_\perp}(\theta)$ and $y_{0\,e_\perp}(\theta)$ are the angle-dependent center coordinates of the $e_\perp$, defined by Equation 2.5 and Equation 2.6, respectively:

$$x_{0\,e_\perp}(\theta) = x_{0\,o_\parallel} + dsin(\theta) \quad \text{(Eq. 2.5)}$$

$$y_{0\,e_\perp}(\theta) = y_{0\,o_\parallel} + dcos(\theta) \quad \text{(Eq. 2.6)}$$

where *d* is the distance between the $o_\parallel$ center and $e_\perp$ center.

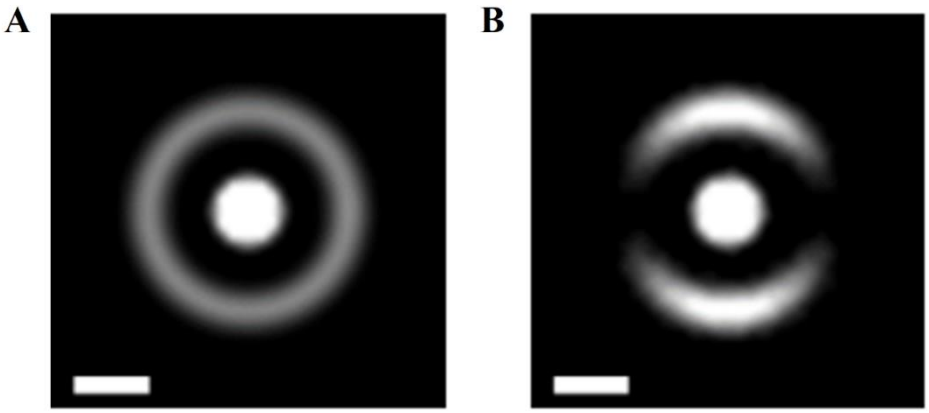

Figure 2.2. Simulated CLocK images for an (A) isotropic and (B) anisotropic emitter/scatter. Scale bars = 1 μm.

CLocK Polarization and Orientation Experimental Procedure

A solution of Au NSs and Au NRs was prepared by mixing 5 µL of Au NSs and 50 µL of Au NRs in 470 µL of nanopure water. A solvent- and plasma-cleaned glass coverslip was then spin-coated with 15 µL of the dilute sample of Au NPs.

Optical images were captured utilizing the dark-field setup described above. The calcite crystal was set to rotate at a speed of 200 RPM (3.33 Hz), and the acquisition rate of the camera was set to capture an image every 300 ms (3.33 Hz).

Colored CLocK Images Experimental Procedure

A mixture of Au NSs and Au NRs was prepared by mixing 5 µL of Au NSs and 50 µL of Au NRs in 470 µL of nanopure water which was then spin-coated (3,000 rpm for 60 s) onto an ITO coverslip with an asymmetric 'A' etched onto it to allow for correlated optical, single-particle spectroscopy, and electron microscopy studies.

For optical studies, the calcite crystal was set to rotate at a speed of 200 RPM (3.33 Hz), and the acquisition rate of the camera was set to capture an image every 300 ms (3.33 Hz). To obtain spectral information in these optical images, a rotational filter wheel equipped with several bandpass filters (Edmund Optics) was inserted into the optical path before the relay lens. A total of 10 images were obtained with each bandpass filter: 466 ± 20 nm, 520 ± 18 nm, 562 ± 20 nm, 585 ± 20 nm, 607 ± 18 nm, 655 ± 20 nm, and 692 ± 20 nm. For each image, the $o_{\parallel}$ was fit to Equation 2.1 to approximate the center position. To isolate the intensity contributions of the $o_{\parallel}$ and $e_{\perp}$, circles of increasing radii (1 – 20 pixels) were overlaid on top of the CLocK PSF, centered on the $o_{\parallel}$. The $o_{\parallel}$ intensity was attributed to intensity values within a 3σ pixel radius of the center of the $o_{\parallel}$, while the $e_{\perp}$ intensity was attributed to intensity values 10.7 ± 3σ pixels from the $o_{\parallel}$ center. While the intensity

within the rings of the $o_{\parallel}$ are integrated to a single intensity value, the intensity of the $e_{\perp}$ is broken into 18 (20°) segments and integrated leading to 18 $e_{\perp}$ intensity values for a CLocK PSF (Figure 2.3A). These 18 segments can be plotted as a function of orientation and fit to Equation 2.7:

$$I_{\theta} \propto 1 + Mcos\{2(\theta - \varphi)\} \qquad \text{(Eq. 2.7)}$$

where I_{θ} is the background-subtracted intensity of the $e_{\perp}$ as a function of θ, the orientation of the polarizer, *M* is the modulation depth, and φ is the orientation of the particle (Figure 2.3B, C). The θ value of maximum intensity calculated from Equation 2.7 can be used to identify the 20° intensity segment corresponding to the orientation of longitudinal axis of the NR ($\theta = \varphi$, $e_{\perp\,long}$), as well as the 20° intensity segment corresponding to the orientation of the transverse axis of the NR ($\theta = \varphi + 90$, $e_{\perp\,trans}$).

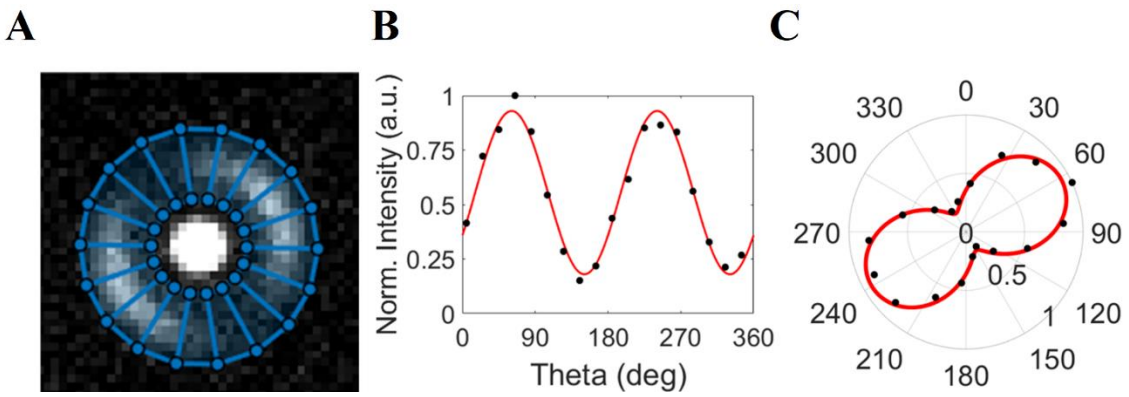

Figure 2.3. (A) The $e_{\perp}$ is segmented into 18 (20°) segments in which the intensity within each segment is integrated and normalized to give 18 unique data points. (B) Cartesian plot of Equation 2.7 fit (red) and normalized intensity (black) plotted as a function of θ. (C) Polar plot of Equation 2.7 fit (red) and normalized intensity (black) plotted as a function of θ.

For single-particle polarized-resolved dark-field scattering spectra were collected using an Olympus IX-71 inverted microscope. Light from the built-in halogen lamp passed through a dark-field condenser (Olympus, IX-ADUCD) and illuminated the Au NP on an

ITO. Scattered light from the Au NPs was collected using a 100X objective (Olympus, oil-immersion, 0.6 NA), and imaged onto a spectrometer (Princeton Instruments 2500i) and liquid nitrogen cooled camera (Princeton Instruments, Spec-10). Spectra were collected using a 20 s integration time. For each particle, an unpolarized emission spectra was captured, as well as seven linearly polarized emission spectra at angles of 40°, 70°, 100°, 130°, 160°, 190°, and 220° (Melles Griot 07 HPR 223 Polarizer Rotation Mount, BMI Surplus).

CLocK Imaging of SM-SERS Experimental Procedure

SM-SERS samples were prepared following a previously developed procedure in our lab.[2] First, 200 µL of 50 nM rhodamine 6G (R6G) in methanol was added to 2 mL of silver colloids that were prepared as describe above. We vortexed this mixture for 30 s and then added 2 mL of a 33 mM NaCl (BioXtra, ≥ 99.5% (AT), Sigma-Aldrich) solution to induce aggregation of the colloids. Prior to imaging, 200 µL of 286 x diluted sky-blue fluorescent beads was added (serving as alignment markers for analysis) to the mixture which was then vortexed again for 30 s. Finally, we spin-coated 10 µL of the SM-SERS solution at 3000 rpm for 1 min onto a clean glass coverslip for imaging.

In the dark-field setup, the calcite crystal was set to rotate at a speed of 200 RPM (3.33 Hz), and the EM-CCD acquisition rate was set to capture an image every 300 ms (3.33 Hz). In the SM-SERS setup, the calcite crystal was set to rotate at a speed of 60 RPM (1 Hz), and EM-CCD acquisition rate was set to capture an image every 1 s (1 Hz). A total of 180 frames (180 s) of SM-SERS events were captured.

In MATLAB, the o_I intensity of all 180 frames of the SM-SERS movie were compared to identify 'off' frames, where the o_I intensity is solely attributed to the

photoluminescence of the Ag colloid, and 'on' frames, where intensity is attributed to a combination of the photoluminescence of the Ag colloid and a R6G SM-SERS event. Every frame, whether 'off' or 'on', was fit to a 2-D Gaussian using Equation 2.1. All 'on' and 'off' events fits are benchmarked to a R^2 value of 0.90, and frames that do not meet this threshold are disregarded. CLocK images of R6G SM-SERS events are obtained by subtracting the nearest 'off' frame from each 'on' frame, eliminating the intensity contribution of the Ag colloid photoluminescence and isolating the intensity contribution of the R6G SM-SERS event.

For non-background subtracted CLocK images, the $e_{\perp}$ intensity was calculated by finding the pixel of maximum intensity along 120 straight lines separated by 3° increments between 3σ - 10.7 pixels and 3σ + 10.7 pixels from the o_{I} center. This leads to 120 individual $e_{\perp}$ intensity values for each CLocK PSF, where each value represents the sum of the identified pixel of maximum intensity and its eight nearest neighbors. The orientation of the line can be related to a time in the image, where t_0 is arbitrarily defined as 3 o'clock and time rotates clockwise.

CLocK Temporal Model Experimental Procedure

A sample of fluorescent nanodiamonds was created by adding 5 µL of fluorescent nanodiamonds to 245 µL of nanopure water. A solvent- and plasma-cleaned glass coverslip was then spin-coated with 15 µL of the fluorescent nanodiamonds solution.

To capture optical images, the calcite crystal was set to rotate at a speed of 375 RPM (6.25 Hz), and the acquisition rate of the camera was set to capture an image every 160 ms (6.25 Hz). To control the arc length of the $e_{\perp}$ (simulating kinetic events of various times), a VS25 25 mm optical shutter (Uniblitz) powered by a VCM-D1 shutter driver

(Uniblitz) was inserted into the optical path before the relay lens. The shutter driver was controlled using a 20 MHz function / arbitrary waveform generator (Agilent, Model 33220A) and synced to the EM-CCD camera such that the waveform generator would initiate at the start of each data collection. The waveform generator was set to the pulse wave setting, where the period of the pulses was set to equal the accumulation cycle time (160.897 ms), rather than 160 ms to account for the readout delay of the EM-CCD camera in between subsequent frames. The amplitude of the pulse wave was set to 5 V, the offset set to 0 V, and the edge time set to 5.0 ns. The width of the pulse dictated the arc length of the $e_{\perp}$, for example a width of 80 ms would lead to a 180° arc length for an acquisition time of 160 ms. For each $e_{\perp}$ arc length sampled (5°, 10°, 15°, 22.5°, 45°, 67.5°, 90°, 112.5°, 135°, 157.5°, 180°, 202.5°, 225°, 247.5°, 270°, 292.5°, 315°, 337.5°, 345°, 350°, and 360°), 24 CLocK images were captured.

2.2 Experimental Section for Chapter 4

Chemicals and Materials

Commercial Ag NPs used in this study are 70 nm citrate-capped silver nanospheres (73 ± 7 nm diameter, $\lambda_{max} = 442$ nm) purchased from nanoComposix. Conductive silver epoxy (Electrically/Thermally Conductive Bond 556) was purchased from Electron Microscopy Science. Glass coverslips (25 x 25 mm, thickness no.1), a two-part silicone elastomer (SYLGARD 184) and two-part epoxy adhesive (DEVCON 5-minute epoxy) were purchased from Fisher Scientific. Platinum wire (2 mm diameter) used for reference and counter electrodes was purchased from Alfa Aesar. Sodium citrate tribasic dehydrate (ACS Reagent, ≥99.0%), citric acid (BioUltra, anhydrous, ≥99.5%), sodium sulfide, and

sodium hydroxide (BioXtra, ≥98%) were purchased from Sigma-Aldrich. All solutions were prepared with nanopure water (18 MΩ·cm, arium pro, Sartorius).

Preparation of Transparent Gold-film Substrates

Transparent gold-film substrates used as the working electrode in these experiments were prepared in-house using a Kurt J. Lesker Nano 36 thermal evaporation system. First, glass coverslips were sequentially cleaned by sonicating 20 minutes each in acetone, iso-propanol, and then nanopure water. Coverslips were then dried with N_2 and O_2 plasma cleaned (Harrick Plasma, Plasma Cleaner PDC-32G) for 15 minutes and taped (Cole-Parmer, Kapton Tape w/ Silicone Adhesive) down on a rotating mount for deposition of the gold film. We deposit the gold in a two-step process: first, 3 nm of chromium (Lesker, chrome plated tungsten rod, 4" length x 0.050" diameter) was thermally evaporated at a rate of 1.0 Å s^{-1} to serve as sticking layer between the glass coverslip and gold; second, a 30 nm layer of gold (Ted Pella, 0.008" diameter) was thermally evaporated at a rate of 5.0 Å s^{-1}. The conditions as outlined produce a uniform coverage of gold that is reproducibly transparent for correlated optical studies as seen by the transmission spectra in Figure 2.4.

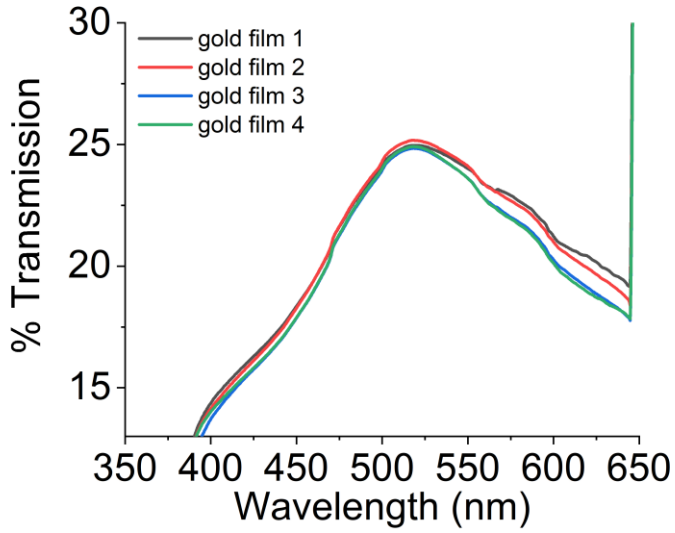

Figure 2.4. Transmission spectra for thermally deposited gold-smooth films on glass coverslips for films taken from different deposition batches.

Synthesis of Silver-Sulfide Shells on Silver Nanoparticles

The sacrificial silver-sulfide shells used in this study were grown chemically in solution by mixing 553 µL of a 9 pM stock Ag NP solution, 250 µL of 100 mM NaOH, a varying amount of 500 µM Na_2S (to create desired concentration of HS^-) and the appropriate amount of nanopure water to make a 1 mL reaction solution. NPs were allowed to react in ambient conditions for 30 minutes prior to drop casting 15 µL on our gold-film working electrodes which were then dried on a hotplate at low heat. A noticeable color change in the NP solution of yellow to red was observed as increasing amounts of Na_2S was added (Figure 2.5). Our synthesis protocol was inspired by previously reported work by the White group.[3]

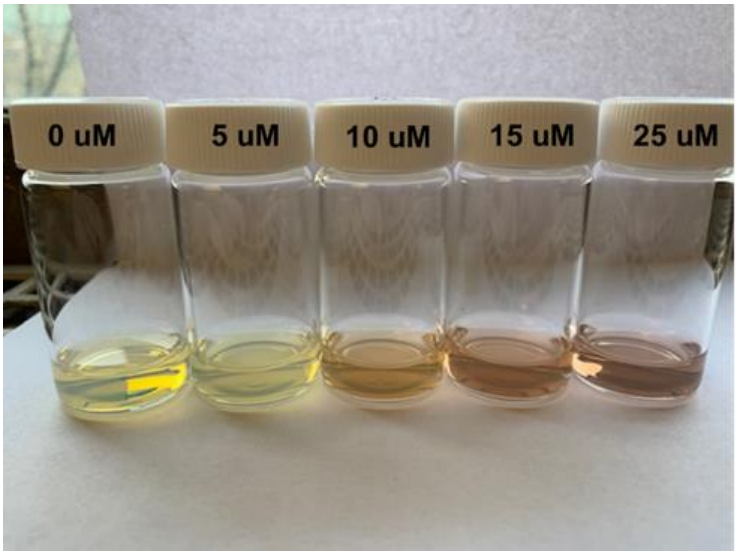

Figure 2.5. Solutions of Ag NPs reacted with varying amounts of Na_2S. The noticeable color change in solution of yellow to red occurs with the addition of increasing amounts of Na_2S is consistent with the formation of Ag_2S.

TEM and HR-TEM Imaging of Nanoparticles

TEM images of unreacted Ag NPs and Ag NPs reacted with 50 µM HS^- were collected on a JOEL JEM 1400 operating at 120 kV. Both TEM samples were prepared by drop casting 10 µL of the nanoparticle solutions on a copper mesh TEM grid which were then dried on a hot plate with low heat until the solution evaporated. These images were collected by Qilin Wei in the Sun Group at Temple University.

High resolution TEM (HR-TEM) imaging and scanning TEM energy-dispersive X-ray spectroscopy (STEM-EDS) analysis were performed on a 300-kV JEOL JEM 3200FS TEM equipped with a Gatan 4k × 4k Ultrascan 4000 camera and a DE-64 direct electron camera from Direct Electron. Samples of unreacted Ag NPs and Ag NPs reacted with 50 µM HS^- were prepared by drop casting 10 µL of the nanoparticle solutions on a copper mesh TEM grid which were then dried on a hot plate with low heat until the solution evaporated. TEM grids were then packaged in an air-tight bag and shipped to Indiana

University for analysis. These images were acquired by Jun Chen in the Ye group at Indiana University.

Electrochemical Cell

The cell used for correlated electrochemical and optical experiments was prepared by attaching a copper wire lead to the transparent gold-film substrate using an electrically conductive silver epoxy and would serve as the working electrode for all experiments. A two-part, 5-minute epoxy adhesive was used to attach a silicon elastomer well (outer dimensions of well: 20 x 15 x 4 mm, inner dimensions: 11 x 7 mm) to the working electrode to house the imaging buffer solution (10 mM citrate buffer, pH 9). Two separate Pt wires were inserted through the side walls of the well to act as the quasi-reference and counter electrodes. The three electrodes were externally connected to a potentiostat (CH Instruments, CHI750E) for precise potential control. The Pt reference electrodes were calibrated to a standard reference electrode, Ag|AgCl, by performing bulk cyclic voltammetry of ferrocyanide in potassium chloride (Sigma Aldrich) (Figure 2.6).

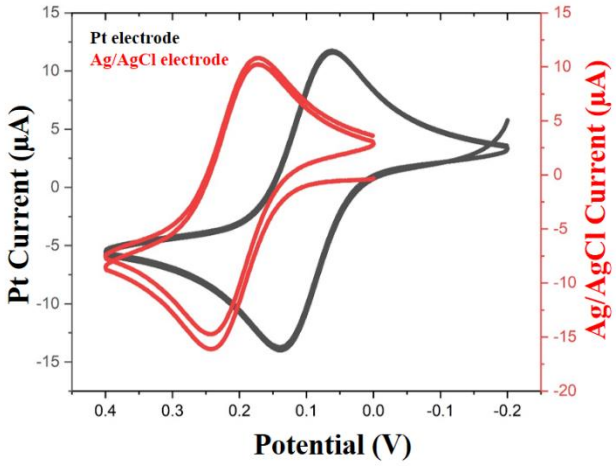

Figure 2.6. Bulk cyclic-voltammogram (CV) to calibrate the quasi-reference Pt electrode used in experiments against a standard reference electrode, Ag/AgCl. From these bulk CV's we observed a 0.107 V shift when comparing Pt to standard Ag/AgCl.

Dark-Field Microscope Setup

Dark-field scattering images were collected using a similarly described setup in previous work from out lab.[4,5] Here, an inverted microscope (Olympus, IX-73) equipped with a 100X objective (Olympus, oil immersion, 0.6 NA), a tungsten-halogen white light source and a dark-field condenser (Olympus, U-DCD) (Figure 2.7). White light passes through the dark-field condenser illuminating the electrochemical cell that is decorated with Ag or Ag@AgNPs. Low angle light that is scattered from the NPs is collected by the objective and imaged onto an EM-CCD camera (Andor, iXon Life). The resulting dark-field image has a dark background with bright spots that each represent diffraction-limited NPs. The camera acquisition for all experiments was set to 0.1 s and externally synchronized with the potentiostat such that correlated optical and electrochemical measurements could be obtained.

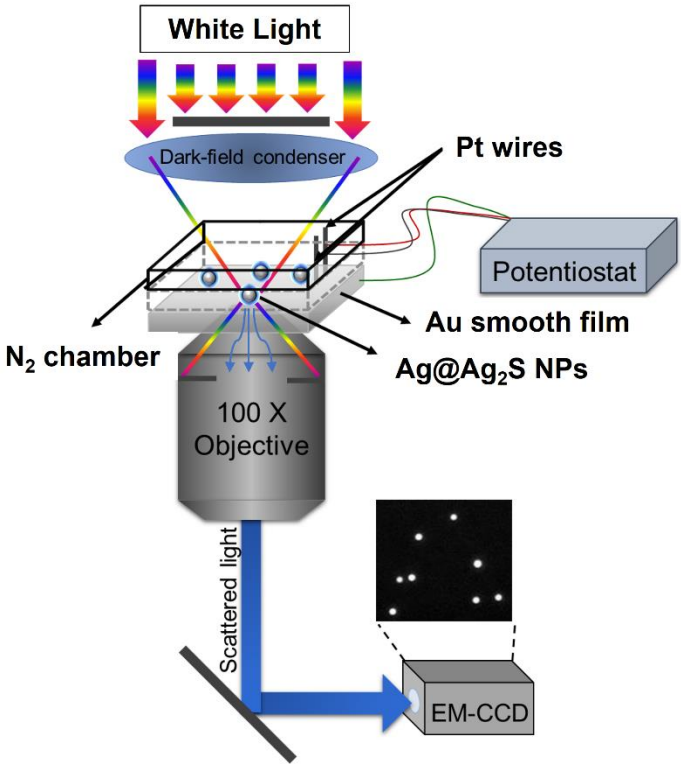

Figure 2.7. General schematic of the experimental and dark-field microscope setup. Electrochemical setup: The electrochemical cell consists of Ag@Ag_2S NPs drop-cast onto a Au film (working electrode) and two Pt wires (reference and counter electrodes) inserted through the sides of an elastomer well that contains our imaging buffer (10 mM Citrate buffer, pH 9). The cell is placed on top of an inverted optical microscope. A home-made N_2 flow chamber is used to create a nitrogen blanket over the cell and prevent O_2 from interacting with the Ag NPs. Optical setup: White light passes through the dark-field condenser to illuminate the working electrode with dispersed NPs. The low angle light scattered from the NPs is collected through a 100X objective and imaged onto an EM-CCD camera. The resulting dark-field image produces a dark background with bright spots that represent the electrode surface and the location of diffraction limited Ag NPs, respectively. By synchronizing the collection of images from the camera with a potentiostat, we can monitor changes in scattering intensities with an applied potential.

2.3 References

(1) Lee, P. C.; Meisel, D. Adsorption and Surface-Enhanced Raman of Dyes on Silver and Gold Sols. *J. Phys. Chem.* **1982**, *86* (17), 3391–3395.

(2) Stranahan, S. M.; Willets, K. A. Super-Resolution Optical Imaging of Single-Molecule SERS Hot Spots. *Nano Lett.* **2010**, *10* (9), 3777–3784.

(3) Robinson, D. A.; White, H. S. Electrochemical Synthesis of Individual Core@Shell and Hollow Ag/Ag_2S Nanoparticles. *Nano Lett.* **2019**, *19* (8), 5612–5619.

(4) Sundaresan, V.; Monaghan, J. W.; Willets, K. A. Visualizing the Effect of Partial Oxide Formation on Single Silver Nanoparticle Electrodissolution. *J. Phys. Chem. C* **2018**, *122* (5), 3138–3145.

(5) Sundaresan, V.; Monaghan, J. W.; Willets, K. A. Monitoring Simultaneous Electrochemical Reactions with Single Particle Imaging. *ChemElectroChem* **2018**, *5* (20), 3052–3058.

CHAPTER 3: CALCITE-ASSISTED LOCALIZATION AND KINETICS (CLocK) MICROSCOPY[1]

3.1 Introduction

Localization-based super-resolution imaging is now well-established as a powerful tool to overcome the diffraction limit of light by analyzing single emitter point-spread functions (PSFs) to determine the spatial position associated with the point of highest intensity, leading to new insights in fields ranging from biology to material science.[1–13] The position of highest intensity is approximated as the location of the single emitter and, given sufficient signal to noise, can have spatial precision better than 10 nm.[14–17] Repeating the process for many single emitters allows for super-resolved images to be constructed, allowing us to break the resolution barrier of traditional optical microscopes and discover unseen structure and processes with nanoscale resolution.

One challenge with this approach is that a diffraction-limited spot encodes limited information about the emitter—typically only its spatial position and intensity (as in Figure 3.1A). However, additional information about the emitter, such as its orientation and extent of anisotropy, is desired for systems where rotational motion or dynamic changes in anisotropy can occur.[18–23] While it is possible to extract additional anisotropy and orientation information from a diffraction-limited image of a dipole emitter by fitting it to a 3-D dipole emission pattern, this requires extremely high signal-to-noise or image defocusing, which introduces complexities with localization analysis.[24–27] Alternative

[1] Reprinted with permission from J.W. Monaghan, Z.J. O'Dell, S. Sridhar, B. Paranzino, V. Sundaresan, K.A. Willets. "Calcite-Assisted Localization and Kinetics (CLocK) Microscopy", *J. Phys. Chem. Lett.* **2022**. *13 (45)*, 10527-10533. Copyright 2022 American Chemical Society.

strategies for extracting orientation and polarization information involve using phase masks in the emission path of the microscope, but these are challenging to design, yield complex PSFs that can be non-intuitive to analyze, and are often sensitive to the emission wavelength of the species of interest as well as the optical properties of the microscope.[23,28] Inserting a rotating wedge polarizer into the emission path of a microscope simplifies this problem, but loses the simplicity of localizing a single emitter by fitting its diffraction-limited emission.[29] A fourth approach involves splitting the diffraction-limited emission between two polarization channels, but this makes image registration difficult, especially in situations where the localized position of the emitter is polarization dependent (as our group has observed with fluorescent beads).[30–33] Moreover, splitting the emission is best suited for homogenous populations of dipole emitters (like single fluorophores) and is less successful in heterogeneous systems with variations in anisotropy (such as nanoparticles) where ambiguity in the polarization-resolved images can occur (Figure 3.1B).

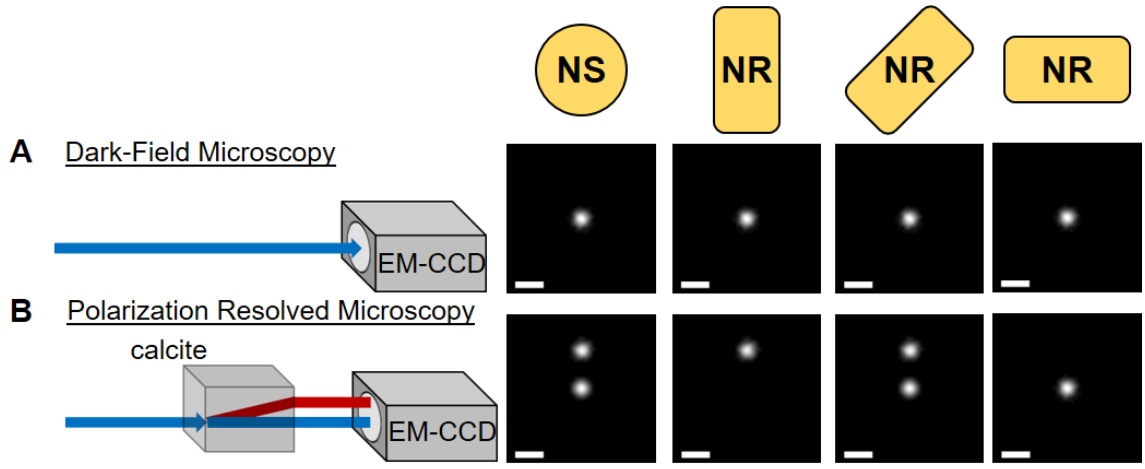

Figure 3.1. Comparison of the simulated PSFs for an isotropic nanospheres (NS) and anisotropic nanorods (NRs) at different orientations (φ = 0°, 45°, and 90°) imaged using (A) dark-field microscopy, where the diffraction limited spots are identical for an isotropic NS or anisotropic NR (B) polarization resolved microscopy using a stationary calcite crystal as the polarization analyzer (θ = 0°) where the PSFs for an isotropic NS and anisotropic NR at φ = 45° are similar. Scale bars = 1 μm.

Herein, we discuss calcite-assisted localization and kinetics (CLocK) microscopy, a multi-parameter super-resolution imaging technique that generates a polarization-averaged diffraction-limited image surrounded by a polarization-resolved ring, allowing both localization/intensity and anisotropy/orientation information to be extracted from a single image. CLocK microscopy relies on the birefringent nature of a rotating calcite crystal, which is inserted into the infinity space of the optical microscope (Figures 3.2). Light collected by the microscope objective passes through the calcite crystal and is split into two orthogonally-polarized rays: an ordinary ray ($o_{\parallel}$) that continues along the original emission path and a spatially-displaced extraordinary ray ($e_{\perp}$), where $\parallel$ and $\perp$ represent the polarization states of the two rays relative to each other. As the calcite crystal rotates at a rate equal to the acquisition rate of the imaging camera, the $e_{\perp}$ sweeps out a complete 360° ring around the stationary $o_{\parallel}$, creating a unique PSF that resembles a 'clock' (Figure 3.2), inspiring the name of the technique (for the sake of completeness, we note that this approach will work for other birefringent materials in addition to calcite).

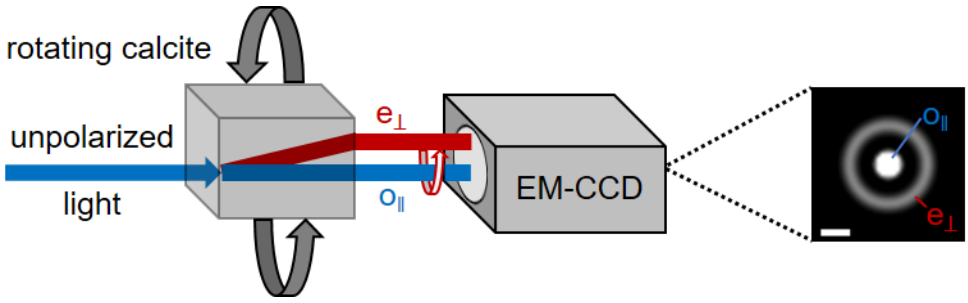

Figure 3.2. Schematic representation of CLocK microscopy in which emission passes through a rotating calcite crystal, splitting it into mutually perpendicular polarizations: a stationary $o_{\parallel}$ ray and a spatially offset $e_{\perp}$ ray. As the calcite crystal rotates, the $e_{\perp}$ ray sweeps out a ring around the stationary $o_{\parallel}$ ray, producing a CLocK image that can be read out by a camera (EM-CCD). Scale bars 1 μm.

3.2 Working Principal of CLocK Microscopy

During the calcite crystal rotation, the linear polarizations probed by the $o_{\parallel}$ and the $e_{\perp}$ change as a function of calcite crystal orientation (θ), while remaining mutually perpendicular. For an isotropic object, such as a nanosphere (NS), the intensity of the $o_{\parallel}$ and $e_{\perp}$ will be equal at all values of θ, leading to uniform intensity in the $e_{\perp}$ ring that surrounds the polarization-averaged $o_{\parallel}$ image (Figure 3.3-i). However, for anisotropic objects such as nanorods (NRs), which preferentially scatter light along their longitudinal axis, the intensity of $o_{\parallel}$ and $e_{\perp}$ will modulate as a function of θ, leading to an angle-dependent broken ring pattern in the $e_{\perp}$ that corresponds to the orientation (φ) of the longitudinal axis of the NR (Figure 3.3-ii-iv).

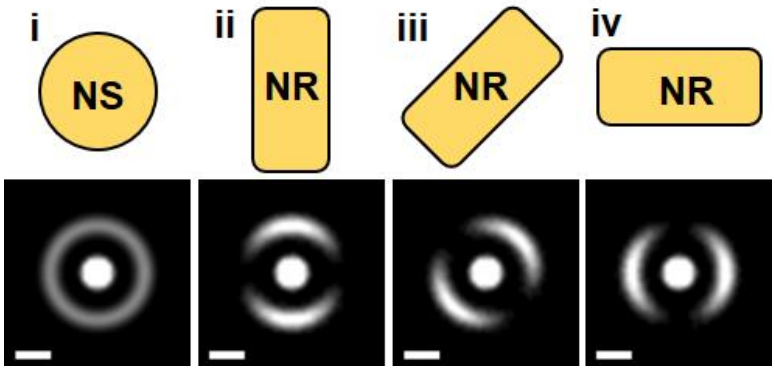

Figure 3.3. Simulated CLocK images for an (i) isotropic nanosphere (NS) and (ii-iv) anisotropic nanorods (NRs) with varying orientations (φ = 0°, 45°, and 90°). The calcite crystal acts as polarization analyzer, leading to distinct patterns in the CLocK images. Scale bars 1 μm.

Moreover, CLocK is compatible with multiple forms of optical microscopy, including dark-field scattering, fluorescence, and Raman scattering (Figure 3.4 and *vide infra*). For dark-field scattering (Figure 3.4A), white light is passed through a dark-field condenser to illuminate a sample of metal NPs, like gold nanospheres or nanorods (Au NS/NRs). Low-angle light that is scattered from individual NPs is collected by the

objective, passed through the rotating calcite, and imaged onto a camera, in our case an electron multiplication charged-coupled device (EM-CCD). For fluorescence (Figure 3.4B), samples like fluorescent nanodiamonds (NDs) are illuminated by a polarized light source (here we use a 532 nm laser shown in an epi-illumination geometry), where the resulting emission is collected by an objective, passed through a dichroic mirror, the rotating calcite, a bandpass filter, and then imaged onto an EM-CCD camera.

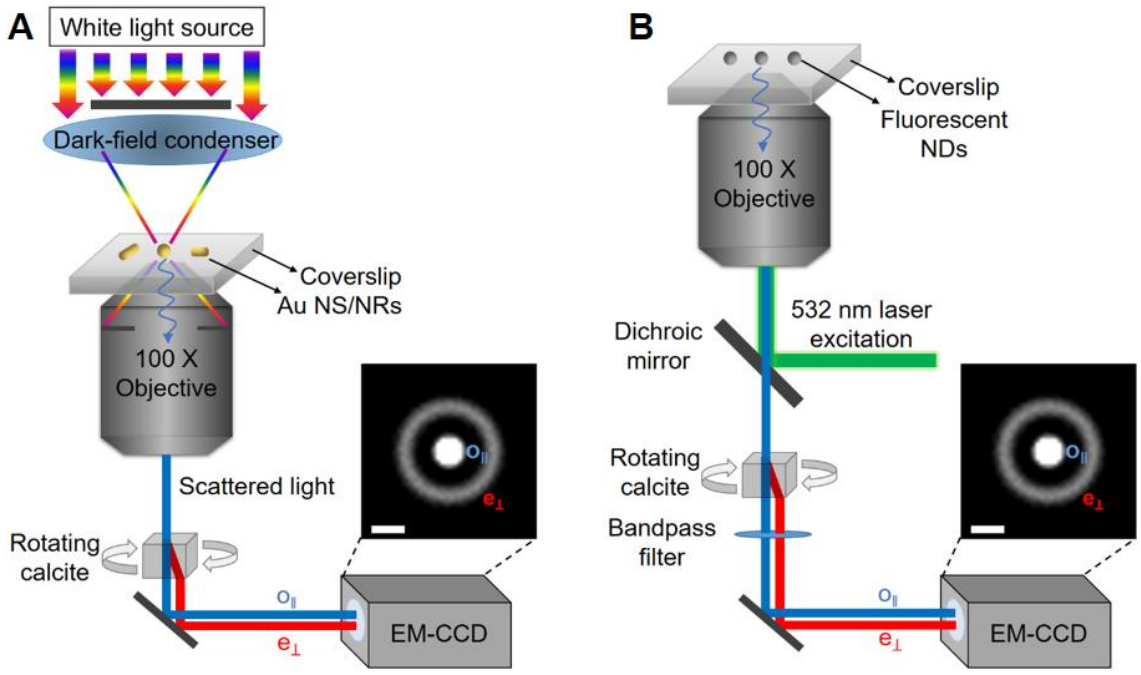

Figure 3.4. Scheme of CLocK microscopy in (A) dark-field and (B) fluorescence configurations. Scale bars = 1 μm.

As this technique is a super-resolution based approach, it is essential to note that optical images captured using CLocK microscopy reveal polarization and orientation information from the $e_{\perp}$ without sacrificing the ability to localize the polarization-averaged centroid of the $o_{\parallel}$ using traditional methods, such as fitting with a two-dimensional Gaussian (Equation 3.1):

$$I = z_0 + I_0 e^{-\frac{1}{2}\left[\left(\frac{x-x_0}{\sigma_x}\right)^2 + \left(\frac{y-y_0}{\sigma_y}\right)^2\right]} \quad \text{(Eq. 3.1)}$$

where I is the intensity of the diffraction-limited spot ($o_{\parallel}$), z_0 is the background intensity, σ_x and σ_y are the standard deviation (or width) of the diffraction-limited spot, and x_0 and y_0 are the approximated center position of the $o_{\parallel}$. We demonstrate the localization precision of CLocK microscopy in both dark-field scattering and fluorescence by comparing the fits of the diffraction limited spots with and without a rotating calcite present in the imaging path (Figure 3.5). In fluorescence, we used an optical shutter to test different degrees of $e_{\perp}$ collection angles, which correlates to time of an event captured (see section 3.5 for further discussion), to test how less signal from short-lived events impacts the ability to localize. For most cases, the localization of the CLocK $o_{\parallel}$ is not statistically different from the localization of a traditional diffraction-limited spot of the same emitter/scatterer. One of two exceptions is shown for the dark-field scattering example in Figure 3.5A, where the localization of the CLocK $o_{\parallel}$ in the *y*-direction has a narrower distribution than the localization of the equivalent traditional diffraction-limited spot. The second exception is in fluorescence when only 12° of the $e_{\perp}$ is collected in Figure 3.5D, where the localization of the CLocK $o_{\parallel}$ in the *y*-direction is broadened due to the inability of the imaging processing algorithm to discriminate the diffraction-limited $o_{\parallel}$ and $e_{\perp}$ resulting in poor quality fits to the data. The localization precision in both x- and y- directions for each imaging condition is summarized in Table 3.1.

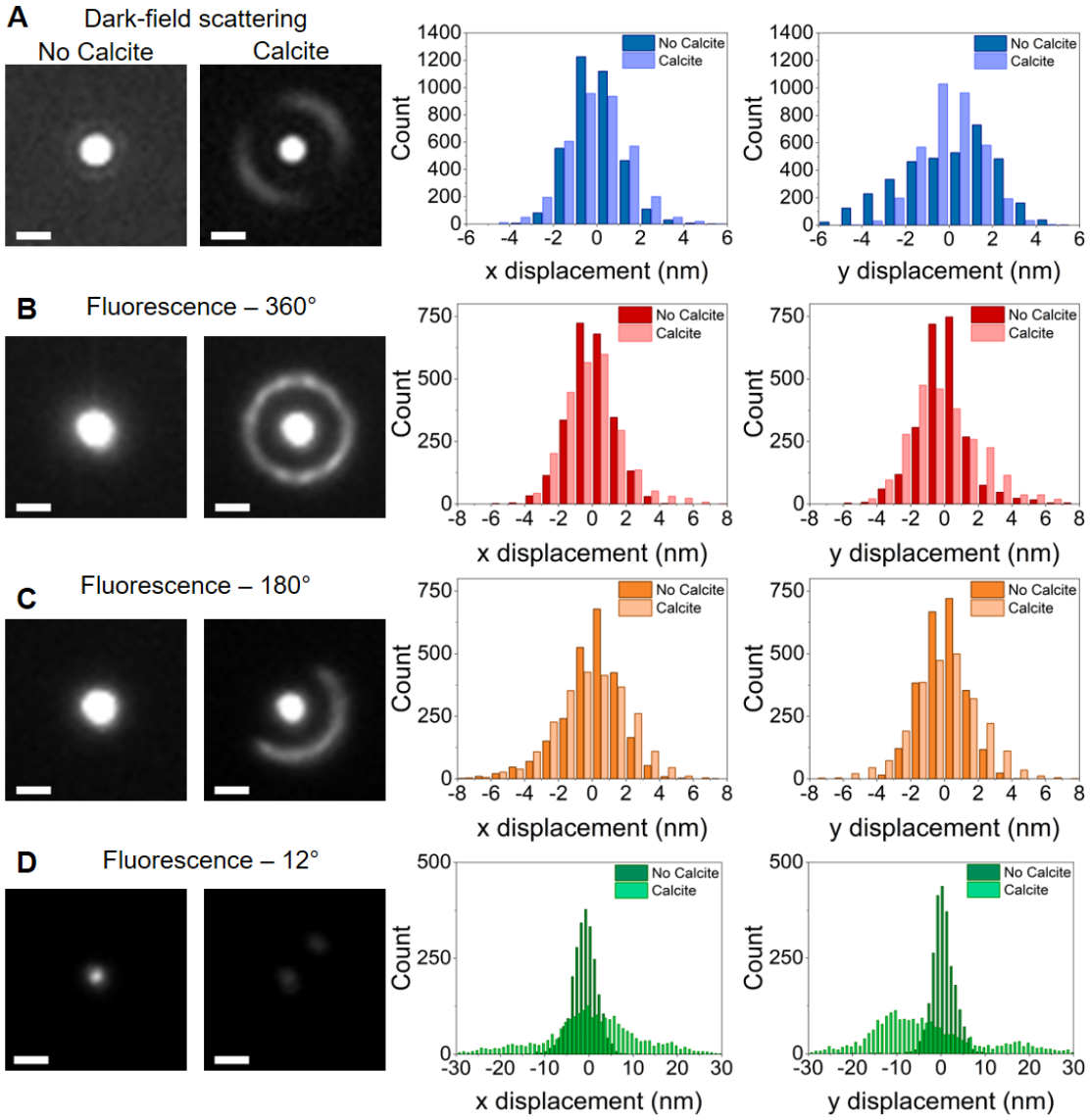

Figure 3.5. Localization precision with and without the calcite crystal. (A) Localization statistics for a mixture of six Au NPs in a dark-field scattering configuration obtained by fitting the diffraction-limited scattering to Equation 3.1. 0 nm is defined as the average center position for each particle sampled over 600 frames. Scale bars = 1 μm. (B-D) Representative fluorescence images of a fluorescent ND with $e_{\perp}$ arc lengths of (B) 360°, (C) 180°, and (D) 12°, controlled using an optical shutter. Images in B-D are shown at the same contrast. Localization statistics for four fluorescent nanodiamonds obtained by fitting the diffraction-limited emission to Equation 3.1. Scale bars = 1 μm.

Table 3.1. Comparing localization precision of CLocK microscopy in dark-field and fluorescent configurations.

Technique		Integrated Photon Counts	x – precision (nm)	y – precision (nm)
Dark-field	No Calcite	986,552	1.1 ± 0.1	2.1 ± 0.3
	Calcite	435,957	1.4 ± 0.2	1.3 ± 0.1
Fluorescence – 360°	No Calcite	445,909	1.3 ± 0.4	1.4 ± 0.8
	Calcite	257,450	1.6 ± 0.6	2.0 ± 0.6
Fluorescence – 180°	No Calcite	304,362	1.6 ± 0.8	1.2 ± 0.3
	Calcite	155,939	2.1 ± 0.4	2.0 ± 0.6
Fluorescence – 12°	No Calcite	45,797	10.9 ± 9.3	10.9 ± 10.7
	Calcite	26,496	10.6 ± 4.5	13.7 ± 4.1

3.3 Polarization and Orientation Information Revealed by CLocK Microscopy

To illustrate the power of the technique, Figure 3.6 compares traditional dark-field microscopy, dark-field CLocK microscopy, and scanning electron microscopy (SEM) for a mixture of Au NSs and NRs. While impossible to distinguish Au NSs from Au NRs in the dark-field microscopy image (Figure 3.6A), the unique PSFs produced in the CLocK image (Figure 3.6B) allow for the immediate differentiation of isotropic particles (Au NSs), which have a uniform $e_{\perp}$ pattern, and anisotropic particles (Au NRs), which have an angle-dependent $e_{\perp}$ pattern. Correlated SEM images confirm that the polarization and orientation information captured in the CLocK PSF reflects both the structure and orientation of the Au NPs accurately (Figure 3.6C). Thus, from a single CLocK image, we can rapidly and non-destructively assess information about metal nanoparticle structure and orientation.

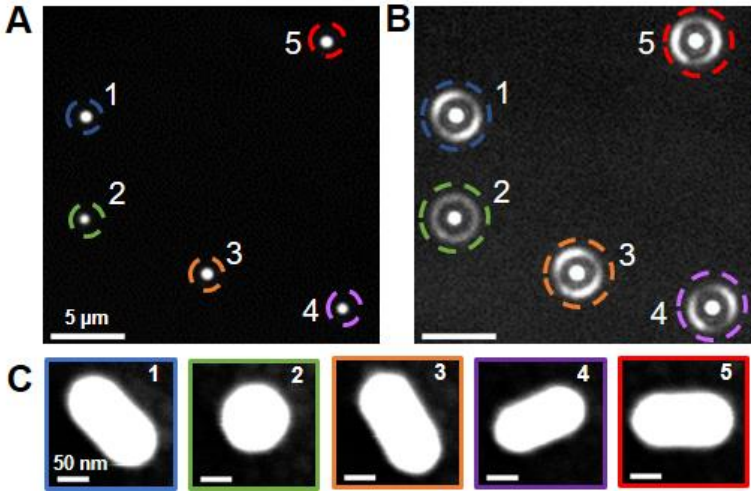

Figure 3.6. Comparison of (A) traditional dark-field, (B) dark-field CLocK, and (C) SEM images for a mixture of Au NSs and Au NRs. Optical images were acquired with an integration time of 300 ms. Scale bars: (A-B) 5 μm, (C) 50 nm.

To quantify the degree of anisotropy and orientation of a particle, we use Equation 3.2:

$$I_\theta \propto 1 + Mcos\{2(\theta - \varphi)\} \qquad \text{(Eq. 3.2)}$$

where I_θ is the background-subtracted intensity of the $e_\perp$ as a function of θ, M is the modulation depth, and φ is the orientation of the particle (Figure 3.7).[34,35] An isotropic scatterer is expected to have a M value of 0, whereas a perfect dipole will have a M value of 1. Fitting particles 2 and 5 from Figure 3.6B to Equation 3.2 yields M values of 0.07 and 0.5, respectively, consistent with their SEM identification as a NS and a NR.

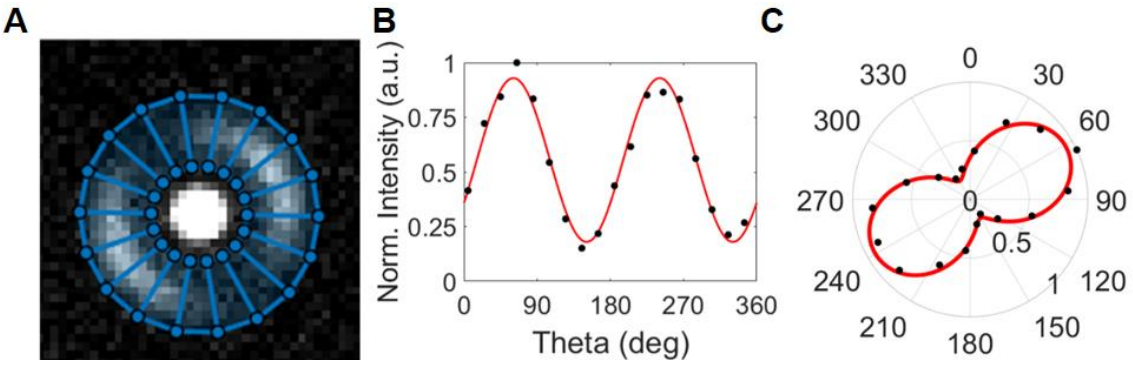

Figure 3.7. Example of a CLocK image of an Au NP being fit to Equation 3.2. (A) The $e_{\perp}$ of the CLocK image is segmented into 18 (20°) segments in which the intensity within each segment is integrated and normalized to give 18 unique data points. (B) Cartesian plot of Equation 3.2 fit (red) and normalized intensity (black) plotted as a function of θ. (C) Polar plot of Equation 3.2 fit (red) and normalized intensity (black) plotted as a function of θ.

Next, we demonstrate how CLocK allows us to track dynamic structural changes of nanoparticles in real time, by monitoring the chemidissolution of Au NRs in the presence of KI/I_2. Previous work has shown that Au NRs preferentially dissolve from their ends, resulting in the formation of spherical particles.[36,37] Figure 3.8A shows representative CLocK images of an Au NR (~120 nm long) before and after chemidissolution via KI/I_2 with a visual difference observed between the original anisotropic and the final isotropic CLocK images. Fitting the data to Equation 3.2, we observe a smooth decrease in *M* from 0.68 to 0.12 (Figure 3.8B), supporting the previous literature observations that the Au NR becomes more spherical as the dissolution proceeds. The change in *M* is also accompanied by a drop in the integrated scattering intensity of the $o_{\parallel}$ (Figure 3.8C), allowing us to monitor the kinetics of the chemidissolution process and indicating that the particle decreases in size during the dissolution process, consistent with previous reports.[23,38,39] Interestingly, by fitting the $o_{\parallel}$ to a 2-D Gaussian and extracting the peak position, we observe a directional change in the center-of-mass over time (Figure 3.8D). If the NR was dissolving from each end at equal rates, we would expect the center-of-mass to remain

unchanged during chemidissolution, even as the particle changed from rod-like to sphere-like (Figure 3.9A). However, not only do we observe the center-of-mass shift over time, but it also follows the orientation of the long axis of the Au NR, indicating that one end is etching faster than the other (Figure 3.9B). This mechanistic insight is hidden in traditional diffraction-limited images, yet is easily revealed through the multi-parameter analysis afforded by CLocK.

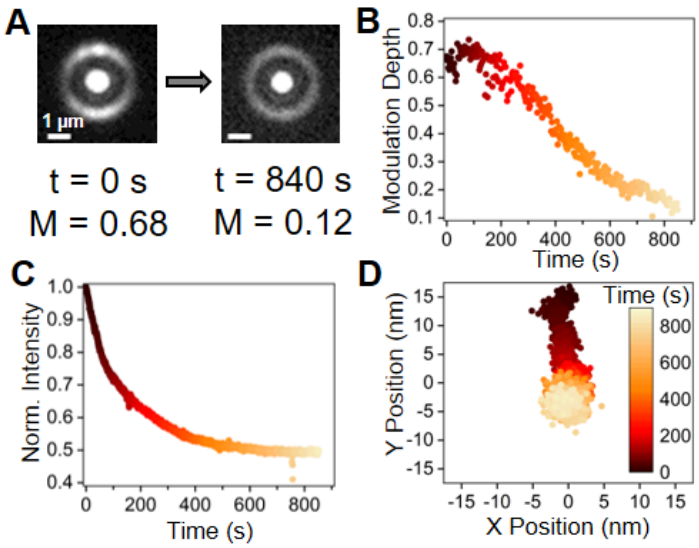

Figure 3.8. (A) Representative CLocK images of an Au NR before (t = 0 s) and after (t = 840 s) chemidissolution with KI/I_2, showing that the Au NR transitions from an anisotropic rod-like structure to a more isotropic sphere-like structure after dissolution (i.e. M = 0.68 → 0.12). (B-D) Changes in the (B) modulation depth, (C) scattering intensity, and (D) localized center-of-mass of the Au NR during chemidissolution. Scale bars = 1 μm.

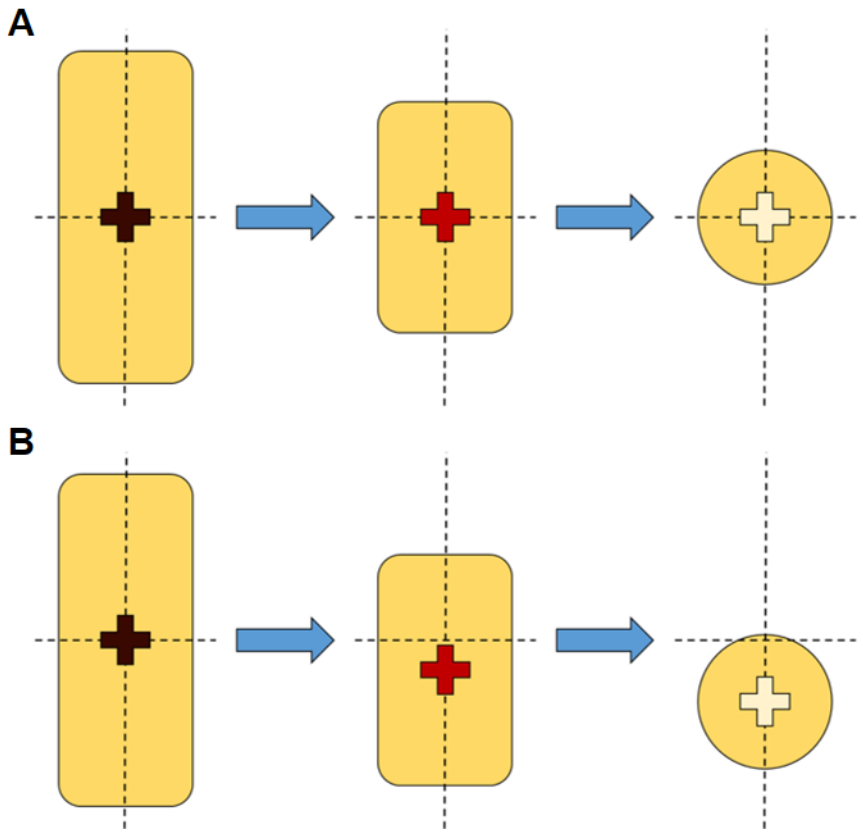

Figure 3.9. Schematic of asymmetric Au NR chemidissolution to a more symmetric Au NS. The dotted cross-hairs represent the same position in space. The '+' symbol represents the center of the Au NP at various time points, color coordinated to match Figure 3.8B-D. In (A), the rods dissolve at equal rates from the ends, leading to a stationary centroid, whereas in (B) the upper end of the rod dissolves faster than the lower end, resulting in a vertical displacement of the centroid with time.

3.4 Spectral Information Revealed by CLocK Microscopy

Further information can be obtained from CLocK by collecting color images. To illustrate this, CLocK images of Au NPs were captured using a color camera (Figures 3.10 A& 3.11A). In Figure 3.10A, the $e_{\perp}$ pattern for a representative NS appears green at all θ due to the symmetry of the dipolar plasmon. Conversely, the $e_{\perp}$ pattern for two representative Au NRs show two different color contributions: red/orange light corresponding to the longitudinal plasmon mode and green light corresponding to the

transverse plasmon mode.[29,40–43] For comparison, we note that the polarization-averaged diffraction-limited $o_{\parallel}$ images of both NR-1 and NR-2 contain less visual spectral information, given that the scattered light is dominated by the red longitudinal plasmon mode of the nanoparticle. Thus, the color CLocK image captures structure-dependent spectral properties that are masked in a traditional-diffraction limited spot.

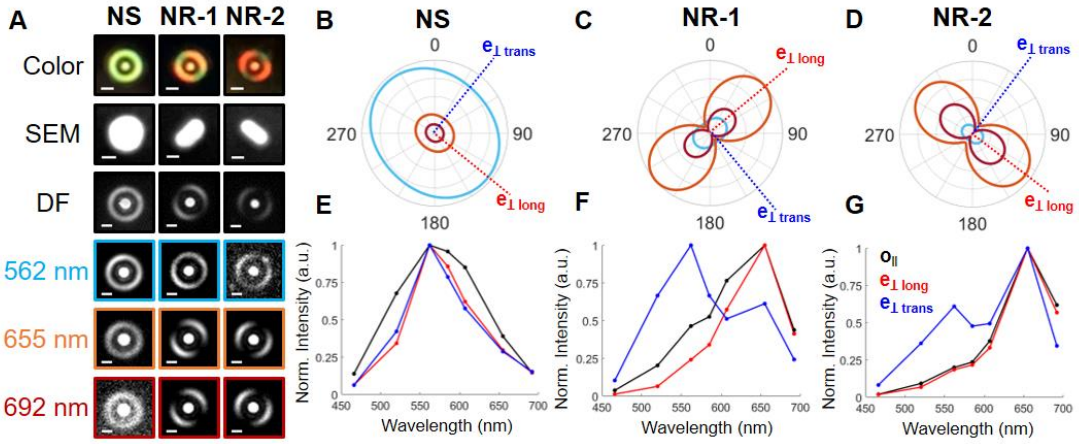

Figure 3.10. Comparison of spectral features found in CLocK images of a Au NS, large-width Au NR (NR-1, 126 x 61 nm), and small-width Au NR (NR-2, 113 x 51 nm). (A) From top to bottom: dark-field color CLocK images, SEM images, wavelength-averaged dark field (DF) CLocK images and spectrally-dependent dark field CLocK using bandpass filters centered at the wavelengths indicated. Images are shown at an optimal contrast to highlight the $e_{\perp}$ pattern. Scale bars: Color = 2 μm; SEM = 50 nm; DF = 1 μm. Optical images were acquired with an integration time of 300 ms. Bandpass filters: 562 ± 20 nm, 655 ± 20 nm, and 692 ± 20 nm. (B-D) Polar plots showing how the angle-dependent $e_{\perp}$ intensity changes as a function of bandpass filter wavelength. The data are normalized to the maximum scattering intensity and fit to Equation 3.2. Each trace in the polar plot is color coordinated to the bandpass filter labels in A. Each circle-tick of the polar plots is 0.25 normalized intensity units. (E-G) Normalized scattering intensity spectra of the intensity of $o_{\parallel}$ (black), $e_{\perp\,\mathrm{long}}$ (red), and $e_{\perp\,\mathrm{trans}}$ (blue) as a function of bandpass filter center wavelength. Data points are shown at the center wavelength of each filter and lines are drawn to guide the eye. Results from (B-D) and (E-G) agree well with polarization-resolved single-NP dark-field spectroscopy data (Figure 3.13).

In addition to capturing color images, spectral information can be obtained by introducing wavelength-resolved imaging to CLocK microscopy. Bandpass filters were used to monitor the spectral evolution of the CLocK images from 466 to 692 nm. For

discussion purposes, Figure 3.10A shows CLocK images of the Au NPs with three representative bandpass filters 562 nm, 655 nm, and 692 nm, while the complete range of wavelengths are shown in Figure 3.11A. Next polar plots were constructed by fitting the normalized $e_{\perp}$ intensity vs. θ to Equation 3.2 for images acquired at each wavelength, allowing us to visualize the spectrally-dependent evolution in anisotropy (Figures 3.10B-D, 3.11B, 3.12). For example, analyzing the wavelength-dependent polar plots for a representative Au NS shows the scattered light is quasi-isotropic (*M* values below 0.2) over the entire wavelength range probed (Figures 3.10B and 3.12). In contrast, the polar plots for NR-1 and NR-2 show the scattered light becomes increasingly anisotropic with increasing wavelength, going from $M < 0.25$ to $M > 0.75$ (Figures 3.10C-D, and 3.12).

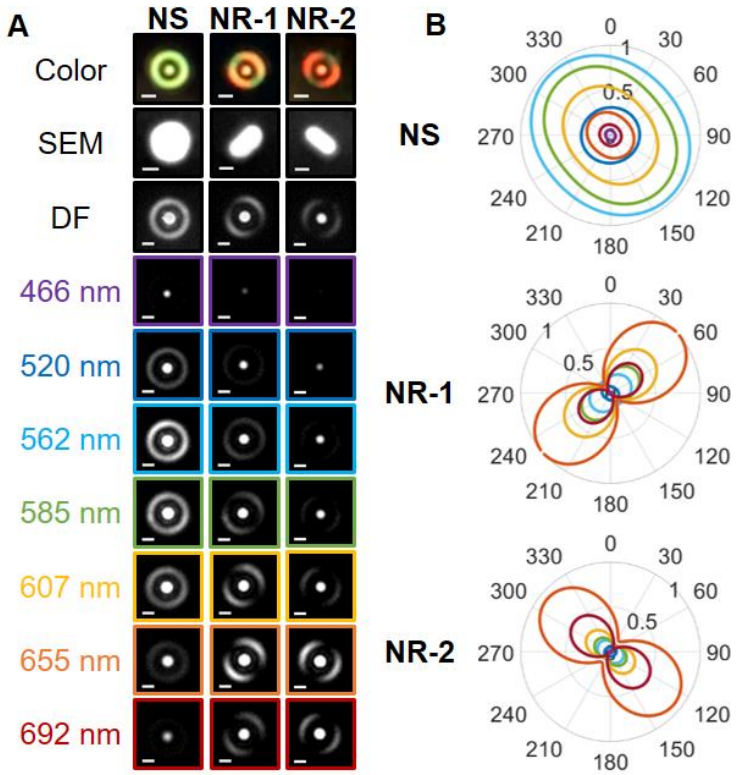

Figure 3.11. (A) Dark-field CLocK images from Figure 3.10 with complete range of bandpass filters. Scale bars: SEM = 50 nm; Color = 2 μm; DF = 1 μm. (B) Normalized intensity polar plots showing how the intensity and modulation depth of the $e_{\perp}$ changes as a function of bandpass filter wavelength. Polar plots are color coordinated to bandpass filter labels and CLocK images in A.

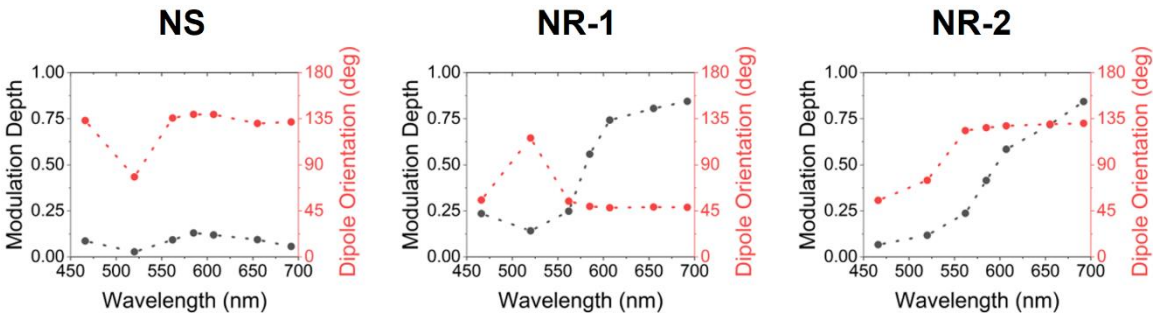

Figure 3.12. Modulation depth and orientation obtained from CLocK images plotted as a function of bandpass filter wavelength for the Au NS, Au NR-1, and Au NR-2 discussed in Figures 3.10 & 3.11.

Polarization-dependent spectra can also be extracted by means of spectrally-resolved imaging. Figure 3.10E-G, shows the wavelength-dependent scattering intensity of the polarization-averaged $o_{\parallel}$ (black data) as well as the intensity of the polarization-resolved light scattered along either the longitudinal axis ($e_{\perp\,long}$, red) or the transverse axis ($e_{\perp\,trans}$, blue), as determined from the polar plots in Figures 3.10B-D. As expected, the Au NS spectra all have a single peak around 562 nm, indicating a single dipolar plasmon resonance (Figure 3.10E). On the other hand, the Au NRs show variations among the three spectra (Figure 3.10F-G). The spectra along $e_{\perp\,long}$ (red data) are dominated by a single red peak, which corresponds to the longitudinal dipole mode, as expected. The spectra along $e_{\perp\,trans}$ (blue data) show two peaks: a peak in the blue-green region of the spectrum, which corresponds to the transverse plasmon mode, as well as a second red peak that aligns with the spectrum of the longitudinal mode. This agrees well with what has been previously shown in the literature, where the intensity of the transverse peak increases as a function of the NR diameter and the longitudinal peak intensity is suppressed along the transverse axis, but never completely disappears.[44] For comparison, Figure 3.13 shows polarization-resolved spectra taken using a grating spectrometer with a linear polarizer placed in front of it, and the same trends are observed, indicating that using the calcite-

crystal as a polarization analyzer does not introduce any artifacts in our spectra. We note that the polarization-averaged $o_{\parallel}$ spectra (black data) are dominated by the red scattering from the longitudinal mode, hiding these polarization-dependent trends, further emphasizing the advantages of CLocK images over traditional diffraction-limited PSFs.

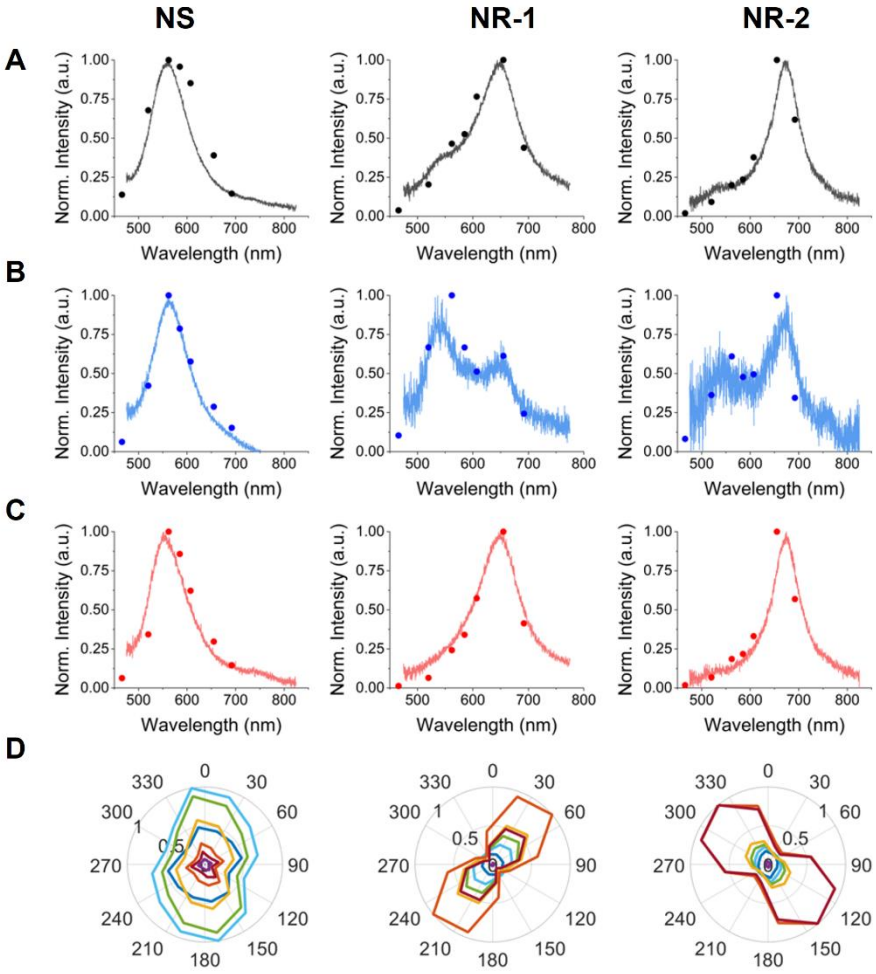

Figure 3.13. Comparison of spectral data obtained using CLocK images (data points) and single-particle polarization-resolved dark-field scattering spectroscopy for the Au NS, Au NR-1, and Au NR-2 discussed in Figures 3.10, 3.11, 3.12. (A) CLocK $o_{\parallel}$ intensity as a function of bandpass filter wavelength compared with the single-particle unpolarized dark-field scattering spectra of each Au NP. (B) CLocK $e_{\perp\ trans}$ intensity as a function of bandpass filter wavelength compared to single-particle polarized-resolved dark-field scattering spectra corresponding to $\theta = \varphi + 90°$ for each Au NP. (C) Comparison of CLocK $e_{\perp\ long}$ intensity as a function of bandpass filter wavelength to the single-particle polarized dark-field scattering spectra corresponding to $\theta = \varphi$ of each Au NP. (D) Intensity polar plots obtained from single-particle polarization-resolved dark-field scattering spectroscopy. Plots are color coordinated to the bandpass filter labels, CLocK images, and polar plot in Figure 3.11.

3.5 Temporal Information Revealed by CLocK Microscopy

So far, we have only described the ability of CLocK to add polarization/anisotropy information to images (whether black and white or spectrally-filtered). However, CLocK images also encode temporal information below the integration time of the camera (τ) based on the $e_\perp$ arc length, addressing a growing interest in the field to capture short-lived events.[45,46] Figure 3.14 compares simulated CLocK images for isotropic emitters with varying on times (t_{on}) relative to the integration time of the camera (τ). For an event lasting the full integration time of the camera ($t_{on} = \tau$), the $e_\perp$ sweeps out a complete ring (Figure 3.14-i). However, for events that are shorter than the integration time ($t_{on} < \tau$), the $e_\perp$ appears as an arc, where the length of the arc becomes shorter as the time of event decreases (Figures 3.14-ii-iii). For sufficiently short on times (Figure 3.14-iv), the arc becomes a diffraction-limited spot, which ultimately defines the temporal resolution of the technique.

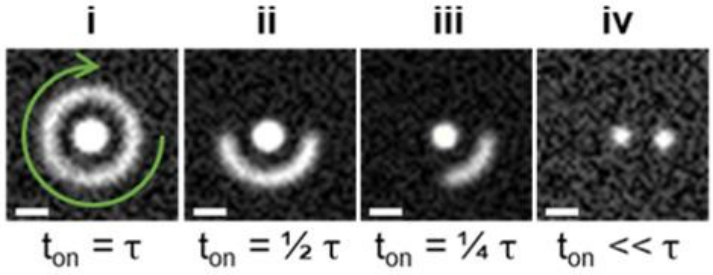

Figure 3.14. Kinetic information encoded in the $e_\perp$ arc length of CLocK images. Simulated CLocK images showing kinetic events (t_{on}) lasting (i) τ, arc length = 360°, (ii) ½ τ, arc length = 180°, (iii) ¼ τ, arc length = 90° and (iv) << τ, where τ is the time required to acquire an image and the arc length is expressed in polar coordinates. Scale bars = 1 μm.

To probe the temporal resolution in more detail, we trained a convolutional neural network (CNN) to extract the $e_\perp$ arc length from simulated CLocK images on (pseudo)isotropic emitters with M values between 0 – 0.2, where parameters such as absolute intensity, intensity-to-background ratio, $o_\parallel$ and $e_\perp$ Gaussian width, $o_\parallel$ center

position, and $o_{\parallel}$ – $e_{\perp}$ distance, and orientation angle were allowed to randomly vary, while the parameter of interest (e.g. $e_{\perp}$ arc length) was systematically varied (Figure 3.15, see Chapter 2 for more details). The model uses polar coordinates to report temporal resolution, where an event with $t_{on} = \tau$ would be 360°, an event with $t_{on} = 0.25\tau$ would be 90°, etc. From these simulated data, we obtain a theoretical temporal resolution of 5.5°, corresponding to a minimum resolvable $t_{on} = \frac{\tau}{65}$.

To test this model on experimental data, we used a mechanical shutter to control the effective on-time of fluorescent events from single nanodiamonds (NDs). For fluorescent NDs with anisotropy values between $M = 0.0 – 0.2$ and signal-to-noise ratios between 6.3 to 8.6, the trained CNN was able to extract $e_{\perp}$ arc lengths ranging from 5° - 360° with a root mean square error (RMSE) of 15° (Figure 3.15), or $t_{on} = \frac{\tau}{24}$ (corresponding to 6.7 ms temporal resolution with an integration time of 160 ms).

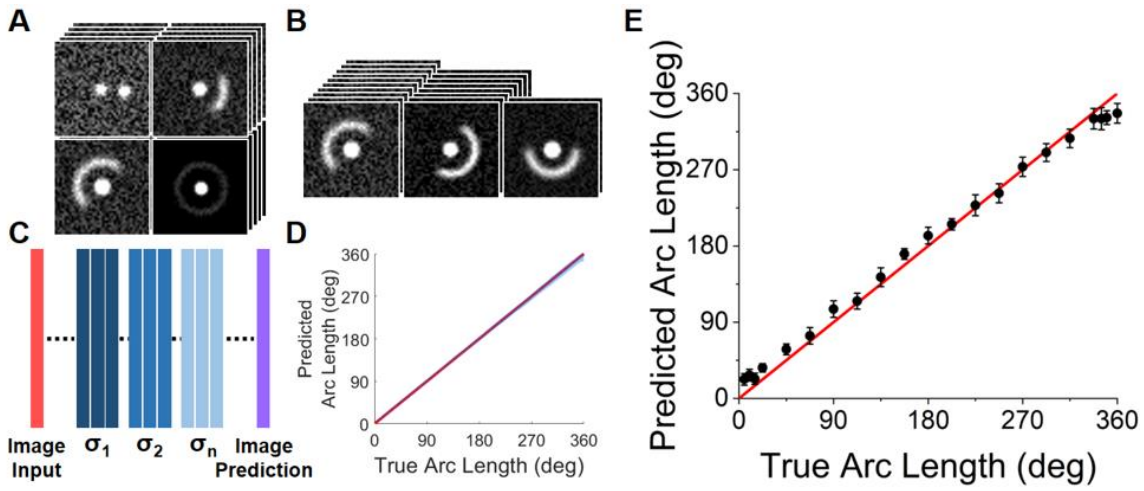

Figure 3.15. Combining CLocK microscopy and CNNs to extract kinetic information from CLocK images of isotropic emitters. (A) CLocK images are simulated, where all parameters such as $e_\perp$ arc length, $e_\perp$ modulation depth, etc. are known. To extract temporal information from CLocK images, images with 1 - 360° $e_\perp$ arc lengths are simulated in 1° increments. (B) After background subtraction and normalization, the simulated images are broken up into three data sets, a training data set, a validation data set, and a test data set. (C) Training and validation data sets are used to train the CNN. (D) The test data set is used to test the accuracy of the CNN on simulated data. For kinetic data, the CNN was able to predict $e_\perp$ arc length with an RMSE of 5.5° on simulated CLocK images. (E) Once satisfied with the model's ability to predict simulated data, the model can be applied to experimental CLocK data to be evaluated. The CNN's model was able to predict the $e_\perp$ arc length of experimental CLocK images with an RMSE of 15°.

While the studies on fluorescent nanodiamonds allowed us to benchmark the temporal resolution of CLocK for isotropic emitters, we next explored single-molecule surface enhanced Raman scattering (SM-SERS) as a system where both fast temporal processes and polarized emission are present.[25,26,46–48] Moreover, unlike the previous data, where individual emitters/scatterers were well-spaced on the surface to avoid overlapping signals, the temporal fluctuations in SERS signals allows us to uniquely resolve the spatial origin of both the SERS signal and the underlying silver nanoparticle luminescence, which are both convolved in a single diffraction-limited spot.[14,15,49] Figure 3.16A shows several representative CLocK images of Rhodamine 6G (R6G) SM-SERS events on aggregated

Ag colloid, where τ = 1s (additional events shown in Figure 3.17). In Figure 3.16B, normalized intensity time-traces using the $o_{\parallel}$ (black) and the $e_{\perp}$ (red) are compared, revealing the added temporal resolution offered by analyzing the $e_{\perp}$. This temporal enhancement becomes even more apparent in the magnified sub-section of the time trace in Figure 3.16C: what appears as a single SM-SERS event lasting a few seconds in the $o_{\parallel}$ data can be resolved as several separate and temporally distinct SM-SERS events using the $e_{\perp}$ data. However, due to the convolution of polarization and temporal information present in these short-lived SM-SERS events, we are currently unable to accurately quantify the temporal resolution observed. That said, based on our simulations above, we predict that our temporal resolution is no better than $\frac{\tau}{65}$ or 15 ms for the one second integration times used in collecting these data. Although this temporal resolution can be experimentally improved by using shorter camera integration times, current limitations on the rotation speed of the motor do not allow us to access faster intensity fluctuations, as have been reported by others.[46]

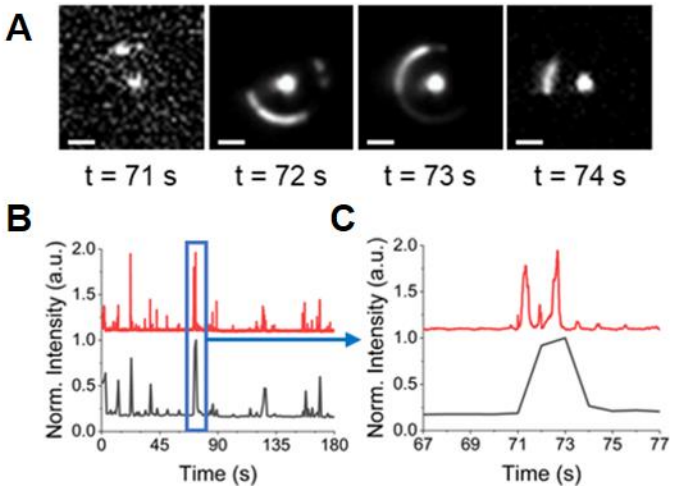

Figure 3.16. (A) Representative CLocK images for Rhodamine 6G SM-SERS events. Scale bars = 1 μm, optical images acquired with an integration time of 1 s. (B) Normalized intensity time-traces of the $o_{\parallel}$ (black) and $e_{\perp}$ (red) for SM-SERS events on aggregated Ag colloid. (C) A subsection of the intensity time-traces from (C) is magnified to demonstrate the difference in temporal resolution provided by the $o_{\parallel}$ and $e_{\perp}$. The portion of the time trace shown in (C) corresponds to the images shown in (A).

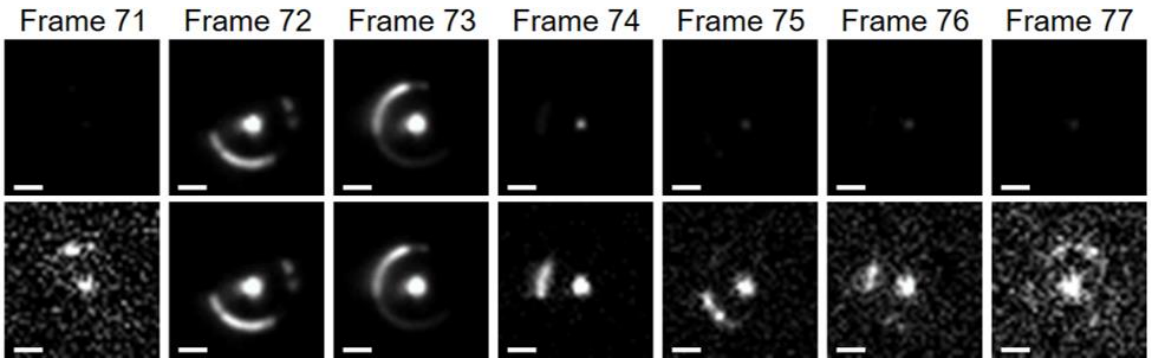

Figure 3.17. CLocK images of R6G SM-SERS events on Ag colloids shown in the intensity time-trace in Figure 3.16B. The images in the top row are contrasted the same to show the difference in intensity of several SM-SERS events. The images in the bottom row are contrasted to best show the CLocK PSF and kinetic information encoded in the $e_{\perp}$. Frame 71 corresponds to t = 70 – 71 s in the intensity time trace of Figure 3.16. Scale bars = 1 μm.

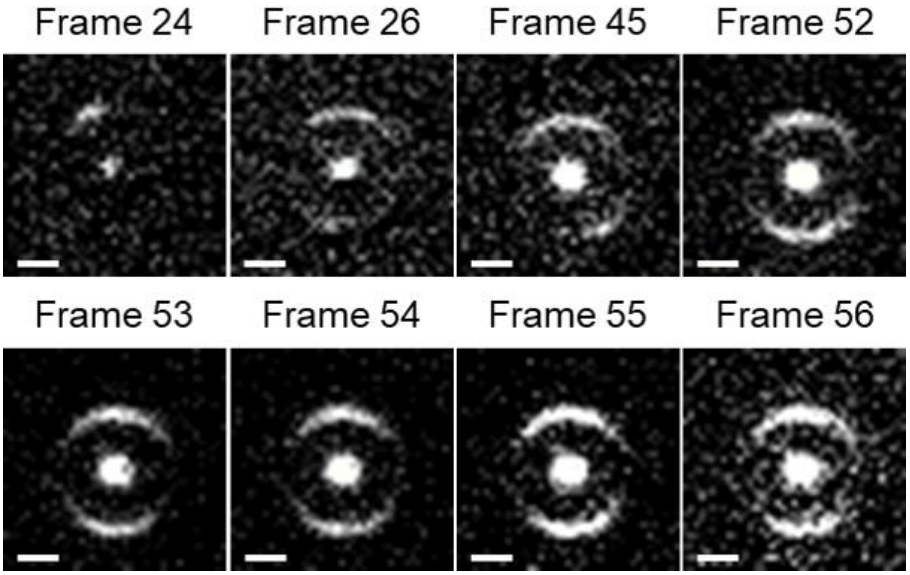

Figure 3.18. CLocK images of R6G SM-SERS on an Ag dimer. The images are individually contrasted to best show the CLocK PSF. Scale bars = 1 μm. Note that even for the short events in frames 24, 26, and 45, the pattern is consistent with the dipole emission observed in the other frames.

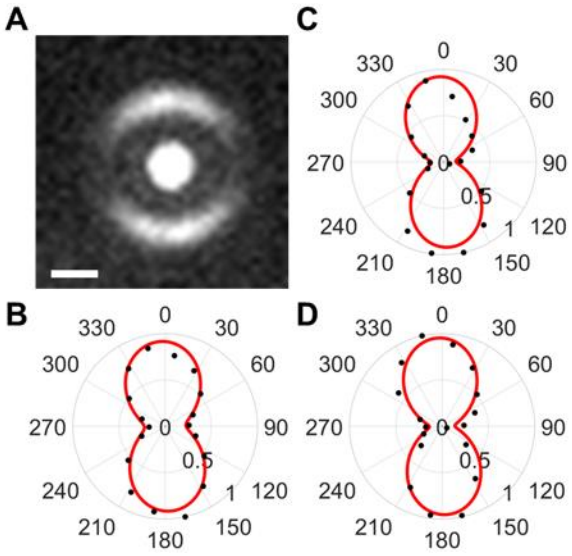

Figure 3.19. SM-SERS polarization information available using CLocK microscopy on an Ag dimer. (A) Dark-field CLocK image of an Ag dimer. Scale bar = 1 μm. (B) $e_{\perp}$ dark-field intensity polar plot fit of the Ag dimer in A. (C) $e_{\perp}$ intensity polar plot fit of the R6G SM-SERS event in Frame 52 (Figure 3.18). (D) $e_{\perp}$ intensity polar plot fit of the R6G SM-SERS event in Frame 56 (Figure 3.18).

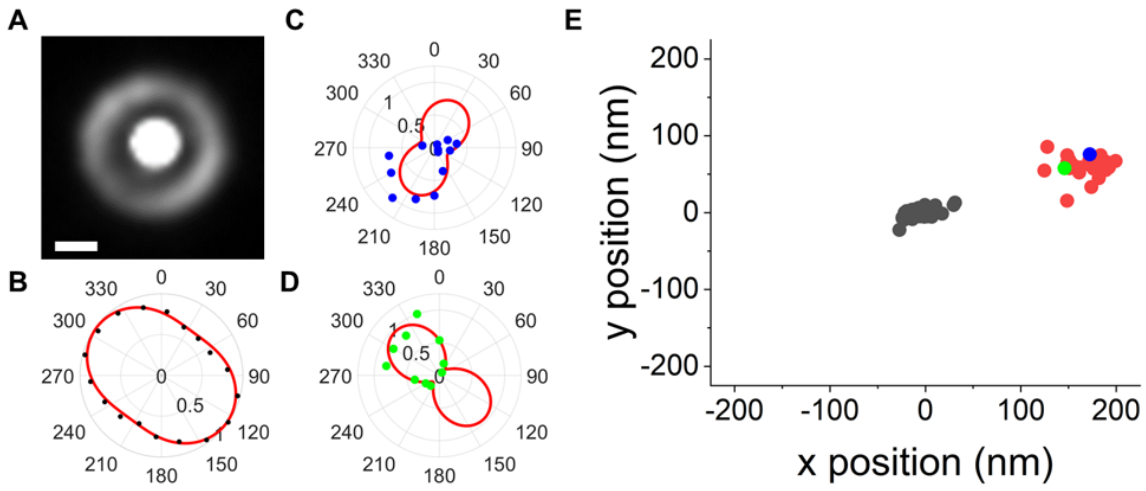

Figure 3.20. Polarization and localization SM-SERS information available using CLocK microscopy. (A) Dark-field CLocK image of an aggregated Ag colloid. Scale bar = 1 µm. (B) $e_{\perp}$ dark field intensity polar plot fit of the Ag colloid in A. (C) $e_{\perp}$ intensity polar plot fit of the R6G SM-SERS event in Frame 72 (Figure 3.16). (D) $e_{\perp}$ intensity polar plot fit of the R6G SM-SERS event in Frame 73 (Figure 3.16). (E) Super-localization data of the Ag colloid center (black) and R6G SM-SERS events (red, Frame 72 – blue, Frame 73 – green). Only events in which the $o_{\parallel}$ had a $R^2 > 0.80$ when fit to a 2-D Gaussian are plotted.

One challenge that requires more exploration is how to extract polarization/orientation information from the short-lived events ($t_{on} < \tau$) revealed by CLocK (as in Figure 3.16A). To highlight this, Figures 3.17-3.20 shows SM-SERS CLocK data on both a silver nanoparticle dimer and a larger multi-particle aggregate, as determined by CLocK. For the structure assigned as a dimer, we observe anisotropic dark field scattering ($M = 0.58$, $\varphi = 87°$), similar to the gold nanorods discussed above. Based on previous literature, we expect SM-SERS from a dimer to be polarized along the long axis,[50] and this behavior is observed for all SM-SERS events, even those shorter than τ (Figures 3.18-3.19). Not only does the polarization of the SM-SERS further support our dimer assignment, but also highlights that for relatively simple structures, it is straightforward to interpret the polarization response.

On the other hand, our CLocK analysis suggests that the SM-SERS data shown in Figure 3.16A originates from a higher order nanoparticle aggregate (e.g. trimer or above). We make this assignment because (1) its dark field CLocK appears quasi-isotropic (unlike a dimer) and (2) the spatial origin of the aggregate luminescence is offset by >100 nm from the SERS hot spot (as we have previously observed in large aggregates, Figure 3.20).[15,51,52] From previous work, it is known that higher order aggregates can modify the output polarization of SM-SERS based on how the molecule couples to different plasmon modes within the aggregate.[48,50,53] Angle-dependent intensity analysis of images at t = 72 and 73 s from Figure 3.16A indicate that the two events appear to have different polarization responses, although neither have high quality fits to Equation 1 ($R^2 < 0.7$, Figure 3.20C-D). Interestingly, when we localized the SERS emission of these two frames by fitting the associated $o_{\parallel}$ to a two-dimensional Gaussian, we found that the emission was spatially separated by 32 nm, which is larger than the expected precision of our SERS measurement (< 3 nm based on comparable signal; see Figure 3.5C Table 3.1), suggesting that the molecule is exploring spatially distinct regions of the nanoparticle aggregate (Figure 3.20E).[14,49,51,52] We speculate that the R6G moved to a new location on the aggregate surface (as evidenced by the shift in its localized position), leading to a change in the polarization output of the SERS due to changes in how the molecular dipole couples to the plasmon modes of the aggregate. However, we note that in this regime, we cannot be completely quantitative about the polarization/orientation of the emission without having either events with $t_{on} > \tau$ and/or correlated nanoparticle structure information; this will be the subject of future work. Despite this challenge, these results highlight the wealth of information encoded in CLocK images that is unavailable in traditional diffraction-limited

imaging and yet crucial for understanding these time-varying molecule-plasmon interactions.

3.6 Conclusions

In conclusion, we have introduced CLocK microscopy, a multi-parameter super-resolution imaging technique that allows the position, intensity, extent of anisotropy, and orientation of a single emitter/scatterer to be measured from a single image, while also offering fast temporal resolution for monitoring dynamic processes. We have demonstrated that CLocK allows for rapid structural discrimination in nanoparticle samples, and when combined with color or spectrally-resolved imaging, paints an even clearer picture of differences in nanoparticle properties. Future work will focus on using color RGB images to extract spectral information and provide an even more complete particle-level analysis within a single dark field image.[18,41,54–60] To demonstrate the utility of CLocK, we showed two representative applications, nanorod chemidissolution and SM-SERS, where new mechanistic insight is revealed by the contemporaneous analyses of polarization and localization. Future work will focus on these two applications in more detail, as well as expanding our use of machine learning methods to train and analyze CLocK images. We believe CLocK will prove useful across a wide range of applications, given that the technique is conceptually simple, relatively inexpensive to implement, works with existing super-localization codes, and is compatible with multiple forms of optical spectroscopy (including dark field, fluorescence, and Raman, as shown here), making it a universally useful imaging strategy for multi-parameter super-resolution imaging.

3.7 Acknowledgements

This work was supported by the U.S. National Science Foundation under grant number DMR-2003613. This research includes calculations carried out on HPC resources supported in part by the National Science Foundation through major research instrumentation grant number 1625061 and by the US Army Research Laboratory under contract number W911NF-16-2-0189. The authors would like to thank Natalia Y. Molina and Philip A. Reinhardt for their valuable discussions and suggestions throughout the experimental process.

3.8 References

(1) Dean, K. M.; Palmer, A. E. Advances in Fluorescence Labeling Strategies for Dynamic Cellular Imaging. *Nat. Chem. Biol.* **2014**, *10* (7), 512–523.

(2) Sengupta, P.; van Engelenburg, S. B.; Lippincott-Schwartz, J. Superresolution Imaging of Biological Systems Using Photoactivated Localization Microscopy. *Chem. Rev.* **2014**, *114* (6), 3189–3202.

(3) Rust, M. J.; Bates, M.; Zhuang, X. Sub-Diffraction-Limit Imaging by Stochastic Optical Reconstruction Microscopy (STORM). *Nat. Methods* **2006**, *3* (10), 793–796.

(4) van de Linde, S.; Löschberger, A.; Klein, T.; Heidbreder, M.; Wolter, S.; Heilemann, M.; Sauer, M. Direct Stochastic Optical Reconstruction Microscopy with Standard Fluorescent Probes. *Nat. Protoc.* **2011**, *6* (7), 991–1009.

(5) Biteen, J.; Willets, K. A. Introduction: Super-Resolution and Single-Molecule Imaging. *Chem. Rev.* **2017**, *117* (11), 7241–7243.

(6) Betzig, E.; Patterson, G. H.; Sougrat, R.; Lindwasser, O. W.; Olenych, S.; Bonifacino, J. S.; Davidson, M. W.; Lippincott-Schwartz, J.; Hess, H. F. Imaging Intracellular Fluorescent Proteins at Nanometer Resolution. *Science* **2006**, *313* (5793), 1642–1645.

(7) Hauser, M.; Wojcik, M.; Kim, D.; Mahmoudi, M.; Li, W.; Xu, K. Correlative Super-Resolution Microscopy: New Dimensions and New Opportunities. *Chem. Rev.* **2017**, *117* (11), 7428–7456.

(8) Lee, A.; Tsekouras, K.; Calderon, C.; Bustamante, C.; Pressé, S. Unraveling the Thousand Word Picture: An Introduction to Super-Resolution Data Analysis. *Chem. Rev.* **2017**, *117* (11), 7276–7330.

(9) Shen, H.; Tauzin, L. J.; Baiyasi, R.; Wang, W.; Moringo, N.; Shuang, B.; Landes, C. F. Single Particle Tracking: From Theory to Biophysical Applications. *Chem. Rev.* **2017**, *117* (11), 7331–7376.

(10) Möckl, L.; Moerner, W. E. Super-Resolution Microscopy with Single Molecules in Biology and Beyond–Essentials, Current Trends, and Future Challenges. *J. Am. Chem. Soc.* **2020**, *142* (42), 17828–17844.

(11) Dhiman, S.; Andrian, T.; Gonzalez, B. S.; Tholen, M. M. E.; Wang, Y.; Albertazzi, L. Can Super-Resolution Microscopy Become a Standard Characterization Technique for Materials Chemistry? *Chem. Sci.* **2022**, *13* (8), 2152–2166.

(12) Willets, K. A. Super-Resolution Imaging of SERS Hot Spots. *Chem Soc Rev* **2014**, *43* (11), 3854–3864.

(13) Wöll, D.; Flors, C. Super-Resolution Fluorescence Imaging for Materials Science. *Small Methods* **2017**, *1* (10), 1700191.

(14) Stranahan, S. M.; Willets, K. A. Super-Resolution Optical Imaging of Single-Molecule SERS Hot Spots. *Nano Lett.* **2010**, *10* (9), 3777–3784.

(15) Weber, M. L.; Litz, J. P.; Masiello, D. J.; Willets, K. A. Super-Resolution Imaging Reveals a Difference between SERS and Luminescence Centroids. *ACS Nano* **2012**, *6* (2), 1839–1848.

(16) Weber, M. L.; Willets, K. A. Nanoscale Studies of Plasmonic Hot Spots Using Super-Resolution Optical Imaging. *MRS Bull.* **2012**, *37* (8), 745–751.

(17) Willets, K. A. Super-Resolution Imaging of Interactions between Molecules and Plasmonic Nanostructures. *Phys. Chem. Chem. Phys.* **2013**, *15* (15), 5345–5354.

(18) Xiao, L.; Ha, J. W.; Wei, L.; Wang, G.; Fang, N. Determining the Full Three-Dimensional Orientation of Single Anisotropic Nanoparticles by Differential Interference Contrast Microscopy. *Angew. Chem. Int. Ed.* **2012**, *51* (31), 7734–7738.

(19) Peterman, E. J. G.; Sosa, H.; Goldstein, L. S. B.; Moerner, W. E. Polarized Fluorescence Microscopy of Individual and Many Kinesin Motors Bound to Axonemal Microtubules. *Biophys. J.* **2001**, *81* (5), 2851–2863.

(20) Gu, Y.; Won Ha, J.; E. Augspurger, A.; Chen, K.; Zhu, S.; Fang, N. Single Particle Orientation and Rotational Tracking (SPORT) in Biophysical Studies. *Nanoscale* **2013**, *5* (22), 10753–10764.

(21) Gu, Y.; Sun, W.; Wang, G.; Fang, N. Single Particle Orientation and Rotation Tracking Discloses Distinctive Rotational Dynamics of Drug Delivery Vectors on Live Cell Membranes. *J. Am. Chem. Soc.* **2011**, *133* (15), 5720–5723.

(22) Ding, T.; Lew, M. D. Single-Molecule Localization Microscopy of 3D Orientation and Anisotropic Wobble Using a Polarized Vortex Point Spread Function. *J. Phys. Chem. B* **2021**, *125* (46), 12718–12729.

(23) Sundaresan, V.; Monaghan, J. W.; Willets, K. A. Visualizing the Effect of Partial Oxide Formation on Single Silver Nanoparticle Electrodissolution. *J. Phys. Chem. C* **2018**, *122* (5), 3138–3145.

(24) Joshi, P. B.; Anthony, T. P.; Wilson, A. J.; Willets, K. A. Imaging Out-of-Plane Polarized Emission Patterns on Gap Mode SERS Substrates: From High Molecular Coverage to the Single Molecule Regime. *Faraday Discuss.* **2017**, *205*, 245–259.

(25) Stranahan, S. M.; Titus, E. J.; Willets, K. A. SERS Orientational Imaging of Silver Nanoparticle Dimers. *J. Phys. Chem. Lett.* **2011**, *2* (21), 2711–2715.

(26) Stranahan, S. M.; Titus, E. J.; Willets, K. A. Discriminating Nanoparticle Dimers from Higher Order Aggregates through Wavelength-Dependent SERS Orientational Imaging. *ACS Nano* **2012**, *6* (2), 1806–1813.

(27) Titus, E. J.; Willets, K. A. Accuracy of Superlocalization Imaging Using Gaussian and Dipole Emission Point-Spread Functions for Modeling Gold Nanorod Luminescence. *ACS Nano* **2013**, *7* (7), 6258–6267.

(28) Wu, T.; Lu, J.; Lew, M. D. Dipole-Spread-Function Engineering for Simultaneously Measuring the 3D Orientations and 3D Positions of Fluorescent Molecules. *Optica* **2022**, *9* (5), 505.

(29) Schubert, O.; Becker, J.; Carbone, L.; Khalavka, Y.; Provalska, T.; Zins, I.; Sönnichsen, C. Mapping the Polarization Pattern of Plasmon Modes Reveals Nanoparticle Symmetry. *Nano Lett.* **2008**, *8* (8), 2345–2350.

(30) Lampe, A.; Haucke, V.; Sigrist, S. J.; Heilemann, M.; Schmoranzer, J. Multi-Colour Direct STORM with Red Emitting Carbocyanines. *Biol. Cell* **2012**, *104* (4), 229–237.

(31) Bates, M.; Dempsey, G. T.; Chen, K. H.; Zhuang, X. Multicolor Super-Resolution Fluorescence Imaging via Multi-Parameter Fluorophore Detection. *ChemPhysChem* **2012**, *13* (1), 99–107.

(32) Jungmann, R.; Avendaño, M. S.; Woehrstein, J. B.; Dai, M.; Shih, W. M.; Yin, P. Multiplexed 3D Cellular Super-Resolution Imaging with DNA-PAINT and Exchange-PAINT. *Nat. Methods* **2014**, *11* (3), 313–318.

(33) Böning, D.; Wieser, F.-F.; Sandoghdar, V. Polarization-Encoded Colocalization Microscopy at Cryogenic Temperatures. *ACS Photonics* **2021**, *8* (1), 194–201.

(34) Adachi, T.; Brazard, J.; Ono, R. J.; Hanson, B.; Traub, M. C.; Wu, Z.-Q.; Li, Z.; Bolinger, J. C.; Ganesan, V.; Bielawski, C. W.; Vanden Bout, D. A.; Barbara, P. F. Regioregularity and Single Polythiophene Chain Conformation. *J. Phys. Chem. Lett.* **2011**, *2* (12), 1400–1404.

(35) Chang, W.-S.; Ha, J. W.; Slaughter, L. S.; Link, S. Plasmonic Nanorod Absorbers as Orientation Sensors. *Proc. Natl. Acad. Sci.* **2010**, *107* (7), 2781–2786.

(36) Sun, S.; Gao, M.; Lei, G.; Zou, H.; Ma, J.; Huang, C. Visually Monitoring the Etching Process of Gold Nanoparticles by KI/I2 at Single-Nanoparticle Level Using Scattered-Light Dark-Field Microscopic Imaging. *Nano Res.* **2016**, *9* (4), 1125–1134.

(37) Cheng, J.; Liu, Y.; Cheng, X.; He, Y.; Yeung, E. S. Real Time Observation of Chemical Reactions of Individual Metal Nanoparticles with High-Throughput Single Molecule Spectral Microscopy. *Anal. Chem.* **2010**, *82* (20), 8744–8749.

(38) Molina, N. Y.; Pungsrisai, T.; O'Dell, Z. J.; Paranzino, B.; Willets, K. A. The Hidden Role of the Supporting Electrode for Creating Heterogeneity in Single Entity Electrochemistry. *ChemElectroChem* **2022**, *9* (9).

(39) Sundaresan, V.; Monaghan, J. W.; Willets, K. A. Monitoring Simultaneous Electrochemical Reactions with Single Particle Imaging. *ChemElectroChem* **2018**, *5* (20), 3052–3058.

(40) Jain, P. K.; Lee, K. S.; El-Sayed, I. H.; El-Sayed, M. A. Calculated Absorption and Scattering Properties of Gold Nanoparticles of Different Size, Shape, and Composition: Applications in Biological Imaging and Biomedicine. *J. Phys. Chem. B* **2006**, *110* (14), 7238–7248.

(41) Huang, X.; El-Sayed, M. A. Gold Nanoparticles: Optical Properties and Implementations in Cancer Diagnosis and Photothermal Therapy. *J. Adv. Res.* **2010**, *1* (1), 13–28.

(42) Lohse, S. E.; Murphy, C. J. The Quest for Shape Control: A History of Gold Nanorod Synthesis. *Chem. Mater.* **2013**, *25* (8), 1250–1261.

(43) Halas, N. J.; Lal, S.; Chang, W.-S.; Link, S.; Nordlander, P. Plasmons in Strongly Coupled Metallic Nanostructures. *Chem. Rev.* **2011**, *111* (6), 3913–3961.

(44) Huang, Y.; Kim, D.-H. Dark-Field Microscopy Studies of Polarization-Dependent Plasmonic Resonance of Single Gold Nanorods: Rainbow Nanoparticles. *Nanoscale* **2011**, *3* (8), 3228.

(45) Wang, W.; Shen, H.; Shuang, B.; Hoener, B. S.; Tauzin, L. J.; Moringo, N. A.; Kelly, K. F.; Landes, C. F. Super Temporal-Resolved Microscopy (STReM). *J. Phys. Chem. Lett.* **2016**, *7* (22), 4524–4529.

(46) Lindquist, N. C.; de Albuquerque, C. D. L.; Sobral-Filho, R. G.; Paci, I.; Brolo, A. G. High-Speed Imaging of Surface-Enhanced Raman Scattering Fluctuations from Individual Nanoparticles. *Nat. Nanotechnol.* **2019**, *14* (10), 981–987.

(47) Shegai, T.; Brian, B.; Miljković, V. D.; Käll, M. Angular Distribution of Surface-Enhanced Raman Scattering from Individual Au Nanoparticle Aggregates. *ACS Nano* **2011**, *5* (3), 2036–2041.

(48) Shegai, T.; Li, Z.; Dadosh, T.; Zhang, Z.; Xu, H.; Haran, G. Managing Light Polarization via Plasmon–Molecule Interactions within an Asymmetric Metal Nanoparticle Trimer. *Proc. Natl. Acad. Sci.* **2008**, *105* (43), 16448–16453.

(49) Weber, M. L.; Willets, K. A. Correlated Super-Resolution Optical and Structural Studies of Surface-Enhanced Raman Scattering Hot Spots in Silver Colloid Aggregates. *J. Phys. Chem. Lett.* **2011**, *2* (14), 1766–1770.

(50) Li, Z.; Shegai, T.; Haran, G.; Xu, H. Multiple-Particle Nanoantennas for Enormous Enhancement and Polarization Control of Light Emission. *ACS Nano* **2009**, *3* (3),

(51) Titus, E. J.; Weber, M. L.; Stranahan, S. M.; Willets, K. A. Super-Resolution SERS Imaging beyond the Single-Molecule Limit: An Isotope-Edited Approach. *Nano Lett.* **2012**, *12* (10), 5103–5110.

(52) Weber, M. L.; Wilson, A. J.; Willets, K. A. Characterizing the Spatial Dependence of Redox Chemistry on Plasmonic Nanoparticle Electrodes Using Correlated Super-Resolution Surface-Enhanced Raman Scattering Imaging and Electron Microscopy. *J. Phys. Chem. C* **2015**, *119* (32), 18591–18601.

(53) Chuntonov, L.; Haran, G. Maximal Raman Optical Activity in Hybrid Single Molecule-Plasmonic Nanostructures with Multiple Dipolar Resonances. *Nano Lett.* **2013**, *13* (3), 1285–1290.

(54) Biswas, S.; Nepal, D.; Park, K.; Vaia, R. A. Orientation Sensing with Color Using Plasmonic Gold Nanorods and Assemblies. *J. Phys. Chem. Lett.* **2012**, *3* (18), 2568–2574.

(55) Hao, J.; Xiong, B.; Cheng, X.; He, Y.; Yeung, E. S. High-Throughput Sulfide Sensing with Colorimetric Analysis of Single Au–Ag Core–Shell Nanoparticles. *Anal. Chem.* **2014**, *86* (10), 4663–4667.

(56) Huang, Y.; Ferhan, A. R.; Kim, D.-H. Tunable Scattered Colors over a Wide Spectrum from a Single Nanoparticle. *Nanoscale* **2013**, *5* (17), 7772.

(57) Jing, C.; Gu, Z.; Ying, Y.-L.; Li, D.-W.; Zhang, L.; Long, Y.-T. Chrominance to Dimension: A Real-Time Method for Measuring the Size of Single Gold Nanoparticles. *Anal. Chem.* **2012**, *84* (10), 4284–4291.

(58) Pan, Z. Y.; Zhou, J.; Zou, H. Y.; Li, Y. F.; Gao, P. F.; Huang, C. Z. In Situ Investigating the Size-Dependent Scattering Signatures and Sensing Sensitivity of Single Silver Nanocube through a Multi-Model Approach. *J. Colloid Interface Sci.* **2021**, *584*, 253–262.

(59) Sweeney, C. M.; Nehl, C. L.; Hasan, W.; Liang, T.; Eckermann, A. L.; Meade, T. J.; Odom, T. W. Three-Channel Spectrometer for Wide-Field Imaging of Anisotropic Plasmonic Nanoparticles. *J. Phys. Chem. C* **2011**, *115* (32), 15933–15937.

(60) Zou, B.; Liu, Y.; Yan, X.; Huang, C. Gold Nanoparticles Based Digital Color Analysis for Quinidine Detection. *Chin. Sci. Bull.* **2013**, *58* (17), 2027–2031.

CHAPTER 4: IMPROVING HOMOGENEITY OF SILVER NANOPARTICLE SURFACE CHEMISTRY BY MIXED CHARACTER SILVER-SULFIDE SHELLS

4.1 Introduction

The inherent heterogeneity in nanoparticle surface chemistry strongly influences the performance of silver nanoparticles (Ag NPs), making it difficult to derive quantitative structure-function relationships when using them in applications such as (photo) catalysis/sensing,[1,2] surface-enhanced Raman scattering (SERS),[3,4] and environmental ecotoxicity studies.[5,6] The impact of heterogeneous surface chemistries is especially apparent when examining Ag NP performance in electrochemical environments, where differences in particle-to-particle electrochemical activity is commonly observed.[7–11] Mechanistic insight into the role of NP surface chemistries can be revealed by combining electrochemical and optical techniques (e.g., dark-field scattering) where NPs undergoing physical changes (such as size and shape) during electrochemical perturbation can be observed as changes in optical signatures. As discussed in Chapter 1 of this dissertation, we previously explored the influence of surface oxides on the electrodissolution of single Ag NPs.[12,13] In these studies, dark-field scattering, super-localization imaging, and polarization-resolved measurements revealed variations in dissolution kinetics as well as NP shape were caused by asymmetric surface oxides on single NPs. The variability in surface chemistry associated with native surface oxides impacts our ability to untangle the roles played by other potentially perturbative effects in electrochemical studies, such as contact between the NP and supporting substrate or the role of the supporting electrolyte.[14–17] Thus, there is a critical need for developing new strategies to improve the homogeneity of the surface chemistry of Ag NPs, such that more reproducible and predictable

electrochemical performance can be achieved, while also allowing for more robust structure-function relationships to be derived.

In this work, we demonstrate a post-synthesis approach for improving the consistency of Ag NP surface chemistry by chemically growing a sacrificial silver-sulfide (Ag_2S) shell that competes with unwanted contaminants on the silver surface (Figure 4.1). After growth, the silver-sulfide shell is cathodically stripped away, revealing a more pristine, and ideally, reproducible silver surface when compared to the starting material. To benchmark the ability of the sacrificial silver-sulfide shell to "reset" the surface chemistry of the Ag NPs to a more homogeneous starting point, we monitor their electrodissoluion kinetics, where we expect a more silver-like surface to undergo rapid dissolution to Ag^+. Our sacrificial shell approach not only provides insight into how surface chemistry impacts performance at the single nanoparticle level, but also offers a path towards achieving more uniform nanoparticle surfaces. Additionally, these studies revealed that multiple silver-sulfide species form at the surface of Ag NPs during sulfidation depending on the concentration of sulfide used, a discovery that demonstrates the ability of correlated optical electrochemical approaches to probe diverse chemistries on NP surfaces.

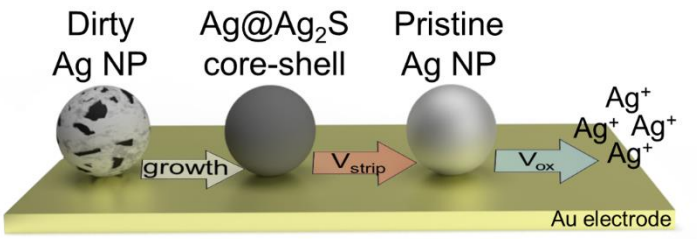

Figure 4.1. A schematic of the post-synthesis sacrificial silver-sulfide shell approach in which a sacrificial Ag_2S shell is chemically grown on the surface of surface-contaminated (dirty) Ag NPs, then electrochemically stripped, revealing a more silver-like surface. Electrodissolution kinetics (as revealed by changes in the optical signatures) of the recovered Ag NPs are used to benchmark changes in surface chemistry.

4.2 Characterizing Growth of Silver-Sulfide Shell on Ag NPs

Silver-sulfide was chosen as the starting system to test our sacrificial shell strategy due to the high affinity of sulfide to bind to the silver surface, making growth on Ag NPs straightforward, in addition to the extensive literature on this system.[18–22] The electrochemical formation of Ag_2S on Ag NPs has been shown by White and coworkers to occur according to Equation 4.1 and our proposed cathodic half-reaction in Equation 4.2:[23]

$$2\ Ag\ (s) + HS^- + OH^- \rightleftarrows Ag_2S\ (s) + H_2O + 2e^- \qquad \text{(Eq. 4.1)}$$

$$O_2 + 2\ H_2O + 4e^- \rightleftarrows 4OH^- \qquad \text{(Eq. 4.2)}$$

In our studies, we use a chemical, rather than electrochemical, approach to grow Ag_2S on commercial Ag NPs by introducing varying concentrations of sodium sulfide, Na_2S, to our nanoparticle solution and using similar reaction conditions as the White group (see Chapter 2 for additional details). For the shell growth, we work at pH = 12 such that bisulfide (HS^-) is the dominant sulfide form based on its acid dissociation constants;[24] thus, we will report the total concentration of sulfide-containing species for our varying reaction conditions as [HS^-]. We first confirmed the chemical growth of Ag_2S on the surface of the Ag NPs by measuring the bulk extinction spectra for Ag NPs after undergoing sulfidation with varying

[HS^-] (Figure 4.2). The extinction spectra show a red shift and increased damping as the Ag NPs are exposed to increasing [HS^-], consistent with other reports on the sulfidation of silver.[25]

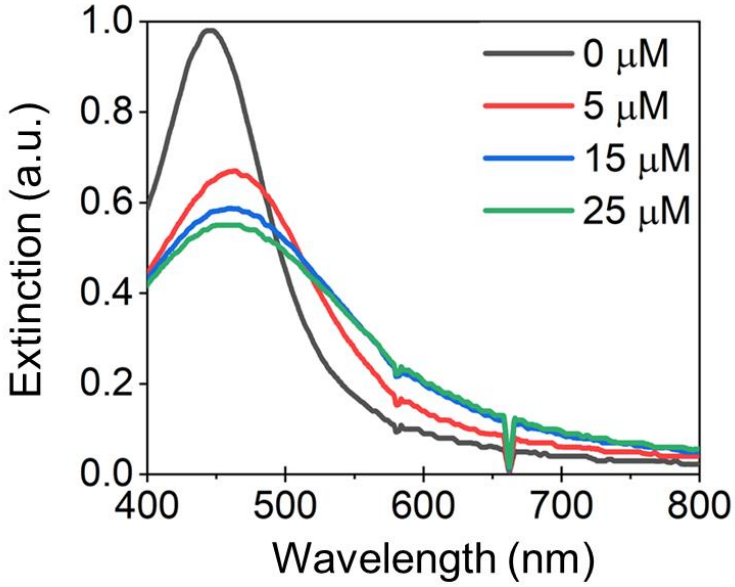

Figure 4.2. Extinction spectra of bulk Ag NPs reacted with varying [HS^-]. As [HS^-] increase from 0 μM to 25 μM thicker shells are expected to grow on the surface of the Ag NPs, leading to a red shift and plasmon damping, as previously reported.[25] Each spectrum was taken 30 minutes after the addition of Na_2S to the Ag NPs (in a pH = 12 solution).

To characterize the formation of shell growth on single Ag NPs, transmission electron microscopy (TEM) images of unreacted Ag NPs and Ag NPs after sulfidation were taken with correlated energy dispersive X-ray (EDX) spectroscopy. Figures 4.3 and 4.4 show representative TEM images of an unreacted Ag NPs and Ag NPs reacted with 50 μM HS^- (where a Ag_2S shell is expected to form – i.e. Ag@Ag_2S), respectively. Comparing the single particle TEM images in Figures 4.3A and 4.4A we can see the presence of a chemically distinct species surrounding the Ag NP that was reacted with 50 μM HS^- from the lighter gradient halo surrounding the dark core NP. Additionally, the corresponding EDX spectra for both particles show that sulfur is only present for the reacted NP. While

these images suggest we are growing a chemically distinct species during our sulfidation reaction, and that sulfur is present, the TEM detector was not able to identify the shell as a silver-sulfide species. To gain further insight into the chemical identity of the exterior shell that we observed in Figure 4.4, we imaged the same batch of unreacted Ag NPs and Ag NPs reacted with 50 μM HS^- in a high-resolution TEM (HR-TEM) that could provide elemental mapping of the NPs. Figure 4.5 shows representative TEM and elemental mapping images with the corresponding EDX spectra for Ag NP and Ag@Ag_2S NPs. The corresponding elemental mapping and EDX spectra confirms the presence of surface sulfide as the areas of lighter contrast on exterior of the darker-contrasted core Ag NP in the TEM images, thus confirming our chemical synthesis procedure is successful at growing the desired shell. Interestingly, in both cases where the Ag NP was reacted with a high [HS^-], we see the shape of the NP become more distorted (less spherical) when compared to the unreacted Ag NPs. This may indicate that during sulfidation the reactive sulfide integrates into the core NP structure with a silver-sulfide species displacing the solid silver core. Optical and electrochemical data discussed in the following sections suggest that this could be a source of heterogeneity in the measurements.

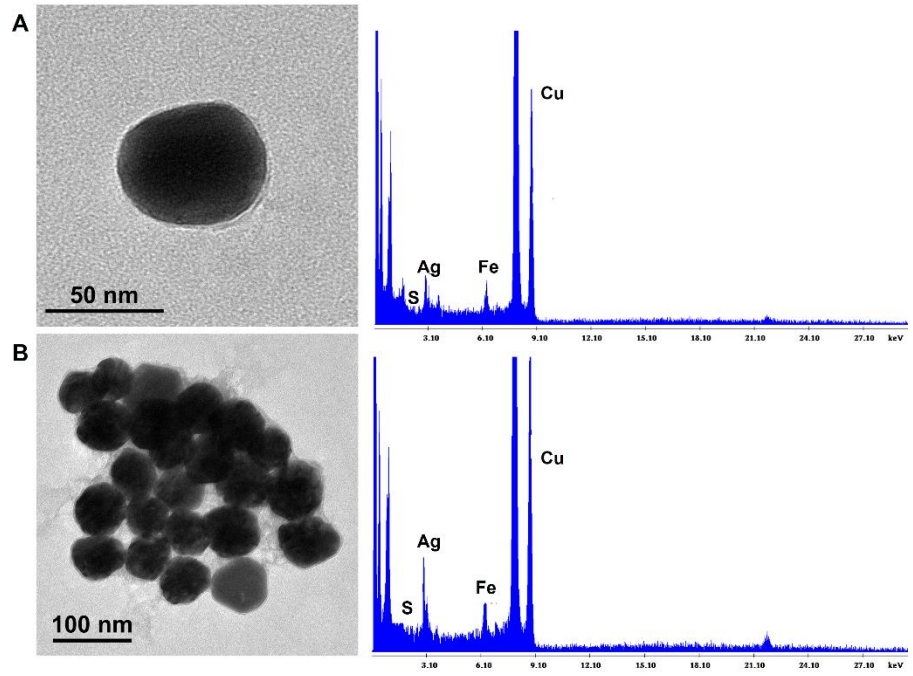

Figure 4.3. (A) TEM image and corresponding EDX spectra of a single unreacted Ag NP showing no sulfide species is present on the Ag NP. (B) TEM image and corresponding EDX spectra for an aggregated sample of unreacted Ag NPs.

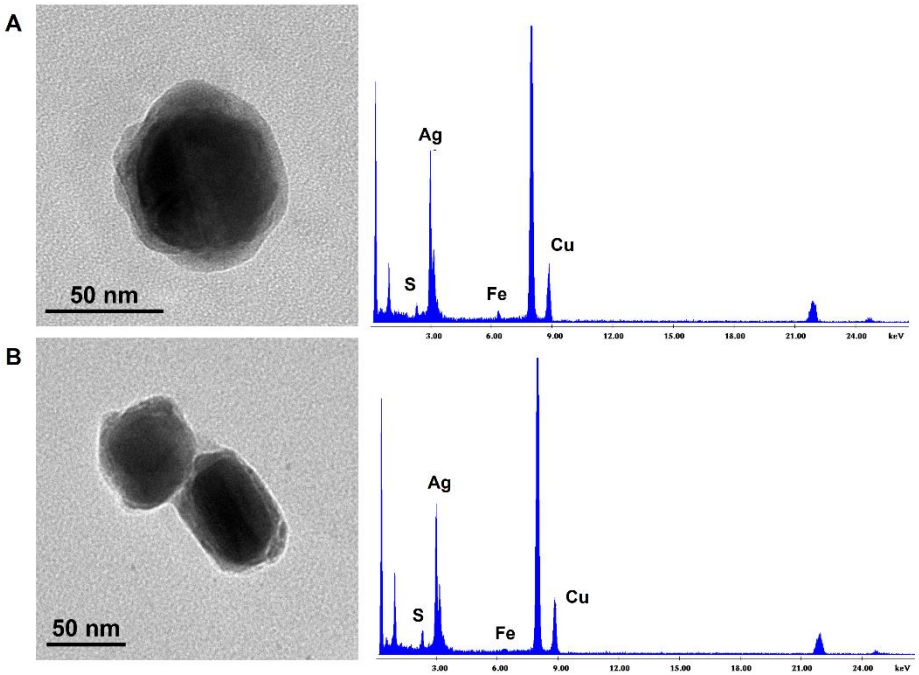

Figure 4.4. (A) TEM image and corresponding EDX spectra of a single Ag NP that was reacted with 50 µM HS^- (where a Ag_2S shell is expected to form – i.e. $Ag@Ag_2S$) showing a chemically distinct shell has formed on the exterior of the NP with a sulfur signal visible in the spectra. (B) TEM image and corresponding EDX spectra for a dimer Ag NP that was reacted with 50 µM HS^-

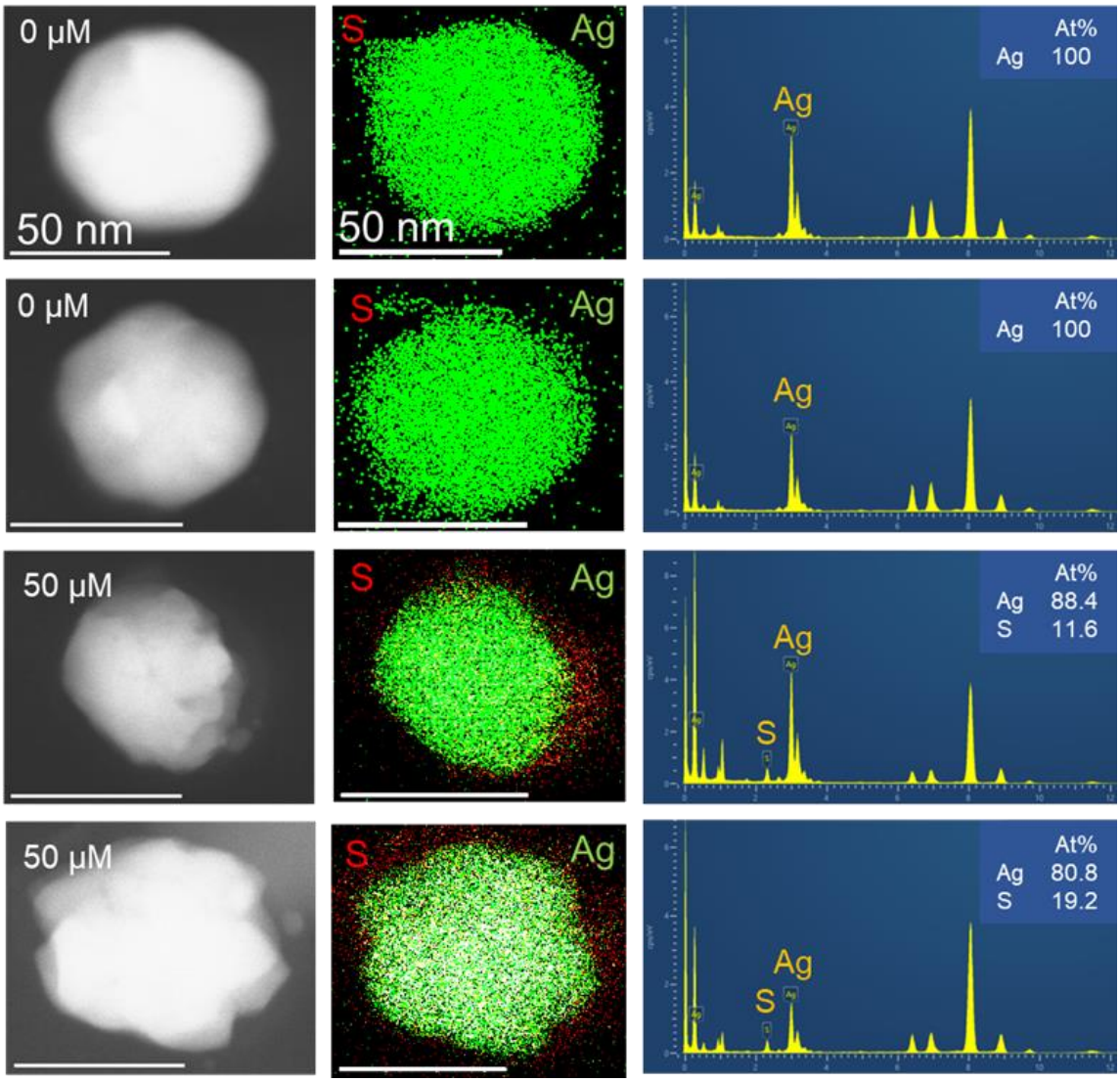

Figure 4.5. TEM image, elemental mapping, and energy-dispersive x-ray (EDX) spectra for two representative unreacted Ag NPs (0 µM) and two Ag NPs after reacting with 50 µM HS^- solution. Here, the elemental mapping and EDX spectra suggest the contrast difference seen in the TEM image is an exterior surface sulfide species. Scale bars = 50 nm.

4.3 Characterizing the Scattering Intensities of Ag NPs with Varying [HS^-]

Next, we used single NP dark-field scattering to probe how the presence of the Ag_2S shell impacts both the scattering intensity and heterogeneity in a population of Ag NPs (Figure 4.6). Dark-field scattering is particularly useful for these studies as Ag NPs

exhibit strong light scattering characteristics due to a localized surface plasmon resonance lying in the visible region; therefore, changes to the surface of Ag NPs because of shell growth and removal is easily identifiable as a change in their optical signatures.[12,13] Histograms of the scattering intensities of more than 120 nanoparticles exposed to varying [HS^-] are shown in Figure 4.7. For the unreacted nanoparticles (0 μM HS^-), we observe a broad distribution of scattering intensities, illustrating the inherent heterogeneity in our starting population of commercial nanoparticles. As the [HS^-] increases from 2.5 μM to 7.5 μM, we observe both a decrease in the scattering intensity as well as a narrowing of the intensity distribution, suggesting both plasmon damping due to the formation of the shell as well as increased uniformity of the surface across the population. However, this trend surprisingly reverses at 10 μM HS^-, with a shift towards higher scattering intensities, accompanied by broadening in the distributions over several [HS^-]. The trend then reverses again at [HS^-] ≥ 15 μM, with a return to damped scattering and narrowing of the intensity histograms. To better illustrate this trend, Figure 4.8 shows the average scattering intensity as a function of [HS^-], where the scattering intensity at intermediate [HS^-] approaches the intensity of the unreacted nanoparticles (dashed line), a surprising result given the presence of a sulfide-containing shell.

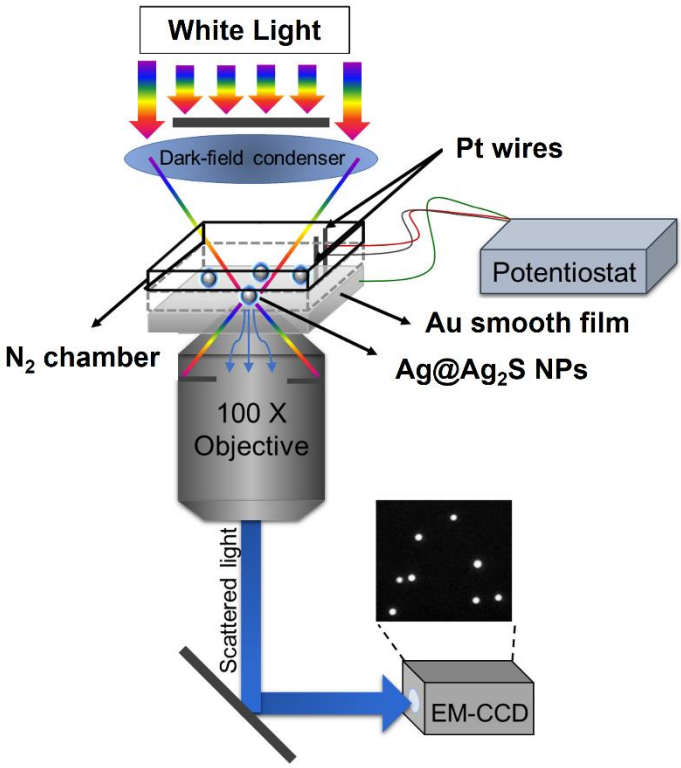

Figure 4.6. General schematic of dark-field microscope setup. White light passes through the dark-field condenser to illuminate the NPs. The low angle light scattered from the NPs is collected through an objective and imaged onto an EM-CCD camera. The resulting dark-field image produces a dark background with bright spots that represent the electrode surface and the location of diffraction limited Ag NPs, respectively. By synchronizing the collection of images from the camera with a potentiostat, we can monitor changes in scattering intensities with an applied potential.

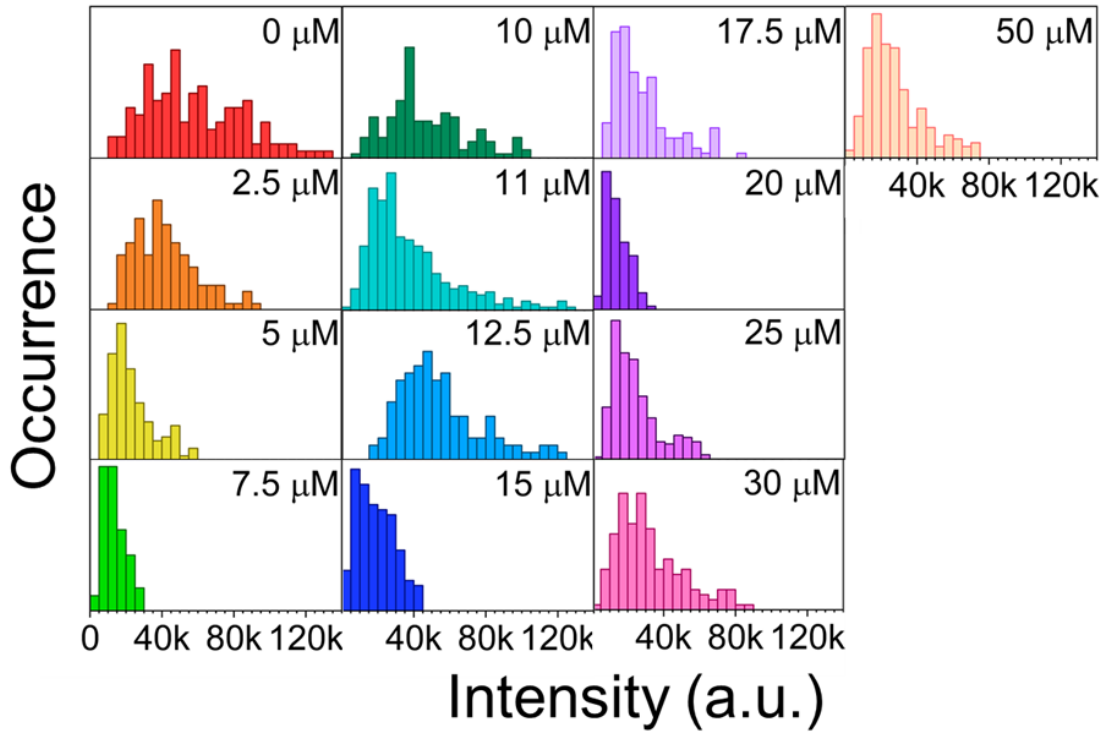

Figure 4.7. Histograms showing the distribution of scattering intensities for individual Ag NPs after reacting with varying [HS^-]. More than 120 nanoparticles were examined for each [HS^-].

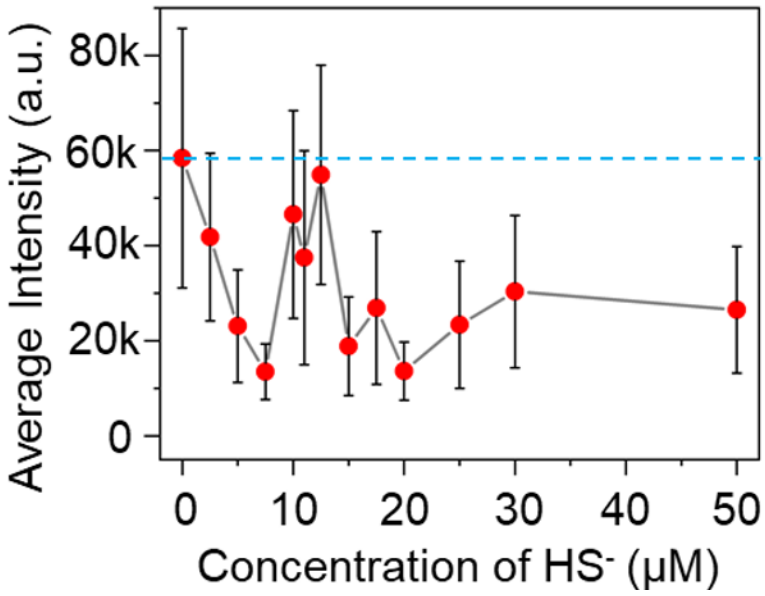

Figure 4.8. Average scattering intensities (from histograms in Figure 4.7) as function of [HS^-]. The dashed line represents the initial average scattering intensity of Ag NPs from a commercial source.

4.4 Examining Electrodissolution Kinetics of Ag NPs after Electrochemical Removal of Ag_2S Shell

To gain insight into the origin of the sulfide concentration-dependent change in scattering intensity upon shell growth, we explored both reductive shell removal as well as the electrodissolution kinetics of the Ag NPs. For these studies, we performed a potential step experiment in which we first applied a reductive potential to strip the sacrificial Ag_2S shell, followed by an oxidizing potential to electrodissolve the newly exposed Ag NP to Ag^+ (as shown schematically in Figure 4.1). For all experiments discussed below, the potentials are reported relative to an Ag|AgCl reference electrode. The two reactions involved in the stripping and dissolution, respectively, are shown below:

$$Ag_2S\ (s) + H_2O + 2e^- \xrightarrow{V_{strip}} 2\ Ag\ (s) + HS^- + OH^- \qquad \text{(Eq. 4.3)}$$

$$Ag\ (s) \xrightarrow{V_{ox}} Ag^+ + e^- \qquad \text{(Eq. 4.4)}$$

Figure 4.7 shows intensity-time traces of two representative behaviors observed during each electrochemical step for particles after sulfidation in a 15 μM HS^- solution. In Figure 4.9A, the application of a -1.1 V stripping potential at t = 10 s led to a stepwise increase in the scattering intensity to nearly twice its starting value, indicating rapid removal of the Ag_2S from the nanoparticle and ideally generating a more silver-like surface. Next, we stepped the potential to an oxidizing value of 0.7 V at t = 70 s, and we observed a stepwise drop in the scattering intensity to background, showing that the particle dissolved almost immediately, consistent with our picture of a more silver-like surface. Figure 4.19B shows a different behavior in which introducing the stripping potential generated a sluggish rise in the scattering intensity with an intensity increase of ~30% of the starting value,

suggesting slow reduction of the silver-sulfide shell and the possibility of contaminants remaining on the surface. When we stepped to the oxidizing potential, we observed complete electrodissolution of the nanoparticle, as evidenced by the scattering decrease to background, although the kinetics appear to show multiple time scales and are slower than the particle shown in Figure 4.9A. This observation further supports our hypothesis that some surface contaminants remain on this particle.

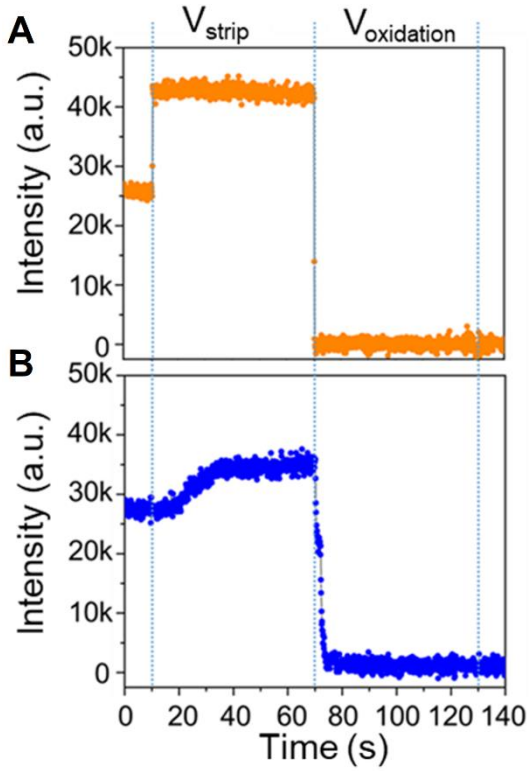

Figure 4.9. Representative potential-step intensity-time traces for two different Ag NPs with sacrificial shells formed in 15 μM HS^-. (A) NP undergoing immediate shell removal and fast oxidation, indicating a more silver-like surface achieved. (B) NP with sluggish shell removal and slower oxidation kinetics suggesting contaminants remain. The potential waveform is as follows: t = 0 – 10s, open circuit potential; t = 10 – 70 s, V_{strip} = -1.1 V (removal of silver-sulfide shell); t = 70 – 130 s, V_{ox} = 0.7 V (electrodissolution of Ag NPs); and t = 130 – 140 s, open circuit potential. A 10 mM citrate buffer (pH 9) was used as supporting electrolyte for stripping and oxidation steps.

To characterize how the concentration of added HS^- affects the removal of the silver-sulfide shells, we first compare the average scattering intensities of the nanoparticles passivated by the sacrificial shell to the average scattering intensities after shell removal at -1.1 V (Figure 4.10A, red and blue data, respectively). In the low [HS^-] regime (highlighted in orange), we observe almost no change in the scattering intensity upon the application of a stripping potential, suggesting that the shell species that was formed on these nanoparticles is not removed. On the other hand, in the intermediate concentration regime (highlighted in green), we find that the intensity of the Ag NPs not only increases relative to the shell-passivated values but is as high or even higher than the scattering intensity of the as-purchased nanoparticles (dashed line), suggesting that we have successfully recovered a more silver-like surface. The change in behavior between the low concentration and intermediate concentration regimes indicates that different species are formed at the surface of the particles as the [HS^-] is tuned. At the highest [HS^-] (highlighted in purple), we observe an increase in scattering intensity upon shell removal, although the intensity never reaches that of the as-purchased nanoparticles, suggesting that the shell has not been completely removed. Based on the elemental mapping shown for the Ag NPs reacted with 50 μM HS^- (Figure 4.5), we believe at high concentrations Ag_2S begins to integrate into the Ag NP core, changing the structure, and influencing the ability to electrochemically remove an exterior Ag_2S shell. Thus, our data indicates that there is an optimal [HS^-] range for the growth and successful removal of the sacrificial shells.

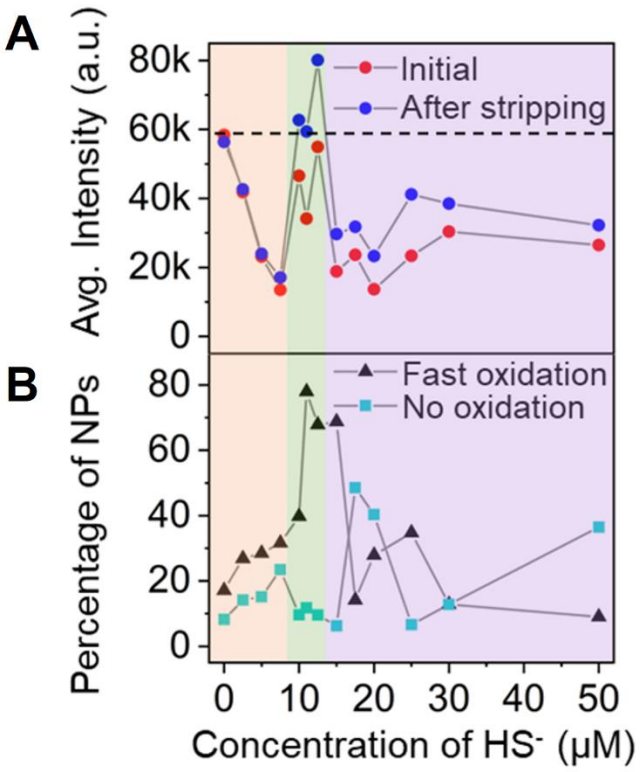

Figure 4.10. (A) Average scattering intensities before (red) and after (blue) electrochemical stripping of the sacrificial silver-sulfide shell from Ag NPs as a function of [HS^-]. The dashed line serves as guide for the starting intensity of the purchased Ag NPs. The solid line connecting the data points helps to guide the eye. (B) Percentage of NPs that show fast oxidation kinetics (scattering intensity decays in < 0.5 s, black data) versus percentage that show no oxidation (no change in scattering intensity, cyan data). Orange, green, and purple shaded regions designate the three concentration regimes discussed in the text.

Next, we benchmarked the electrochemical reactivity of the Ag NPs after shell removal by examining their electrodissolution kinetics under an oxidizing potential. As with our previous work,[12,13] we classify an Ag NP as having fast oxidation kinetics when the scattering intensity from that nanoparticle decays to background levels in less than 0.5 s and slow oxidation kinetics when the scattering intensity decays over periods longer than 0.5 s. Fast oxidation kinetics are indicative of more pristine silver-like surface, while slow oxidation kinetics indicate the presence of passivating surface contaminants.[12,13] Alternatively, if a Ag NP shows no change in scattering intensity during the 60 s in which

the oxidation potential is applied, that NP is classified as having no oxidation, indicating that there is either complete passivation of the surface or that the nanoparticle is not in electrochemical contact with the supporting electrode.

Figure 4.10B shows the percentage of nanoparticles for a given [HS^-] regime that undergo fast oxidation versus no oxidation after sacrificial shell removal. The figure reveals a clear relationship between the three concentration regimes identified in Figure 4.10A and the observed electrodissolution kinetics. In the low [HS^-] regime (highlighted in orange), we observe a gradual rise in both the number of fast oxidizing particles as well as non-oxidizing particles as the concentration of [HS^-] increases. Based on work done by White and coworkers,[18–20] we propose that this behavior is a result of AgSH adlayers, rather than Ag_2S, being formed on the surface of the Ag NPs during sulfidation at low [HS^-]. Cyclic voltammetry studies on silver surfaces show that surface-adsorbed AgSH adlayers can precede monolayer Ag_2S coverage according to the equations below:[18,19]

$$Ag\ (s) + HS^- \rightleftarrows AgSH_{ads} + e^- \qquad \text{(Eq. 4.5)}$$

$$AgSH_{ads} + Ag\ (s) + OH^- \rightleftarrows Ag_2S_{ads}\ (s) + H_2O + e^- \qquad \text{(Eq. 4.6)}$$

Previous work has shown that the cathodic wave associated with the removal of the AgSH adlayers shows two peaks, one of which is centered around -1.3 V (which we will call type A, following the convention of White and coworkers[18,19]) and the other around -1.1 V (type B). Thus, we propose that differences in the surface adlayer characteristics leads to the increasing populations of both fast and non-oxidizing nanoparticles as [HS^-] increases in the low concentration regime. For Ag NPs in which the surface adlayer is dominated by type A characteristics, the sacrificial shell remains on the surface when we apply a stripping potential of -1.1 V, preventing subsequent oxidation. For Ag NPs in which the surface

adlayer is dominated by type B characteristics, the sacrificial shell can be successfully removed at our applied stripping potential, leading to fast oxidation kinetics. This hypothesis is further supported by examining our single NP intensity data in which the Ag NPs that show fast oxidation kinetics are also associated with an increase in scattering intensity upon shell stripping (Figure 4.12). Moreover, when we increased our stripping potential to -1.4 V, which should remove both type A and B adlayers, we found that we could further increase the population of fast oxidizing particles (Figure 4.13), consistent with this mechanistic picture.

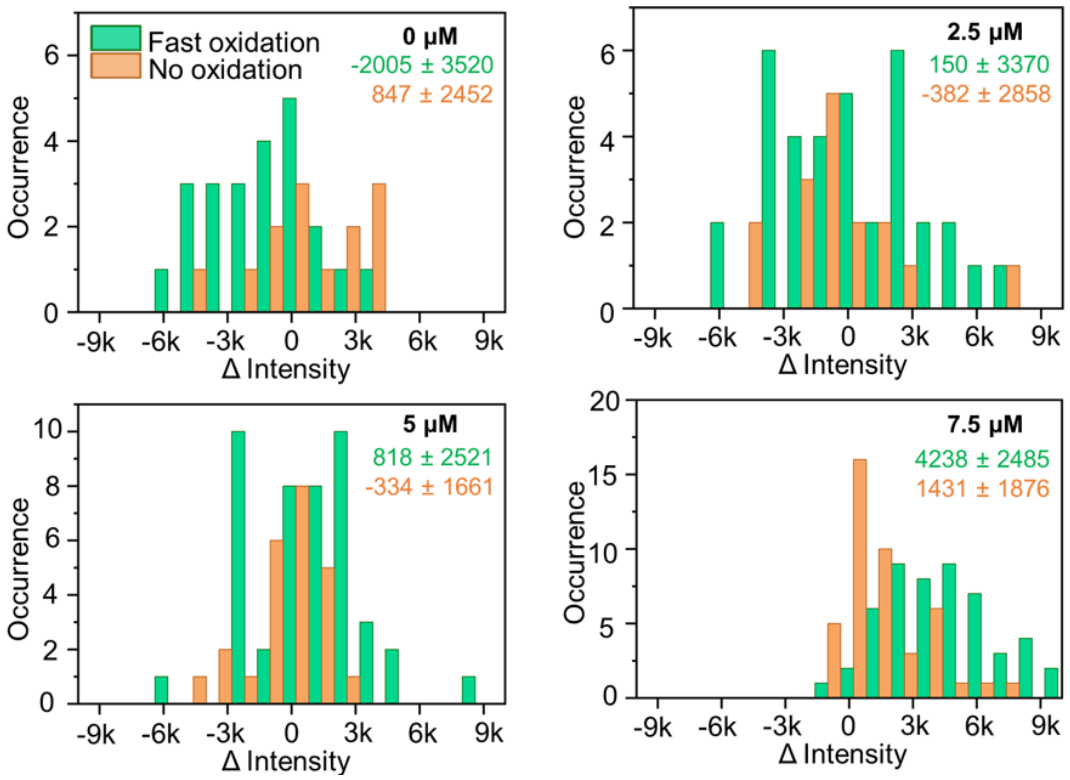

Figure 4.11. Histograms of the change in scattering intensity (ΔI) of the Ag NPs after reductive stripping and before reductive stripping (e.g., "without" shell vs. "with" shell). For the as-purchased NPs (0 µM), most of the NPs undergoing fast oxidation (green) show either no change in their scattering intensity or even a decrease in scattering intensity upon application of a stripping potential. In the low [HS^-] regime, we attribute the diverse behavior to mixed character surfaces formed at low [HS^-] where AgSH adlayer coverage is expected to be less than 50% of the NP surface and thus why a positive shift in ΔI is not always seen, particularly in the 2.5 and 5 µM histograms. NPs that undergo fast oxidation after reacting with 7.5 µM show a more dramatic positive shift in ΔI, demonstrating the correlation between complete shell removal and efficient dissolution of the NP. Interestingly, NPs that did not undergo oxidation in this concentration also showed a positive ΔI. We propose these NPs have a type of AgSH adlayer where -1.1 V is not effective at stripping and why no dissolution is observed.[18,19]

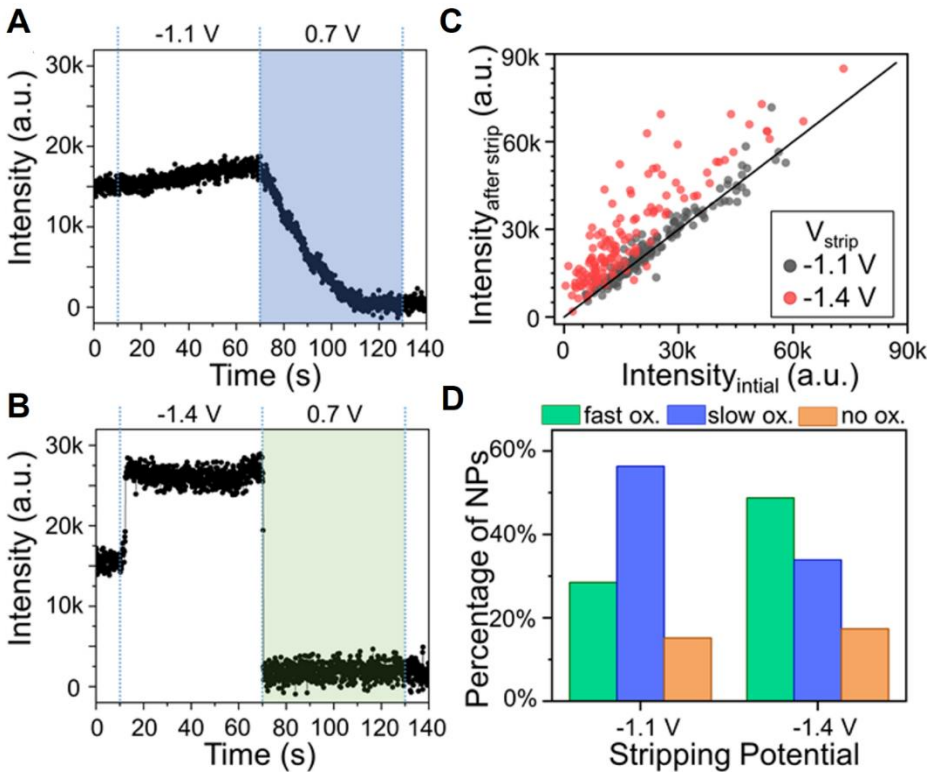

Figure 4.12. Confirming presence of multiple adlayers types, where -1.1 V is sufficient to strip type B but requires a more negative potential of -1.4 V to strip type A. (A) Representative intensity-time trace for Ag NP reacted with 5 μM HS^- with insufficient stripping potential of -1.1 V. Blue shaded region demonstrating slow oxidation kinetics. (B) Representative intensity-time trace for Ag NP reacted with 5 μM HS^- with more reducing stripping potential of -1.4 V. Green shaded region indicating fast oxidation kinetics. (C) Scattering intensity *after* stripping vs. *initial* scattering intensity (before stripping) over a population of nanoparticles at different stripping potentials (D) Comparison of oxidation kinetics over the same population of NPs after different stripping potentials applied.

Looking now at the intermediate [HS^-] regime (highlighted in green in Figure 4.10), we see that ≥ 70% of the Ag NPs undergo fast oxidation after removal of the shells. This behavior stands in stark contrast to the behavior of the Ag NPs that had no sacrificial shell (0 μM HS^-) where less than 20% of the nanoparticles had fast oxidation kinetics, supporting our hypothesis that Ag NP surfaces can be "reset" to a more silver-like state through the introduction of sacrificial shells. Moreover, unlike the low concentration regime, the

emergence of a sizable population of fast oxidizing particles suggests that we are successfully removing most of the sacrificial shells formed in the intermediate concentration regime. We believe that this change in behavior from the low [HS^-] regime is due to a transition from AgSH adlayer formation to Ag_2S monolayer formation.[18–20] The monolayer formation is associated with both the rise in scattering intensity of the nanoparticles upon shell formation and removal (Figure 4.10A) as well as faster oxidation kinetics after shell removal (Figure 4.10B). We do note, however, that there appears to be a slight concentration offset between the emergence of increased scattering due to shell removal (transition from orange to green in Figure 4.10A) and the increased population of fast oxidizing particles. We will discuss this in more detail below. We also note that the population of nanoparticles that show no oxidation never drops below ~10% in this regime, similar to the value observed for the untreated Ag NPs, suggesting that there is a nonreactive sub-population within the sample that is unaffected by the chemistry we are performing.

In the high [HS^-] regime (highlighted in purple in Figure 4.10), we observe concentration-dependent variations in the relative populations of fast and no oxidation behavior. At [HS^-] of 17.5 and 20.0 μM, a sizable population (> 40%) emerges in which no oxidation is observed, accompanied by a significant drop in the number of Ag NPs showing fast oxidation. However, at a [HS^-] of 25 μM, this behavior inverts, with fast oxidation occurring for ~30% of the particles, while those showing no oxidation returned to levels ~10%. Interestingly, this concentration is twice that of the concentration at which we observe the highest fraction of fast oxidizing Ag NPs in the intermediate regime (12.5 vs. 25 μM), suggesting that this behavior is indicative of Ag_2S bilayer formation.[20] It is

possible that the formation of bilayer Ag_2S is a transition point where sulfide integrates into the core Ag NP structure, further confirming our earlier hypothesis of poor shell removal at higher [HS^-]. Additionally, we find that at the highest [HS^-] concentrations tested, the population of fast oxidizing particles drops again, indicating that as the Ag_2S shells formed in this regime becoming increasingly thick, the applied stripping potential only generates partial removal, leading to surface passivation against rapid oxidation.

As noted above, there is a concentration-offset between the rise in scattering intensity associated with the transition between the low and intermediate concentration regimes (Figure 4.10A) and the emergence of a significant population of fast oxidizing particles (Figure 4.10B). Given that our data indicate a transition between AgSH adlayer formation and Ag_2S shells in this regime, we speculate that particles may have shells with mixed character,[22] which can lead to more complex kinetics. For example, Figure 4.13 shows a representative intensity-time trace, in which two consecutive stripping/oxidation cycles were performed. Initially, we performed stripping at -1.1 V and observed only a modest increase in the scattering intensity. Upon stepping to an oxidizing potential (highlighted in blue), we observed an initial slow drop in intensity to ~35% of its starting value, followed by even more sluggish oxidation with minimal change in intensity, suggesting that the surface was not contaminant free. Next, we applied a second stripping potential at a more negative value of -1.4 V and found a rapid, two-fold increase in the scattering intensity, indicating that additional surface material was removed. Upon returning to an oxidizing potential (highlighted in green), we observed fast oxidation kinetics, consistent with a more silver-like surface. This result suggests that reacting Ag NPs with [HS^-] in this intermediate concentration window not only leads to varying silver-

sulfide coverage across a population of particles (leading to broadening in the intensity histograms in Figure 4.7), but the transition between adlayer AgSH and monolayer Ag_2S is observable on the individual particles themselves. While not expected in our original experimental plan, this identification of multiple sulfide species on single Ag NPs demonstrates how single particle optical studies can provide insight to mechanisms lost in electrochemical measurements alone.

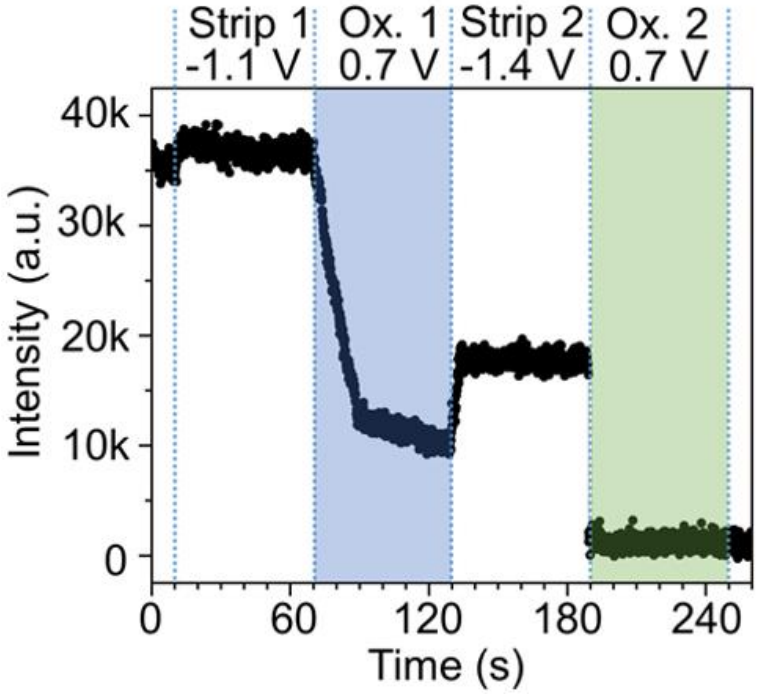

Figure 4.13. Representative intensity-time trace for an Ag NP reacted with 12.5 μM HS^- with the potential waveform of: t = 0 – 10 s, open circuit potential; t = 10 – 70 s, V_{strip} = -1.1 V; t = 70 – 130 s, V_{ox} = 0.7 V; t = 130 – 190 s, V_{strip} = -1.4 V; t = 190 – 250 s, V_{ox} = 0.7 V; t = 250 – 260 s, open circuit potential.

4.5 Testing effectiveness of intermediate [HS^-] at creating more silver-like surfaces

One additional strategy to test whether our sacrificial shell approach is effective at creating more uniform, silver-like surfaces is to lower the oxidation potential from 0.7 V to 0.3 V and determine how the kinetics of silver oxidation are affected. The histograms in Figure 4.14 show the fraction of NPs undergoing fast, slow, and no oxidation under

different shell formation/stripping conditions. To benchmark performance, we start with the as-purchased and unreacted Ag NPs (0 μM HS^-) and find that ~75% show no evidence of oxidation at this low oxidizing potential. Next, we compare Ag NPs in which a sacrificial shell was grown in 12.5 μM HS^- conditions. Using a -1.1 V stripping potential, a small population of fast oxidation events emerges and the number of particles showing no oxidation drops to ~50%. Increasing the stripping potential to -1.4 V leads to ~40% of the particles showing fast oxidation, with fewer than 20% showing no oxidation, despite the much lower oxidizing potential. The ability to transition a population of Ag NPs from having poor activity to high activity, even under relatively low oxidation potentials, highlights the power of the sacrificial shell strategy for generating populations of Ag NPs with more uniform, reproducible behavior. Moreover, these studies confirm the presence of multiple sulfide species as some of the shell remains after stripping at -1.1 V, even though evidence of their existence is hidden in our previous studies using a more positive oxidation potential (as in Figure 4.10). Thus, to ensure that the surface is indeed more silver-like, it is critical to use a more negative stripping potential for shell removal and test the oxidation kinetics under low oxidation potentials to gain a more complete understanding of the surface.

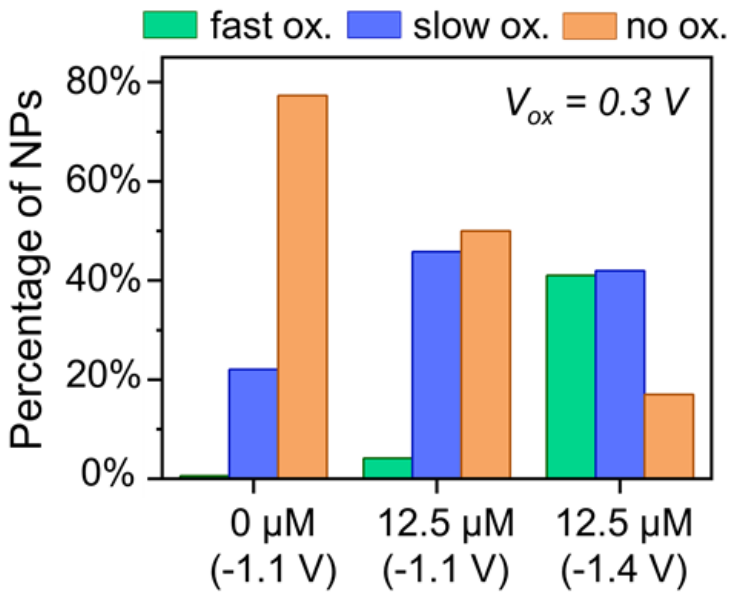

Figure 4.14. Comparison of oxidation kinetics at a low oxidizing potential of 0.3 V comparing populations of unperturbed NPs (0 μM HS^-) and NPs with shells formed with 12.5 μM HS^-. A more negative stripping potential of -1.4 V was applied to the unreactive NPs from 12.5 μM HS^- after -1.1 V was unsuccessful at removing the shell.

As we noted in these data, many particles seem to show mixed shell character, in which different AgSH adlayer types, as well as monolayer, bilayer, and quasi-bulk Ag_2S, can be present among a population of particles.[18–20] For studies in which more pristine silver-like surfaces are desired, this issue is easily addressed by using a more negative stripping potential to remove the sacrificial shells. However, Ag/Ag_2S nanocomposites are found in a range of applications including photocatalysis,[26] biosensing,[27] and electrochemical energy storage.[28] Moreover, $Ag@Ag_2S$ core-shell NPs have been shown to be less toxic to the environment than Ag NPs and therefore of possible interest for applications in the cosmetic and antibiotic industries where controlled leaching of silver ions from Ag NPs is of concern.[29–32] Having said this, the diversity of surface species that can (co)exist on the surface of the $Ag@Ag_2S$ nanoparticles suggests that careful studies

are needed both to understand which surface species dominate the nanoparticle properties in certain environments, as well as to control the composition of these types of particles.

4.6 Conclusions

Here we reported on a post-synthesis approach for improving the consistency of Ag NP surface chemistry by introducing a sacrificial silver-sulfide shell that outcompetes surface contaminants. Reductive stripping of the sacrificial shells revealed a more silver-like nanoparticle surface as validated through faster oxidation kinetics. Moreover, we found sulfide-dependent behavior that was attributed to different sulfide species being formed at the Ag NP surface during shell growth, including different types of AgSH adlayers, and evidence of Ag_2S monolayers and bilayers. These different surface species were found to co-exist, suggesting that Ag_2S shells are not uniform, even on the surface of a single nanoparticle. Our sacrificial shell approach not only provides a mechanism to improve the homogeneity of surface chemistry of commercial Ag NPs, leading to more reliable electrochemical performance and facilitating improved structure-function studies, but also generates unexpected insight into the dynamics of silver-sulfide shell growth on individual particles.

4.7 Acknowledgements

This work was supported by the U.S. National Science Foundation under grant number DMR-2003613. The authors would like to thank Natalia Y. Molina and Philip A. Reinhardt for their valuable discussions and suggestions throughout the experimental process. Additionally, we would like to thank Dr. Henry White, Dr. Martin A. Edwards, and Dr. Donald A. Robinson for their feedback and discussions on preliminary experimental results, as well as protocols for the chemical synthesis of silver-sulfide shells; and Dr. Xingchen Ye and Jun Chen for performing TEM and EDX analysis on our synthesized nanoparticles.

4.8 References

(1) Lucky, S. S.; Soo, K. C.; Zhang, Y. Nanoparticles in Photodynamic Therapy. *Chem. Rev.* **2015**, *115* (4), 1990–2042.

(2) Willets, K. A.; Van Duyne, R. P. Localized Surface Plasmon Resonance Spectroscopy and Sensing. *Annu. Rev. Phys. Chem.* **2007**, *58* (1), 267–297.

(3) Joshi, P.; Zhou, Y.; Ahmadov, T. O.; Zhang, P. Quantitative SERS-Based Detection Using Ag–Fe $_3$ O $_4$ Nanocomposites with an Internal Reference. *J Mater Chem C* **2014**, *2* (46), 9964–9968.

(4) Willets, K. A.; Wilson, A. J.; Sundaresan, V.; Joshi, P. B. Super-Resolution Imaging and Plasmonics. *Chem. Rev.* **2017**, *117* (11), 7538–7582.

(5) Levard, C.; Hotze, E. M.; Lowry, G. V.; Brown, G. E. Environmental Transformations of Silver Nanoparticles: Impact on Stability and Toxicity. *Environ. Sci. Technol.* **2012**, *46* (13), 6900–6914.

(6) Tejamaya, M.; Römer, I.; Merrifield, R. C.; Lead, J. R. Stability of Citrate, PVP, and PEG Coated Silver Nanoparticles in Ecotoxicology Media. *Environ. Sci. Technol.* **2012**, *46* (13), 7011–7017.

(7) Wilson, A. J.; Jain, P. K. Light-Induced Voltages in Catalysis by Plasmonic Nanostructures. *Acc. Chem. Res.* **2020**, *53* (9), 1773–1781.

(8) Andreescu, D.; Kirk, K. A.; Narouei, F. H.; Andreescu, S. Electroanalytic Aspects of Single-Entity Collision Methods for Bioanalytical and Environmental Applications. *ChemElectroChem* **2018**, *5* (20), 2920–2936.

(9) Zamborini, F. P.; Bao, L.; Dasari, R. Nanoparticles in Measurement Science. *Anal. Chem.* **2012**, *84* (2), 541–576.

(10) Patrice, F. T.; Qiu, K.; Ying, Y.-L.; Long, Y.-T. Single Nanoparticle Electrochemistry. *Annu. Rev. Anal. Chem.* **2019**, *12* (1), 347–370.

(11) Tschulik, K.; Batchelor-McAuley, C.; Toh, H.-S.; Stuart, E. J. E.; Compton, R. G. Electrochemical Studies of Silver Nanoparticles: A Guide for Experimentalists and a Perspective. *Phys Chem Chem Phys* **2014**, *16* (2), 616–623.

(12) Sundaresan, V.; Monaghan, J. W.; Willets, K. A. Visualizing the Effect of Partial Oxide Formation on Single Silver Nanoparticle Electrodissolution. *J. Phys. Chem. C* **2018**, *122* (5), 3138–3145.

(13) Sundaresan, V.; Monaghan, J. W.; Willets, K. A. Monitoring Simultaneous Electrochemical Reactions with Single Particle Imaging. *ChemElectroChem* **2018**, *5* (20), 3052–3058.

(14) Wei, W.; Yuan, T.; Jiang, W.; Gao, J.; Chen, H.-Y.; Wang, W. Accessing the Electrochemical Activity of Single Nanoparticles by Eliminating the Heterogeneous Electrical Contacts. *J. Am. Chem. Soc.* **2020**, *142* (33), 14307–14313.

(15) Wonner, K.; Evers, M. V.; Tschulik, K. Simultaneous Opto- and Spectro-Electrochemistry: Reactions of Individual Nanoparticles Uncovered by Dark-Field Microscopy. *J. Am. Chem. Soc.* **2018**, *140* (40), 12658–12661.

(16) Wonner, K.; Rurainsky, C.; Tschulik, K. Operando Studies of the Electrochemical Dissolution of Silver Nanoparticles in Nitrate Solutions Observed With Hyperspectral Dark-Field Microscopy. *Front. Chem.* **2020**, *7*.

(17) Brasiliense, V.; Patel, A. N.; Martinez-Marrades, A.; Shi, J.; Chen, Y.; Combellas, C.; Tessier, G.; Kanoufi, F. Correlated Electrochemical and Optical Detection Reveals the Chemical Reactivity of Individual Silver Nanoparticles. *J. Am. Chem. Soc.* **2016**, *138* (10), 3478–3483.

(18) Hatchett, D. W.; Gao, X.; Catron, S. W.; White, H. S. Electrochemistry of Sulfur Adlayers on Ag(111). Evidence for a Concentration- and Potential-Dependent Surface-Phase Transition. *J. Phys. Chem.* **1996**, *100* (1), 331–338.

(19) Hatchett, D. W.; White, H. S. Electrochemistry of Sulfur Adlayers on the Low-Index Faces of Silver. *J. Phys. Chem.* **1996**, *100* (23), 9854–9859.

(20) Conyers, J. L.; White, H. S. Electrochemical Growth of Ag2S on Ag(111) Electrodes. Coulometric and X-Ray Photoelectron Spectroscopic Analysis of the Stepwise Formation of the First and Second Monolayers of Ag2S. *J. Phys. Chem. B* **1999**, *103* (11), 1960–1965.

(21) Li, N.; Maurice, V.; Klein, L. H.; Marcus, P. Structure and Morphology Modifications of Silver Surface in the Early Stages of Sulfide Growth in Alkaline Solution. *J. Phys. Chem. C* **2012**, *116* (12), 7062–7072.

(22) Lastraioli, E.; Loglio, F.; Cavallini, M.; Simeone, F. C.; Innocenti, M.; Carlà, F.; Foresti, M. L. In Situ Scanning Tunneling Microscopy Investigation of Sulfur Oxidative Underpotential Deposition on Ag(100) and Ag(110). *Langmuir* **2010**, *26* (22), 17679–17685.

(23) Robinson, D. A.; White, H. S. Electrochemical Synthesis of Individual Core@Shell and Hollow Ag/Ag $_2$ S Nanoparticles. *Nano Lett.* **2019**, *19* (8), 5612–5619. h

(24) Li, Q.; Lancaster, J. R. Chemical Foundations of Hydrogen Sulfide Biology. *Nitric Oxide Biol. Chem.* **2013**, *35*, 21–34.

(25) Estrada-Mendoza, T. A.; Willett, D.; Chumanov, G. Light Absorption and Scattering by Silver/Silver Sulfide Hybrid Nanoparticles. *J. Phys. Chem. C* **2020**, *124* (49), 27024–27031.

(26) Liu, G.; Du, K.; Xu, J.; Chen, G.; Gu, M.; Yang, C.; Wang, K.; Jakobsen, H. Plasmon-Dominated Photoelectrodes for Solar Water Splitting. *J. Mater. Chem. A* **2017**, *5* (9), 4233–4253.

(27) Liu, B.; Ma, Z. Synthesis of Ag2S–Ag Nanoprisms and Their Use as DNA Hybridization Probes. *Small* **2011**, *7* (11), 1587–1592.

(28) Hwa, Y.; Park, C.-M.; Sohn, H.-J. The Electrochemical Characteristics of Ag2S and Its Nanocomposite Anodes for Li-Ion Batteries. *J. Electroanal. Chem.* **2012**, *667*, 24–29.

(29) Ivask, A.; ElBadawy, A.; Kaweeteerawat, C.; Boren, D.; Fischer, H.; Ji, Z.; Chang, C. H.; Liu, R.; Tolaymat, T.; Telesca, D.; Zink, J. I.; Cohen, Y.; Holden, P. A.; Godwin, H. A. Toxicity Mechanisms in Escherichia Coli Vary for Silver Nanoparticles and Differ from Ionic Silver. *ACS Nano* **2014**, *8* (1), 374–386.

(30) Yu, S.; Yin, Y.; Liu, J. Silver Nanoparticles in the Environment. *Env. Sci Process. Impacts* **2013**, *15* (1), 78–92.

(31) Levard, C.; Hotze, E. M.; Colman, B. P.; Dale, A. L.; Truong, L.; Yang, X. Y.; Bone, A. J.; Brown, G. E.; Tanguay, R. L.; Di Giulio, R. T.; Bernhardt, E. S.; Meyer, J. N.; Wiesner, M. R.; Lowry, G. V. Sulfidation of Silver Nanoparticles: Natural Antidote to Their Toxicity. *Environ. Sci. Technol.* **2013**, *47* (23), 13440–13448.

(32) Stabryla, L. M.; Johnston, K. A.; Millstone, J. E.; Gilbertson, L. M. Emerging Investigator Series: It's Not All about the Ion: Support for Particle-Specific Contributions to Silver Nanoparticle Antimicrobial Activity. *Environ. Sci. Nano* **2018**, *5* (9), 2047–2068.

CHAPTER 5: LOOKING TOWARD THE FUTURE OF CLocK MICROSCOPY FOR MONITORING NANOPARTICLE SURFACE CHEMSITRY

5.1 Introduction

The development of calcite-assisted localization and kinetics (CLocK) microscopy was driven by the need for an optical technique capable of increasing the information encoded in single particle images. Information on nanoparticle size can be deduced from the scattering intensity of a dark-field image while changes in spatial position by localizing the intensity profile of the diffraction-limited spot can provide insight into how the nanoparticle shape may change during an electrochemical process.[1–8] However, obtaining orientation and structural information are typically not as straightforward. While the development of multi-parameter super-resolution techniques is an active area of research, many of the methods require this tradeoff, such as sacrificing temporal resolution of the imaging system or the ability to localize in a linear way.[9–13] Chapter 3 of this dissertation demonstrated CLocK microscopy as a multiparameter super-resolution technique that does not require a tradeoff and showed how it can easily be integrated into a dark-field setup (we note that other work has demonstrated its utility in fluorescence and surface-enhanced Raman scattering as well).[5,7,14] In this chapter, we will look toward the future of CLocK and the information it could provide to better understand the dynamics of our silver nanoparticle with sacrificial silver-sulfide shells discussed in Chapter 4.

5.2 CLocK Microscopy for Monitoring Multiple Silver-Sulfide Species on Surface of Silver Nanoparticles

In Chapter 4 of this dissertation, we discussed a strategy for resetting the surface chemistry of single silver nanoparticles (Ag NPs) to a more homogeneous state by chemically growing an exterior silver-sulfide (Ag_2S) shell to compete with unwanted surface contaminants. By cathodically stripping this shell, we observed a more reproducible and reactive silver surface is attainable as evident by improved oxidation behavior of the freshly cleaned Ag NPs. While the focus of this study was to highlight the ability of a sacrificial growth model to improve reproducibility across a population of nanoparticles, we additionally discovered that sulfide-dependent and particle-dependent sulfide species would grow on the surface of single nanoparticles during sulfidation.

We expect the CLocK point spread function (PSF) will now provide a strategy for understanding both how the formation of sulfide-containing shells impacts particle anisotropy, as well as how changes in the localized position of the nanoparticle reflect shell non-uniformity. For example, the TEM images in Figure 5.1 (previously shown in Chapter 4) highlight the spherical shape of unreacted Ag NPs prior to surface modification, suggesting that their CLocK image will have uniform $e_{\perp}$ ring around the diffraction-limited $o_{\parallel}$ spot, with modulation depths close to zero. On the other hand, for high [HS^-] conditions, we hypothesized that the sulfide integrates and forms pockets of Ag_2S in the core of the Ag NP, based on the TEM images for these particles (Figure 5.2) where heterogeneous shapes (non-spherical/globular) were observed. Thus, CLocK images of Ag NPs reacted with high [HS^-] would show a higher degree of anisotropy (observed as angle-dependent intensity in the $e_{\perp}$ ring pattern). By quantifying the degree of anisotropy through the

modulation depth (*M* value as discussed in Chapter 3) we can gain insight into how the concentration of sulfide used during sulfidation influences heterogeneous NP structures across the population and draw relationships as to how that impacts the stripping and subsequent oxidation behavior on a single particle level.

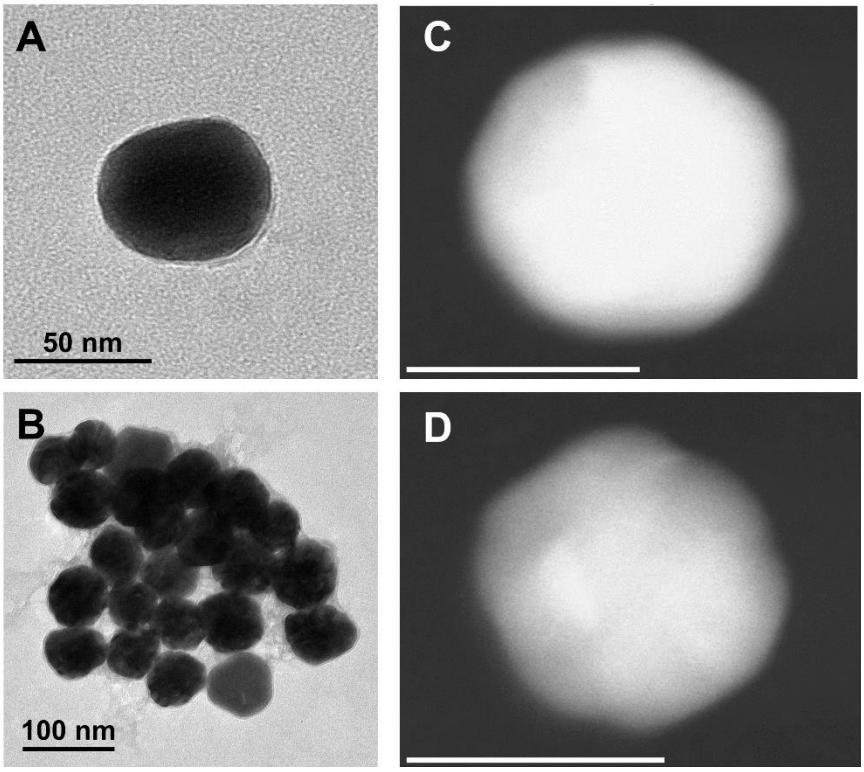

Figure 5.1. A series of TEM images highlighting spherical shape of unreacted Ag NPs. (A) TEM image of a single unreacted Ag NP. (B) TEM image of aggregated sample of unreacted Ag NPs. (C-D) HR-TEM images of single unreacted Ag NPs. Scale bars (C-D) = 50 nm.

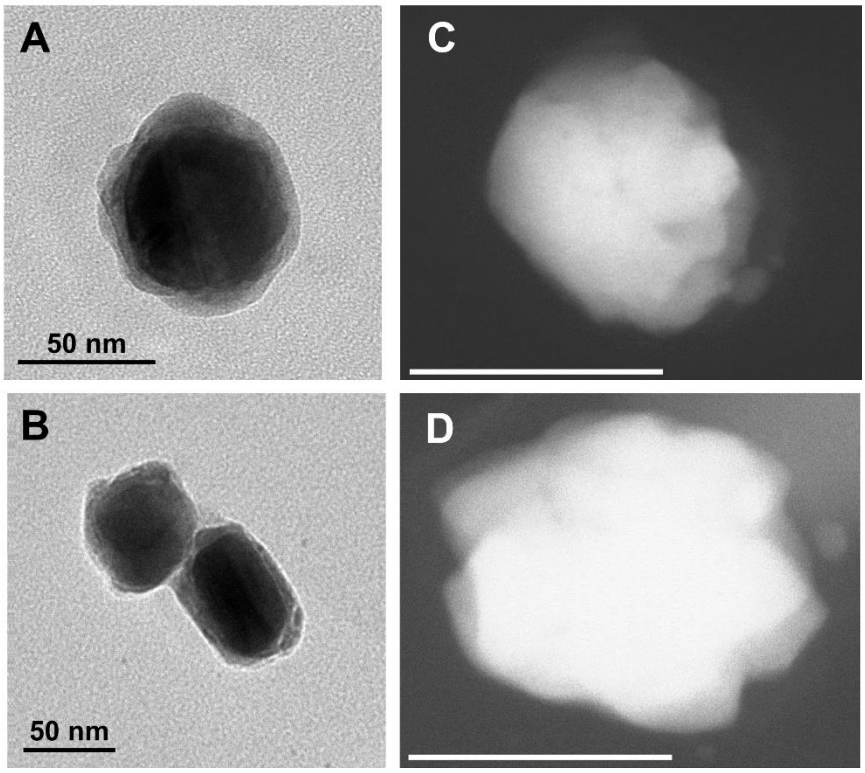

Figure 5.2. A series of TEM images highlighting how the shape of reacted Ag NPs change upon sulfidation. (A) TEM image of a single Ag NP reacted with high [HS^-] (50 µM HS^-). (B) TEM image of Ag NP dimer reacted with high [HS^-] (50 µM HS^-). (C-D) HR-TEM images of single Ag NPs reacted with high [HS^-] (50 µM HS^-). Scale bars (C-D) = 50 nm.

For low and intermediate [HS^-], where types A and B AgSH and monolayer Ag_2S were hypothesized to be in mixed quantities on the surface of Ag NPs, CLocK images can report on the relative presence of each species by tracking the center of mass as different potentials are applied as well as monitoring the change in anisotropy. Based on the dark-field scattering and electrochemical data alone, it is difficult to speculate if type A and type B AgSH are symmetrically or asymmetrically present on the surface of the NPs as well as if monolayer Ag_2S coverage forms uniformly or preferentially from one side. To examine the surface coverage on Ag NPs after sulfidation, we can localize the center position ($o_{||}$ ray of CLocK image) of the NPs during an applied stripping potential of -1.1 V where it is

expected only type B will be removed. If the coverage of type A and B AgSH is symmetrically dispersed across the surface of an Ag NP, then there should be no change in center of mass during stripping at -1.1 V. If type B formed in a spatially distinct location on the NP surface, it is expected that there will be a directional change in the center of mass of the NP during stripping where type B is removed and type A remains.

Additionally, as the CLocK PSF produces a polarization resolved ring, we will be able to determine if the NP structure changes by monitoring the modulation depth (*M* value) during stripping. There will be no change in the *M* value if the shell is not successfully removed during stripping (as would be the case for a Ag NP predominantly covered in type A AgSH), or if the shell is successfully removed in a symmetric manner. If there is a preferential shell stripping leading to change in center of mass, we would expect that the *M* value will increase relative to the extent of anisotropic transformation of the NP. While it's possible there may be subtle differences in the *M* values for NPs reacted at low and intermediate [HS^-] due to scarce sulfide coverage, high [HS^-] form multiple-layers-thick sulfide shells as shown by the TEM images (Figure 5.2) for Ag NPs reacted with 50 µM HS^-, which should lead to structural changes that are easier to identify. In Figure 5.2A, we see an Ag NP that formed a thick, but uniform Ag_2S shell while in Figure 5.2C we see a Ag NP that formed an Ag_2S shell preferentially on the right side of the particle. For NPs such as these, CLocK microcopy will provide insight into how a NP behaves when completely passivated by an Ag_2S shell in comparison to partial coverage which is essential for understanding ideal conditions for a sacrificial shell cleaning procedure.

5.3 CLocK Microscopy for Monitoring Dynamic Sulfidation Reactions on Single Silver Nanoparticles

The growth mechanism of Ag_2S on metallic Ag has been investigated by bulk electrochemical techniques.[15–17] The electrochemical measurements suggested that adsorbed AgSH forms on the Ag surface with a monolayer Ag_2S intermediate species prior to bulk formation of Ag_2S. Our studies in Chapter 4 of this dissertation relied on a chemical growth process for the Ag_2S shell where we monitored changes to the Ag NPs before and after the sulfidation reaction, but not during. As our findings suggested that mixed character sulfide species form on the surface of Ag NPs, a study that focuses on monitoring single particle sulfidation in real time will lead to a greater understanding of the process and ultimately better control of the surface coverage.

We have conducted preliminary studies on the single particle sulfidation process by tracking the dark-field scattering of Ag NPs while reacting with a 50 μM HS^- solution. Figure 5.3 shows three different trials where the scattering intensity for multiple individual Ag NPs was monitored as they reacted over a 25-minute period. The average initial scattering intensity of the Ag NPs (t = 0 min, prior to sulfidation) was used to create a baseline to which the scattering intensity at each subsequent time point was normalized (dashed line in Figure 5.3 serves as guide for reader). For each trial, there is a time-dependent shell growth as evident by the decrease in scattering intensity from the initial value corresponding to the dampening of silver surface by the sulfide. We do note that the kinetics for this time-dependent growth are very different for each trial, suggesting other factors besides the Ag NPs and sulfide solution are impacting the growth, such as nanoparticle density. Despite the differences in reaction kinetics, trial 1 (black data) and

trial 2 (red data) both show an initial increase in scattering intensity prior to a decrease. It is possible that trial 3 (blue data) may also have an increase that happens faster than our acquisition rate. Based on these data, CLocK microscopy could be employed to better understand the process and its variability between trials.

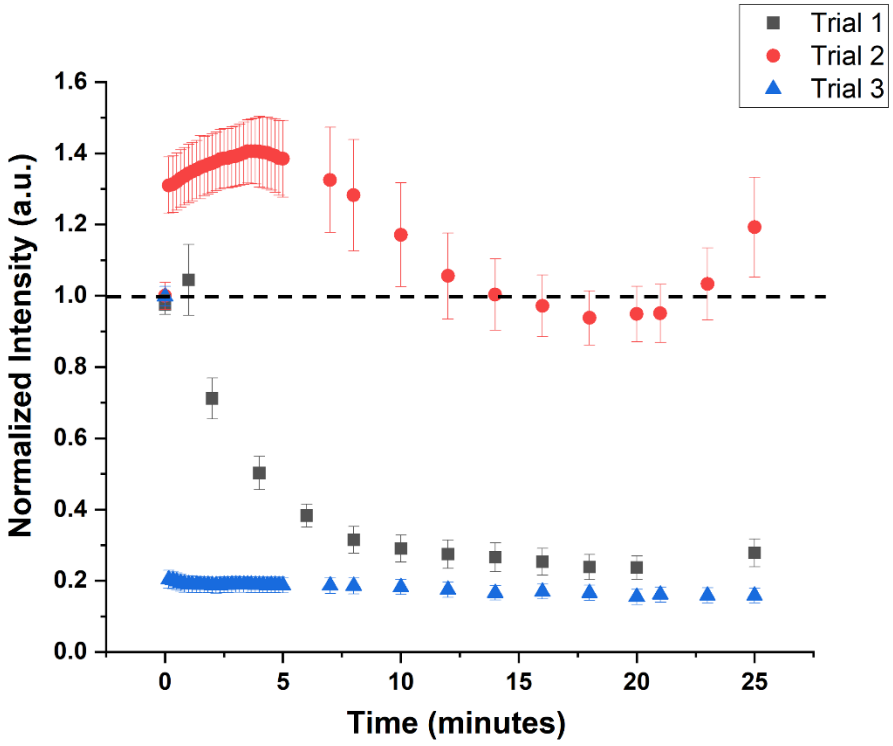

Figure 5.3. Normalized average scattering intensities of single Ag NPs undergoing real-time sulfidation reaction with 50 µM HS^-. In each trial more than 120 NPs were monitored. Dashed line added at the initial scattering intensity to serve as guide for the reader. The rise in scattering intensity from t = 0 → t = 1 min for trial 1 (black data) made us interested in the dynamics during the initial stages of sulfidation, as such, the scattering intensities for trial 2 (red data) and trial 3 (blue data) was recorded continuously from t = 0 → t = 5 mins. Sulfide solution and Ag NP concentration were prepared to match conditions of chemical growth as discussed in Chapter 4 of this dissertation.

CLocK images will provide insight into different stages of sulfide formation on single Ag NPs by analyzing the intensity of the $e_\perp$ ring and any changes in the *M* value over time. Moreover, the kinetic capabilities of CLocK will allow us to correlate any changes

in anisotropy during each stage of sulfide growth to time scales that are faster than the acquisition of the optical image. The added kinetic information encoded in the $e_{\perp}$ ring is useful for data such as trial 3 in Figure 5.3 where the sulfidation process occurs rapidly and is complete by the first optical image recorded. CLocK microscopy can also provide insight into the surface modification process that leads to the initial increase in scattering intensity that was observed in trails 1 and 2. It is possible that this initial scattering increase is the sulfide removing contaminants or the citrate capping agent from the Ag NP surface prior to Ag_2S formation.

At the high [HS^-] we used in these single particle growth experiments, we proposed that sulfide may integrate into the Ag NP core causing displacement of metal silver with Ag_2S. While in the previous section of this chapter we discussed how dark-field CLocK images could be used to explore this mechanism post-sulfidation, it could be further explored in real time by taking advantage of the spectral capabilities afforded by CLocK. Song and coworkers looked at the single particle sulfidation kinetics of silver nanocubes reacting with cysteine.[17] They observed particle-dependent color changes of single nanocubes by monitoring the dark-field scattering through a true color digital camera during sulfidation. The authors attributed the particle-dependent color changes with different stages of sulfide growth. Similarly, we can isolate single particle scattering spectra by extracting changes in color of a dark-field color CLocK image (Figure 5.4). It is expected that at high [HS^-] different stages of sulfide growth will lead to particle-dependent damping and red shift in the spectra as Ag_2S forms and effectively passivates the Ag NP surface. By correlating structure, temporal, and spectral information from

CLocK images, we can gain valuable mechanistic information into the sulfidation of single Ag NPs.

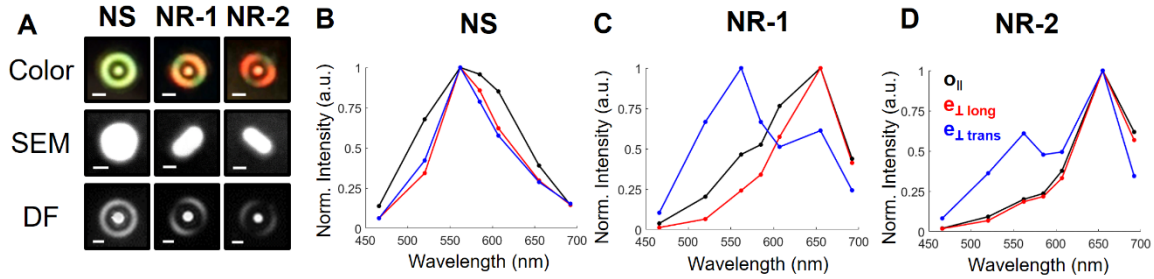

Figure 5.4. Example of how spectral features can be found in CLocK images. (A) Top-down: dark-field color CLocK images, SEM images, dark-field CLocK image for a gold nanosphere (Au NS), a large-width gold nanorod (Au NR-1, 126 x 61nm) and small-width gold nanorod (Au NR-2, 113 x 51nm). (B-D) Normalized scattering intensity spectra of the $o_{\parallel}$ (black), $e_{\perp\ long}$ (red), and $e_{\perp\ trans}$ (blue) of the CLocK image as a function of wavelength (series of bandpass filters used).

5.4 Conclusions

CLocK microscopy allows for intensity, localization, orientation and structural information to be extracted from a single optical image thus opening the pathway for many applications. Here we looked to the future of CLocK microscopy being used to monitor multiple silver-sulfide species growing on the surface of silver nanoparticles by easily integrating into existing optical-electrochemical experimental setups. We additionally discuss how CLocK microscopy can be used to observe the dynamics of this multiple sulfide growth mechanism by taking advantage of enhanced kinetic and spectral information that is encoded in a CLocK image. While CLocK is easily integrated into the single nanoparticle electrochemical experiments discussed in this dissertation, other areas of research such as biological and materials science could also benefit from this multiparameter super-localization approach where the need to infer mechanisms to limited optical information is a mutual concern.

5.5 Acknowledgements

The preliminary data discussed in this chapter was supported by the U.S. National Science Foundation under grant number DMR-2003613. Additionally, I would like to acknowledge Sanjay Sridhar for his contributions to the data collected and experimental design of the single particle sulfidation experiments.

5.6 References

(1) Sundaresan, V.; Monaghan, J. W.; Willets, K. A. Visualizing the Effect of Partial Oxide Formation on Single Silver Nanoparticle Electrodissolution. *J. Phys. Chem. C* **2018**, *122* (5), 3138–3145.

(2) Sundaresan, V.; Monaghan, J. W.; Willets, K. A. Monitoring Simultaneous Electrochemical Reactions with Single Particle Imaging. *ChemElectroChem* **2018**, *5* (20), 3052–3058.

(3) Molina, N. Y.; Pungsrisai, T.; O'Dell, Z. J.; Paranzino, B.; Willets, K. A. The Hidden Role of the Supporting Electrode for Creating Heterogeneity in Single Entity Electrochemistry. *ChemElectroChem* **2022**, *9* (9).

(4) Tschulik, K.; Batchelor-McAuley, C.; Toh, H.-S.; Stuart, E. J. E.; Compton, R. G. Electrochemical Studies of Silver Nanoparticles: A Guide for Experimentalists and a Perspective. *Phys. Chem. Chem. Phys.* **2013**, *16* (2), 616–623.

(5) Stranahan, S. M.; Willets, K. A. Super-Resolution Optical Imaging of Single-Molecule SERS Hot Spots. *Nano Lett.* **2010**, *10* (9), 3777–3784.

(6) Willets, K. A.; Wilson, A. J.; Sundaresan, V.; Joshi, P. B. Super-Resolution Imaging and Plasmonics. *Chem Rev* **2017**, *117* (11), 7538–7582. https://doi.org/10.1021/acs.chemrev.6b00547.

(7) Stranahan, S. M.; Titus, E. J.; Willets, K. A. SERS Orientational Imaging of Silver Nanoparticle Dimers. *J. Phys. Chem. Lett.* **2011**, *2* (21), 2711–2715.

(8) Titus, E. J.; Weber, M. L.; Stranahan, S. M.; Willets, K. A. Super-Resolution SERS Imaging beyond the Single-Molecule Limit: An Isotope-Edited Approach. *Nano Lett.* **2012**, *12* (10), 5103–5110.

(9) Möckl, L.; Moerner, W. E. Super-Resolution Microscopy with Single Molecules in Biology and Beyond–Essentials, Current Trends, and Future Challenges. *J. Am. Chem. Soc.* **2020**, *142* (42), 17828–17844.

(10) Wang, W.; Shen, H.; Shuang, B.; Hoener, B. S.; Tauzin, L. J.; Moringo, N. A.; Kelly, K. F.; Landes, C. F. Super Temporal-Resolved Microscopy (STReM). *J. Phys. Chem. Lett.* **2016**, *7* (22), 4524–4529.

(11) Wang, W.; Shen, H.; Moringo, N. A.; Carrejo, N. C.; Ye, F.; Robinson, J. T.; Landes, C. F. Super-Temporal-Resolved Microscopy Reveals Multistep Desorption Kinetics of α-Lactalbumin from Nylon. *Langmuir* **2018**, *34* (23), 6697–6702.

(12) Kress, A.; Wang, X.; Ranchon, H.; Savatier, J.; Rigneault, H.; Ferrand, P.; Brasselet, S. Mapping the Local Organization of Cell Membranes Using Excitation-Polarization-Resolved Confocal Fluorescence Microscopy. *Biophysical Journal* **2013**, *105* (1), 127–136.

(13) Chen, K.; Gu, Y.; Sun, W.; Bin Dong; Wang, G.; Fan, X.; Xia, T.; Fang, N. Characteristic Rotational Behaviors of Rod-Shaped Cargo Revealed by Automated Five-Dimensional Single Particle Tracking. *Nat Commun* **2017**, *8* (1), 887.

(14) Monaghan, J. W.; O'Dell, Z. J.; Sridhar, S.; Paranzino, B.; Sundaresan, V.; Willets, K. A. Calcite-Assisted Localization and Kinetics (CLocK) Microscopy. *J. Phys. Chem. Lett.* **2022**, *13* (45), 10527–10533.

(15) Hatchett, D. W.; White, H. S. Electrochemistry of Sulfur Adlayers on the Low-Index Faces of Silver. *J. Phys. Chem.* **1996**, *100* (23), 9854–9859.

(16) Hatchett, D. W.; Gao, X.; Catron, S. W.; White, H. S. Electrochemistry of Sulfur Adlayers on Ag(111). Evidence for a Concentration- and Potential-Dependent Surface-Phase Transition. *J. Phys. Chem.* **1996**, *100* (1), 331–338.

(17) Conyers, J. L.; White, H. S. Electrochemical Growth of Ag2S on Ag(111) Electrodes. Coulometric and X-Ray Photoelectron Spectroscopic Analysis of the Stepwise Formation of the First and Second Monolayers of Ag2S. *J. Phys. Chem. B* **1999**, *103* (11), 1960–1965.